Lower-Middle Cambrian Microbialites from South Australia: Construction, Biofacies and Biogeochemistry.

Bronwyn Louise Teece

Masters of Research (MRes)

Supervisor: Prof. Simon C. George

Co-Supervisor: Assoc. Prof. Glenn A. Brock

Department of Earth and Planetary Sciences,

Macquarie University, Sydney, Australia

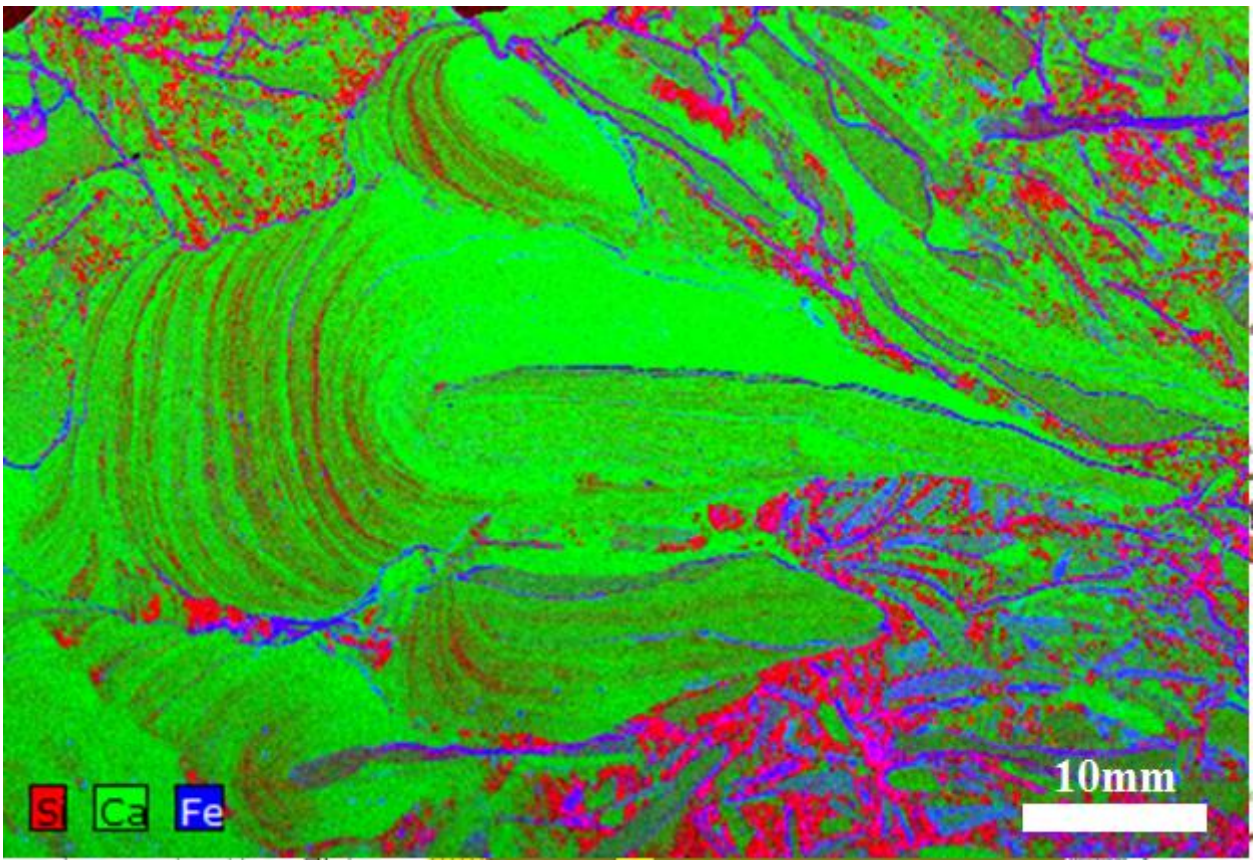

False colour X-ray Flourescence element map of sample WP1.

Submitted on 09th October, 2017.

Contents

Abstract

Microbialites are organo-sedimentary deposits, sometimes composed of accumulations of cyanobacteria and other bacteria, which form at the sediment-water interface. Microbialites represent one of the earliest records of life on Earth, with stromatolites - laminated accretionary microbialites - dating back at least 3.7 Ga. Stromatolites became extremely diverse and abundant throughout the Archean era (4-2.5 Ga), causing increased atmospheric oxygen levels on Earth as part of the Great Oxidation Event. The early Cambrian bilaterian radiation coincided with a sharp decline in stromatolite abundance.

In this study, microbialites were sampled from lower and middle Cambrian carbonate facies in the Arrowie Basin, South Australia. The appearance, construction, and biogeochemistry of stromatolites from different depositional environments, is described to investigate morphological variation and ecological associations, which may have been altered after the evolution of epifaunal grazing bilaterians. Few research projects have investigated stromatolites in the Arrowie Basin. This project investigates morphological variations in microbialites through petrographic observations, attempting to resolve previously unanswered biogeochemical questions using multi-disciplinary techniques: field relationships, hand and thin section observations, gas chromatography-mass spectrometry, Raman spectroscopy, fourier transform infrared spectroscopy, and X-ray fluorescence. The samples are highly thermally mature. Microbialites are not found in association with any fossils preserved in life position. Depositional environments ranging from shallow supratidal to low-energy subtidal are consistent with previous regional interpretations.

Declaration

All research was conducted with funding from Macquarie University HDR Funds, the Betty Mayne Fund from the Linnean Society of NSW, and research funds from Prof. Simon C. George of Macquarie University.

No Ethics Committee approval was necessary for this research.

I hereby certify that this thesis is my own work and has not been submitted for a Higher Degree at any other University or Institution.

Bronwyn Louise Teece

Signed by: 6821869b-2c29-47f5-955d-6450a6b87f34

Acknowledgements

I would like to show my respect and acknowledge the Adnyamanthanha people, the Traditional Custodians of the Land, of Elders past and present, on which my fieldwork took place. Additionally, I show my respect and acknowledge the Darug people, the Traditional Custodians of the Land, of Elders past and present, on which my research and university career have taken place. Sincere thanks property owners Ian and Di Fargher (Angorichina), and Graham and Laura Ragless (Beltana) for permission to access field locations on their properties.

To my supervisor Prof. Simon C. George, four and a half years ago you taught me the word stromatolite, and introduced me to my passion in life. I used to want to be an academic who studied science fiction texts, and now, because of you, I get to make science fiction a reality. Your dedication, patience, and aptitude for teaching inspire me every day. And I will be forever grateful you let me be one of your students.

To my co-supervisor Assoc. Prof. Glenn A. Brock, your knowledge of the Arrowie basin, is awe-inspiring. Thank you for expecting perfection, and making me strive to be a better scientist, and thank you for being a walking map in the field when our maps were delayed. I've never been so impressed as I was when you lead us through the Flinders, day after day with no map.

Sarah Houlahan, I'm lucky to have sat next to you that first day in biology. Few people, get to have a university buddy whose interests, both academically and personally, so closely match their own.

To Dr. Sarah Jacquet thank you for your help with photoshop, microscopy and for letting me bounce ideas off you. Oluwatoosin Agbaje, thank you for not only teaching me how to use FTIR and Raman spectroscopy, but for the light and brightness that you bring everywhere you go, you are a joy to work with. Josh Shea, thank you for showing me how to describe thin sections, and being interested in my project, my work is better for discussing it with you. Ben Alsop, your help with structural geology was greatly appreciated. Dr. Tim Murphy thank you for teaching me how to use XRF and patiently sitting through my endless questions and emails. Matt Kerr, thank you for your coding lessons, and for being my beer and debrief buddy.

To my great-grandmother Joy, my nana Jackie, and my mother Robyn, thank you for showing me that the mark of a strong, and successful, woman is not the ability to succeed the first time she does something, but rather, her perseverance and determination to succeed.

1. Introduction

The Cambrian fossil record contains evidence for the beginning of bioturbation, direct evidence of zooplankton, rapid expansion of biomineralisation, first animal reef systems, complex exoskeletons, and temporally differentiated distributions of novel taxa (Marshall, 2006; Bush et al., 2011). Ocean chemistry also changed significantly after animals evolved: dissolved carbon content was reduced because of zooplankton ventilation, carbonate saturation in the ocean decreased because metazoans developed a metabolic pathway to incorporate carbon into a biomineralised exoskeleton, and sediments in the ocean became aerated because of bioturbation and bio-irrigation (Bush et al., 2011). Due to all these rapid developments, a complex system of ecological niches and feedbacks quickly developed in the Cambrian, including a reduction in the distribution and abundance of microbial build-ups (microbialites) (Bush et al., 2011; Chen et al., 2011). During the Proterozoic and early Palaeozoic, microbialites were the world's first large-scale biotic constructions; although stromatolites have been reported from the Archean (Marshall et al., 2007; Tosti et al., 2011). Microbialites have also significantly affected the way the Earth developed, an effect termed the Gaia Hypothesis (Chopra and Lineweaver, 2016). Microbialites record atmospheric conditions, seawater chemistry, mat and organic evolution, and thus can act as "environmental dipsticks" (Grotzinger and Knoll, 1999; Mukhopadhyay and Thorie, 2016).

Furthermore, through recording the sediment-water interface, microbialites can show the evolution of the intricate diversities of ecosystems at these locations (Mukhopadhyay and Thorie, 2016). Historically, research into early life was hampered by the problematic nature of relying simply on physical fossils (Knoll et al., 2016). The physical fossil record is insufficient for representative sampling, ecology, and time (Knoll et al., 2016). Whilst areas of exceptional preservation aid in detangling these relationships, these would be greatly supported by a geochemical record. Molecular fossils are useful for looking at a variety of questions, including the identity and relationships of extinct organisms (Brocks and Pearson, 2005). Thus, by investigating the physical, biogeochemical and geochemical record of these microbialites more information about the processes that govern these structures during ecological change and transitions can be gleaned.

1.1 The Cambrian

The Ediacaran-Cambrian boundary is a primary division in the history of life. The fossil record shows that all major animal phyla radiated within 30 million years after the boundary (Fig. 1) (Bush et al., 2011; Erwin et al., 2011) . The Cambrian explosion is arguably the most important step in evolutionary history, representing a rapid change from primitive life to abundant protists and multicellular organisms; a complicated series of radiations and extinctions (Pagès et al., 2016). It has been proposed that either increased levels of oxygen, or nutrient availability, may have been an

important factor constraining diversification (Bush et al., 2011; Brocks et al., 2017). During the early Cambrian, reefs transitioned from stromatolitic to metazoan but, collapsed worldwide by the middle Cambrian. There are no clear answers as to why these changes occurred in the Cambrian (Pagès et al., 2016). Cambrian reef systems are regarded as having two predominant stages. The first stage, where reefs were primarily composed of archaeocyaths cemented by calicimicrobes, stretched throughout the earluy Cambrian (Zhuravlev, 1996). The middle to late Cambrian is marked by a second microbial stage, after archaeocyath decline (Mata and Bottjer, 2012). Recent research suggests that metazoans had a larger role in Cambrian reef building than previously thought, which may be investigated through biomarkers (Coulson and Brand, 2016).

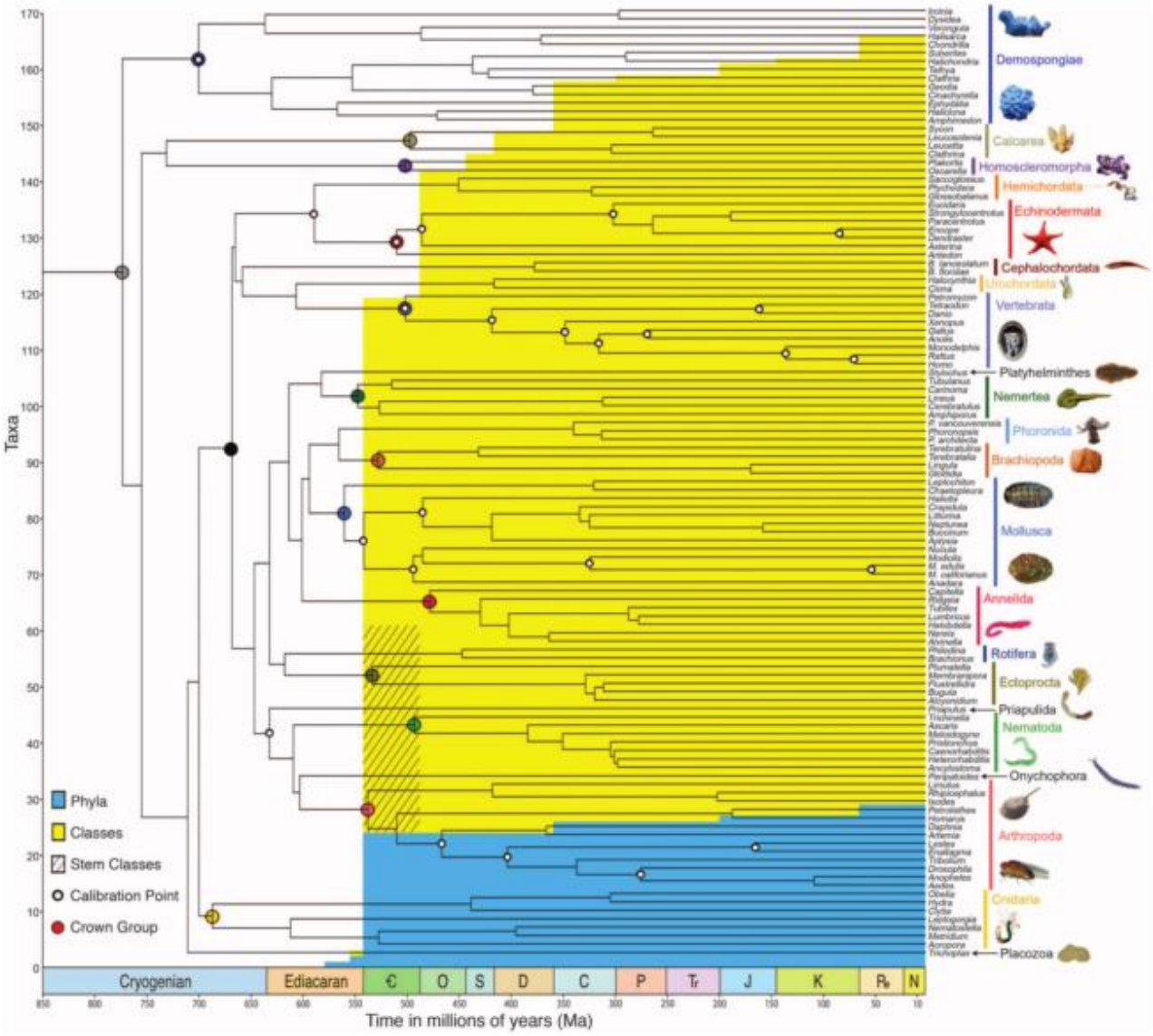

Figure 1. The origin and diversification of animals as inferred from the geological and genetic fossil records (Erwin et al., 2011).

1.1.1 Microbial Radiations in the early Cambrian

There is a notable microbial response in the late early Cambrian, when two successive extinction pulses mark the near elimination of almost all archaeocyath taxa: the Sinsk Event and the Hawke

Bay Event. The Sinsk event delineates a global occurrence of non-bioturbated laminated black shales with dysaerobic fauna (Mata and Bottjer, 2012). This is typically attributed to widespread development of anoxic conditions in shallow marine environments, which occurred concurrently with a transgression. Anoxia resulted from phytoplankton blooms at the start of the transgression (Zhuravlev and Wood, 1996; Mata and Bottjer, 2012) . The significance of the Hawke Bay event lies in a global regression which instigated a significant reduction in shelf area, followed by intervals of marine anoxia throughout the rest of the Cambrian (Zhuravlev and Wood, 1996; Mata and Bottjer, 2012).

1.2 Microbialites

Microbialites are different morphological structures that can be abiogenically mediated, or biogenically mediated by microbes that trapped and bound sediments (Riding, 2000; Chen et al., 2011). The three types of fossilised microbialites considered here are stromatolites, oncolites, and thrombolites.

1.2.1 Stromatolites

Stromatolites are microbial growths which accrete simultaneously with carbonate precipitation, and are the most abundant and ancient form of fossils throughout the geological record (Mukhopadhyay and Thorie, 2016; Murphy et al., 2016). They were formed in a wide variety of environments, from diverse microbial communities, and are now found in restricted environments (Murphy et al., 2016). They are the only macroscopic fossils that formed for nearly 3 billion years of Earth's history, and continue to the present; although they almost disappeared by the late Neoproterozoic, and thereafter were restricted to primarily peritidal facies in marginal marine settings (Garcia-Pichel et al., 2004; Mata and Bottjer, 2012; Murphy et al., 2016). Modern stromatolites are typically found in environments which are not preferable to metazoans, such as hypersaline, brackish, low-light, and anoxic environments (Mata and Bottjer, 2012). The most oft-cited hypothesis attributes the reduction in abundance of stromatolites to the evolution of new ecological processes, such as grazing (Garcia-Pichel et al., 2004). Other causes that have been proposed include competitive exclusion by microalgae, changes in seawater chemistry, and changes in sedimentation rates (Garcia-Pichel et al., 2004). However, in environments where grazing metazoans are absent modern stromatolites typically exhibit intense growth and accretion (Mukhopadhyay and Thorie, 2016). Riding (2006) proposed that the two primary controls on stromatolite abundance and distribution are metazoan diversity, and carbonate saturation. However, more recent research shows that whilst metazoan diversity generally rises with a decrease in microbial activity, carbonate saturation has no significant associations (Mata and Bottjer, 2012). Phanerozoic stromatolites typically exhibit a large resurgence in the aftermath of extinction events (Mata and Bottjer, 2012), such as the recovery of

stromatolites, in the early Triassic, after the Permian-Triassic event (Schubert and Bottjer, 1992), and the recovery of microbialites after the Late Ordovician extinction event (Sheehan and Harris, 2004).

Stromatolite morphology is highly varied, from simple domes or cones to complex column structures. The microstructures that they comprise are likewise architecturally-varied, sometimes with thin lenses and other macro formations existing over hundreds of kilometres (Grotzinger and Knoll, 1999). A non-genetic definition of a stromatolite is an "attached, laminated lithified sedimentary growth structure, accretionary away from a point of limited surface of initiation" (Grotzinger and Knoll, 1999). This definition is useful because it includes simple geometric and textural features of all stromatolites, whilst allowing for biogenic/abiogenic formation (Grotzinger and Knoll, 1999). Studies of the physical form, mineralogical composition and organic content of stromatolites can reveal information about the environments under which they formed (Douglas et al., 2015).

1.2.2 Thrombolites

Thrombolites are macroscopically clotted microbial carbonates that were particularly abundant in shallow marine environments throughout the early Palaeozoic, and are still found in modern environments (Riding, 2000; Harwood Theisen and Sumner, 2016). They are best known for becoming conspicuous around the Proterozoic/Cambrian boundary, and underwent a marked increase in abundance throughout the early Cambrian (Riding, 2000). Whilst stromatolites and other microbialites are easily described by their morphology, the complex nature of the internal structure of thrombolites makes such classification difficult (Harwood Theisen and Sumner, 2016). Some thrombolites have an internally clotted or patchy fabric reflecting highly varied growth structures, and can be examined as the interplay between microbial communities and environmental processes (Fig. 2) (Harwood Theisen and Sumner, 2016).

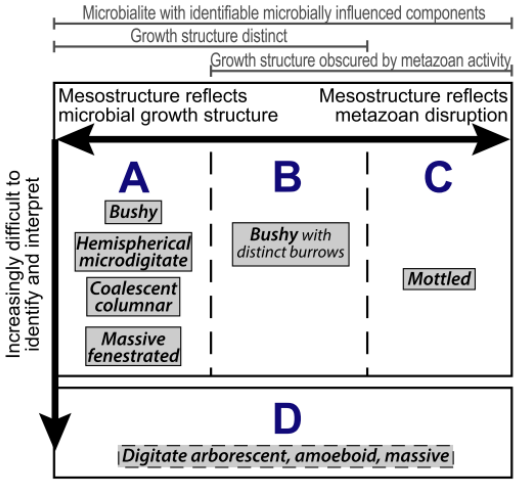

Figure 2. Schematic diagram showing thrombolite classes in the context of the degree that mesostructure reflects microbial growth structure versus metazoan disruption, as well as how easy the growth structure is to identify and interpret (Harwood Theisen and Sumner, 2016).

1.2.3 Oncolites

Oncolites are unattached, regularly or irregularly spheroidal, concentrically to semi-concentrically laminated bodies of microbial origin (Aitken, 1967). Oncolites are primarily made up of oncoids, (atypically large microbially-mediated carbonate-coated grains), and are particularly

prevalent throughout the Cambrian (Shi and Chen, 2006). Oncolites generally form in low-energy environments with intermittent moderate to high energy fluxes, but have highly variable abundance and distribution (Shi and Chen, 2006; Hicks and Rowland, 2009). Oncolite units can vary in texture between ooid-supported and oncoid-supported (Wilmeth et al., 2015).

1.3 Geochemistry

1.3.1 Biomarkers

Biomarkers are chemical or molecular fossils, usually hydrocarbons. which have been preserved in sedimentary rocks and which have structures that link them to the original lipids in living organisms. Biomarkers are typically identified by use of Gas Chromatography- Mass Spectrometry (GC-MS), which separates hydrocarbons based on retention times. Biomarkers can represent a myriad of remnants, including original organic material and/or diagenetic products (Peters et al., 2005). A robust biomarker is something that is difficult to produce via inorganic processes (Awramik et al., 2005). Molecular fossils provide complementary information to the physical fossil record, as some can be used as tools to indicate the presence of a particular group of organisms (Fig. 3) (Pawlowska et al., 2013). There are two classes of polycyclic lipids - sterols and hopanoids, which are used to diagnose eukaryotes and bacteria respectively (Briggs and Summons, 2014).

Microbes don't get preserved very well as body fossils, so using organic geochemical methods can help dismiss some preservation biases. The cell membranes of microbes are made up of lipids including fatty acids, hydrocarbons, alcohols, chlorophyll, carotenoid pigments, and diverse glycerol-esters and glycerol ethers, all of which are prone to being well preserved (Briggs and Summons, 2014). The chemistry of these lipids can be indicative of certain groups of organisms (Fig. S1, [Supplementary figures will be denoted by Fig. Sxx]). Microbial mats can form thick snot-like internal laminations which prevent transport of organic matter into the underlying sediment, increasing the preservation potential of these lipids (Pawlowska et al., 2013).

Using biomarkers in the early geological record can be problematic as it assumes that extant biota represent all the possible producers, and doesn't account for the presence of biomarkers in stem groups (Brocks and Pearson, 2005). To effectively utilise biomarkers it is necessary to demonstrate the relationship between biomolecules and some biological groups (Brocks and Pearson, 2005). There have been significant concerns over using organic compounds as diagnostic criteria in deep time, in part due to suspected contamination of some earlier work (Summons et al., 1988; Brocks et al., 1999). However, recent work has demonstrated techniques that can be used to ensure absence of contamination (French et al., 2015). Biomarkers can offer significant insight into early life and continue to provide very important constraints about biological evolution in the Precambrian (Brocks et al., 2017). Additionally, the biomarkers employed need to be specific. For

example, there are biopolymers in structural tissues like cuticles in arthropods, or lignified materials that support a higher plant origin, but they are not very taxonomically specific (Briggs and Summons, 2014). Few molecules are stable over the entirety of geological time, and their transformation pathways can be altered by the same processes that affect physical fossils such as thermal maturity (Briggs and Summons, 2014).

1.3.2 Fourier Transform Infrared Spectroscopy

Infrared (IR) spectroscopy has been applied to the study of microorganisms for nearly 60 years, as different bacteria display diverse infrared spectra (Preston et al., 2014). Fourier transform infrared spectroscopy (FTIR) is utilised in palaeontological studies to help characterise organic and inorganic compounds, crystalline or amorphous compounds, mineral content, and degradation (Reig, 2002; La Russa et al., 2009; Chen et al., 2015). Studies into the utilisation of FTIR for palaeontological studies show that there are bands that are specific to the chemical structures of complex kerogen molecules (Mastandrea et al., 2011). In FTIR analyses, the absorption of IR radiation occurs when a photon transfers to a molecule, and excites it to a higher energy state (Reig, 2002; Gunasekaran et al., 2006). Organic functional groups have differing bond strengths, and atom masses (Preston and Genge, 2010). FTIR analyses will not determine specific molecules, but instead determine classes of molecules with differing functional groups. For example, because the O-H and C=O functional groups each contain atoms of different masses, they absorb IR radiation at different positions in the spectrum (Preston and Genge, 2010; Mastandrea et al., 2011). For biological spectroscopy, the important vibrations occur in the mid-IR region (700-4000cm^{-1}) where most organic molecules display characteristic spectral features because they have different functional groups (Preston and Genge, 2010). Because FTIR can be used to identify a broad range of chemical functional groups in a variety of physical states, it is complementary to other methods such as Raman spectroscopy and GC-MS (Mastandrea et al., 2011; Olcott Marshall and Marshall, 2015). FTIR typically has better detection for minor components than Raman spectroscopy, and provides a comparable ability to classify and identify minerals (Mastandrea et al., 2011).

1.3.3 Raman Spectroscopy

Raman spectroscopy has been used in the field of palaeobiology since the 1970s and is increasingly utilised as a non-destructive method of analysing mineral and molecule data (Pflug and Jaeschke-Boyer, 1979; Marshall and Olcott Marshall, 2013). In Raman spectroscopy, a laser irradiates the sample which causes photon scattering, in turn causing changes in frequencies dependent on the masses of atoms involved in the vibration (Marshall and Olcott Marshall, 2013). There are two different ways the light gets scattered: elastically (Rayleigh scattered) or inelastically (Raman scattered) (Olcott Marshall et al., 2012). Raman scattered light causes the original frequency to

change in correspondence with a molecular vibration from within the sample (Olcott Marshall et al., 2012). Thus, the Raman shift is a product of the chemical bonds and symmetries of molecules and provides a common spectrum for the identification of both organic and inorganic molecules (Olcott Marshall and Cestari, 2015). Raman analysis can also be used to determine the thermal maturity of a sample, as it can determine when carbonaceous material has experienced thermal rearrangement (Allwood et al., 2006; Olcott Marshall et al., 2012; Olcott Marshall and Marshall, 2015). Raman spectroscopy has been used investigate the structure of carbonate minerals, and has been shown to differentiate between calcite and dolomite (Sun et al., 2014). Because Raman spectroscopy is more sensitive to the molecular framework than FTIR, it is more suited for the analysis of thermally mature carbonaceous materials and inorganic materials, such as biomineralised fossils (Olcott Marshall and Marshall, 2015).

1.3.4 Micro X-Ray Fluorescence (Micro-XRF)

XRF is a non-destructive analytical technique that allows both qualitative and quantitative analysis of the composition of a sample (Kalnicky and Singhvi, 2001). Micro-XRF scans a focused X-ray beam across the surface of a sample, determining elemental composition at mm-cm scales, with individual spot measurements of 100 μm diameter (Allwood et al., 2013). This technique has been used to map the growth processes of stromatolites (Quezergue, 2014), to determine the difference between stromatolitic and non-stromatolitic samples (Douglas et al., 2015), and to locate the least metamorphosed parts of a stromatolitic sample (Flannery et al., 2016).

1.4 Project Aims

1. To describe and reconstruct the depositional environments of the samples in this study.
2. To assess the thermal maturity of the samples taken from the Arrowie Basin.
3. To examine the organics present in the samples of this study, with particular attention to the interactions between microbialites and metazoans.

This study uses a multi-technique approach to attempt to provide novel geological and biogeochemical data about microbialite evolution and ecology during a period dominated by the radiation of complex animals.

2. Sample localities and the geological setting and age of the Arrowie Basin

The samples analysed in this study were collected from the Arrowie Basin (Fig. 3), a 55,000 km depocentre of lower Cambrian carbonate rocks exposed as a series of tight folds in the Flinders Ranges, South Australia (Gravestock and Cowley, 1995). The Flinders Ranges is part of the Adelaide Fold Belt, a deformed and folded sedimentary succession of late Proterozoic to middle

Cambrian sediments, representing a continental rift that evolved into a passive margin in the late Neoproterozoic (Groves et al., 2003; Zang et al., 2004; Turner et al., 2017). Deep water, intra-cratonic platform, reef carbonates and silicilastic sediments were deposited during the lower Cambrian (Fortunian—Cambrian Series 3) and sits unconformably on Neoproterozoic rocks (Jago et al., 2012).

The Arrowie Basin was subjected to regional tectonism, which influenced deposition of various shelf and slope facies (Jago et al., 2006) During the early Cambrian, Australia was located north of the equator as part of East Gondwana (connected to Antarctica and India), within the tropical carbonate development zone, (Brock et al., 2000; Jago et al., 2012). Sedimentation patterns show an intracratonic shallow marine platform succession to the west along the Gawler Craton, which passes eastwards as current day outcrops in the Arrowie Basin (Jago et al., 2013). Sedimentation modes reveal complex reef, platform, ramp, slope and trough sedimentary environments (Jago et al., 2013). Extensive karst development during the lower Cambrian resulted from widespread regression, which led to subaerial exposure of the Wilkawillina Limestone and development of the Flinders Unconformity (Groves et al., 2003). An iron-enrusted hardground surface was eventually colonised by microstromatolitic pioneers during later transgression (Groves et al., 2003). This regionally significant disconformity horizon represents a diachronous surface across the Arrowie Basin (Grooves et al., 2003). This study focuses on samples from the oldest (Woodendinna Dolostone, Wirrapowie/Wilkawilina limestones) and youngest (Wirrealpa limestone) carbonates from the lower Cambrian of South Australia (Fig. 4).

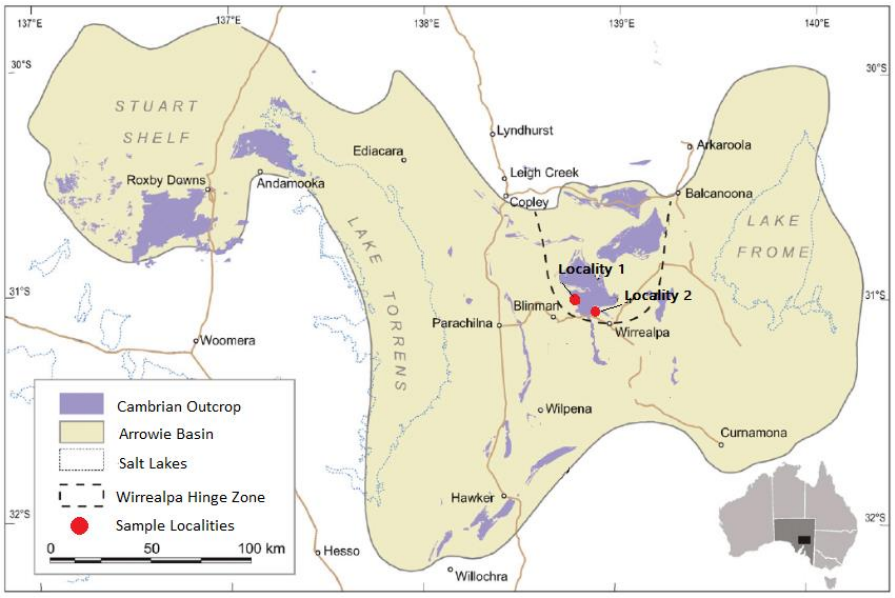

Figure 3. Map of the Arrowie Basin, showing Cambrian outcrops and stratigraphic section locations of samples collected herein - modified from Betts et al., (2016).

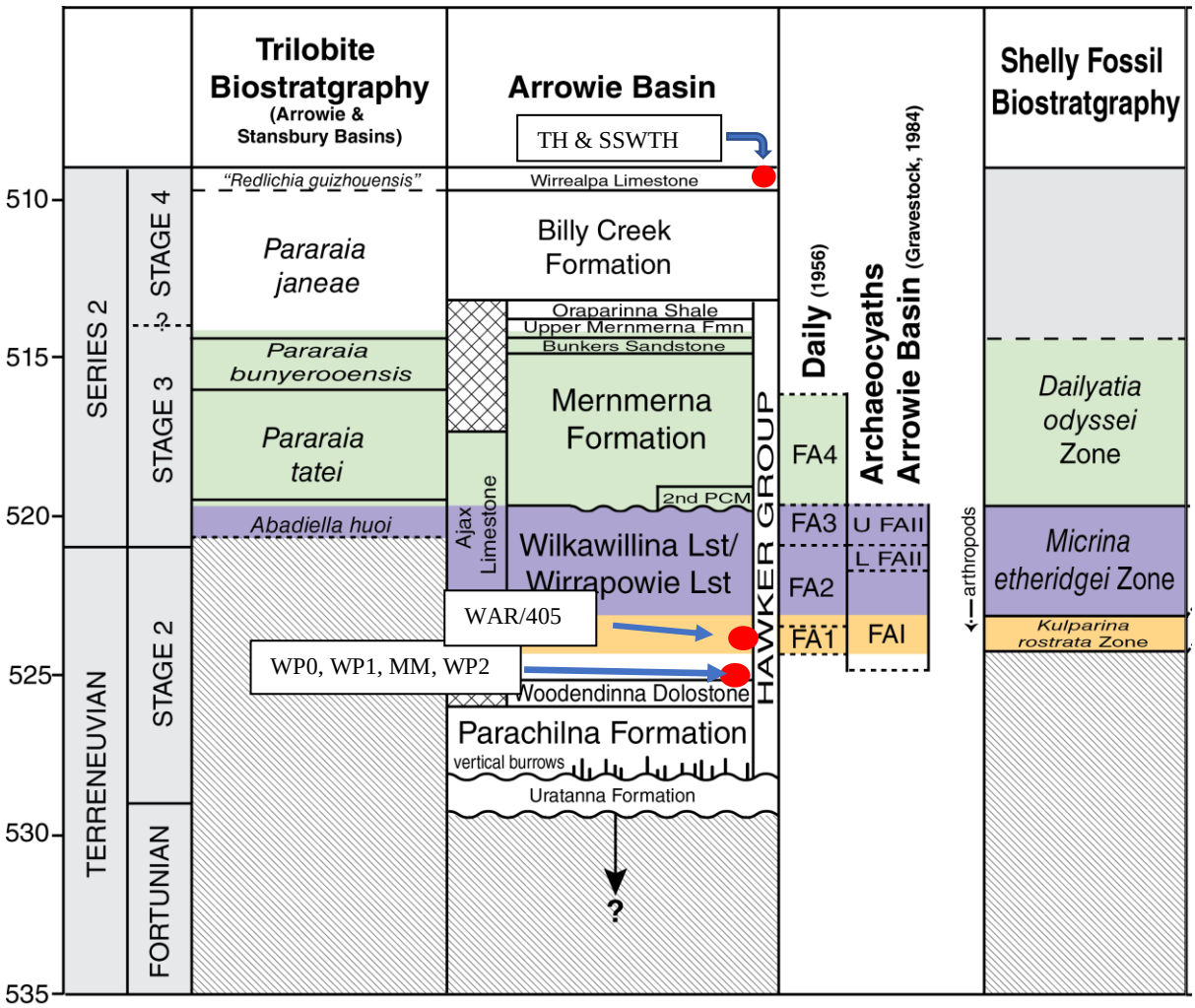

Figure 4. Biostratigraphy of the Arrowie Basin, modified from Betts et al., (2016), showing stratigraphic locations of samples collected for this investigation.

2.1 Locality 1: WAR Section, northern Bunkers Range

2.1.1 Sample Details and Locations

Samples WP0, WP1 WP2 (later split into two samples WP2 and MM), and WAR/405 were collected from spot localities on (or along strike from) the WAR stratigraphic section measured by Betts et al. (2016; Fig. 5). Samples WP0, WP1, MM and WP2 were taken from the Woodendinna Dolostone along a 25 m long transect with base at S31°01'30.2" E138°47'59.0", whereas sample WAR405 is located 301 m (true thickness) above the base of the WAR section at S31°01'21.1" E138°47'12.3 (Fig. 5).

Sample WAR/405 is derived from a relatively thin Wilkawillina Limestone that interfingers with the restricted lagoonal palaeoenvironments represented by the Wirrapowie Limestone (Haslett, 1975; Betts et al., 2016) or possibly a patch of shallower, more open marine platform carbonate facies of the Wirrapowie Limestone. This sample is largely a redeposited bioclastic limestone that is blocky and massive spalling in outcrop, with clotted microbial textures and macrofossil debris.

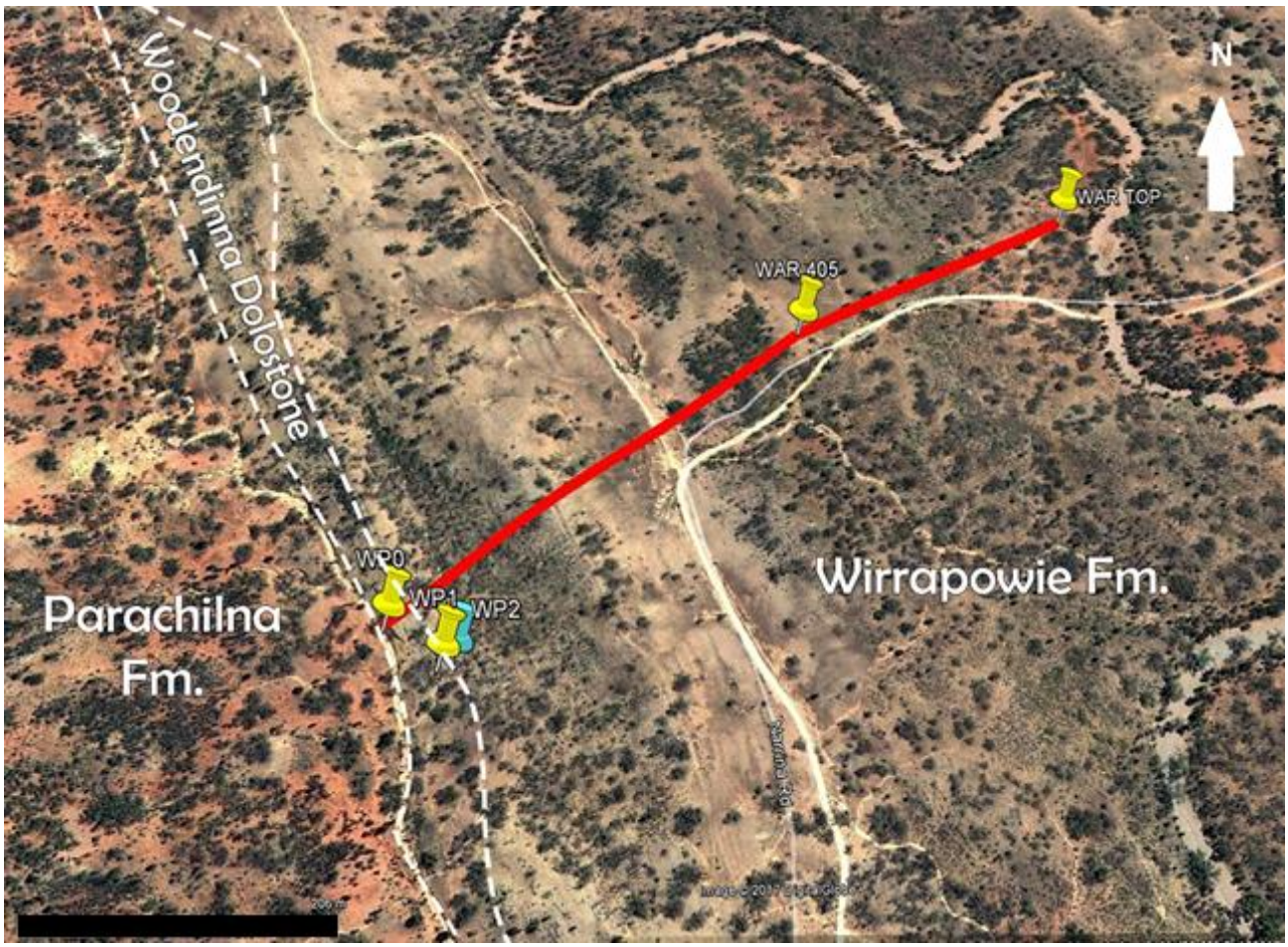

Figure 5. Google Earth image of samples (pin labels) collected from Locality 1 in the Bunkers Range. The red line indicates the position of the WAR stratigraphic section from Betts et al. (2016). Scale bar = 200m. Section is stratigraphically youngest to the right.

2.1.2 Geological setting

The Woodendinna Dolostone underlies the Wirrapowie Limestone at the base of the WAR section (Figs 4, 5 and 6) and is characterised by oolitic and pisolitic carbonates with high degrees of dolomitization (Haslett, 1975). The Wirrapowie Limestone is characterised by fine-grained micritic carbonates and microbialites and laminated stromatolites, which include massive low, domical forms, interbedded with laminated micritic limestone. Bioturbation, with minor cross-beds and peloidal carbonates with intraformational (flat pebble) conglomerates are also common. Haslett (1975) interpreted the Wirrapowie Limestone (at the type section) as primarily deposited in a low energy, possibly restricted lagoonal environment, with slow sedimentation rates suggested by the pervasive phosphatic firmground surfaces thoughout this unit. The lack of mud-cracks, halite casts and other evidence of subaerial exposure indicates that the environment was constantly submarine (Haslett, 1975). Occasional higher energy facies are represented by oolitic beds, and potentially the deposition of intraformational flat pebble conglomerates, although there is debate in the literature about how these form (Łuczyński and Kozłowski, 2014; Hong et al., 2015; Wright and Cherns,

2016). Coeval deposition of the Wirrapowie Limestone and the Wilkawillina Limestone is confirmed by the synchronous ranges of brachiopods, tommotiids and bradoriids in both facies (Betts et al., 2016). Shallowing-upwards sequences that consist of ooid sands, stromatolites, thrombolites and storm deposits of flat pebble conglomerates record progressively more open marine conditions up the section (James and Gravestock, 1990). There is syn-sedimentary faulting creating numerous fractures, on-shelf depressions and islands, but overall the facies mosaic comprises shallow-water carbonates (James and Gravestock, 1990).

2.1.3 Age

The samples from this locality, except WAR/405, occur in strata 250 m below the first occurrence of archaeocyaths and small shell fossils representing the *Kulparina rostrata* biozone, the oldest shelly fossil zone erected by Betts et al. (2016). This would indicate that the stromatolites from these samples represent an age equivalent to Terreneuvian Series, Stage 2 (approximately middle of Stage 2) according to the regional biostratigraphy (Fig. 4).

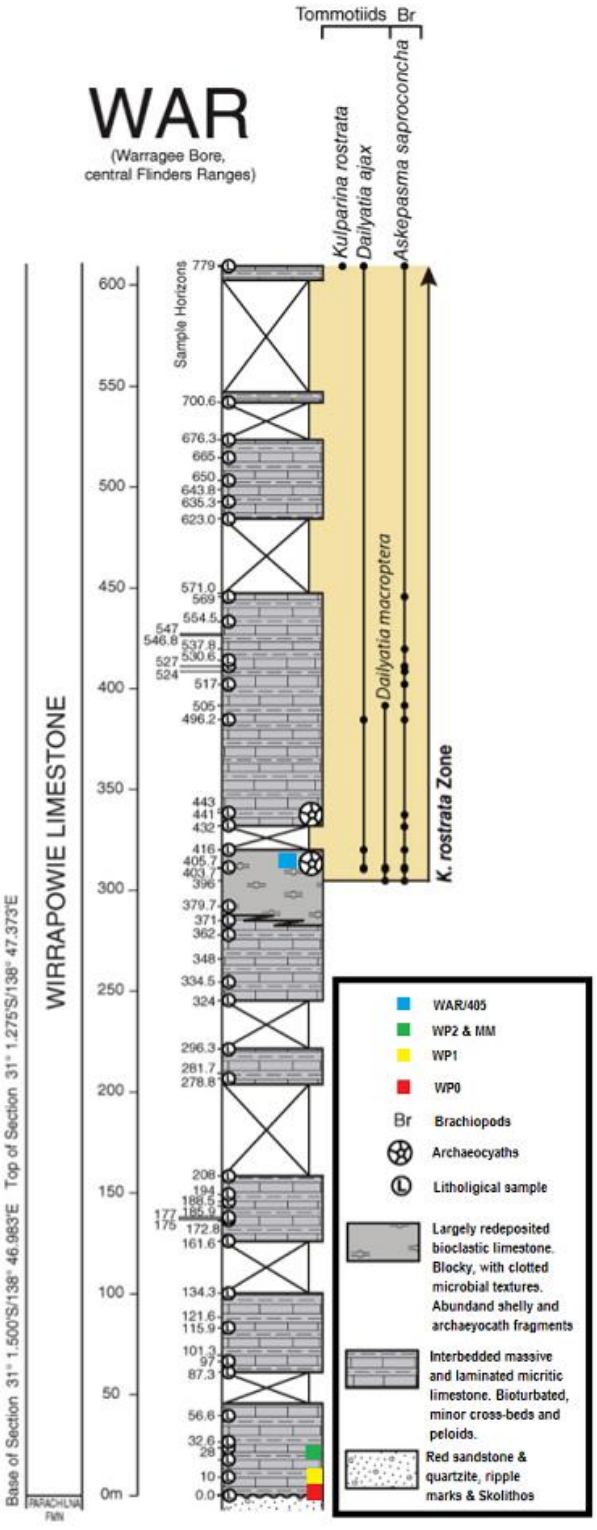

Figure 6. WAR stratigraphic section modified from Betts et al., (2016). Samples WP0, WP1, WP2, MM and WAR/405 were taken for this study.

Sample WAR/405 is located approximately 310 m above the base of the WAR section (Figs 5 and 6) in a thin sliver of shallow platformal limestone, interpreted to be Wilkawillina Limestone interfingering with the Wirrapowie Limestone or, possibly a shallow patch of bioherm within the Wirrapowie Limestone. This locality yields shelly fossils including large specimens of the paterinid brachiopod *Askepasma saproconcha* (Topper et al., 2013), as well as the

tommotiids *Dailyatia ajax* (Bischoff, 1976) and *D. macroptera* (Tate, 1892) and indeterminable archaeocyath fragments. This fauna is part of the *Kulparina rostrata* biozone (Figs 4 and 6) of Betts et al. (2016), and equivalent to a Terreneuvian Series, Stage 2 age.

2.2 Locality 2 - Wirrealpa Limestone, Bunkers Range

2.2.1 Sample Details and Locations

The TH (= Thrombolite) samples were collected along a 12m stratigraphic transect with a base at S31°05'37.7" E138°53'47.3" (Figs 7 and 8). Samples were collected at 4.15 m, 5.2 m, 8.2 m, 9.7 m and 11.8 m above the base of the transect (Fig. 8) with an adjacent oncolitic sample [SSWTH] collected along strike at S31°05'54.2" E138°53'36.3", approximately 450 m to the south west of the TH Locality (Fig. 7). The TH and SSWTH samples were collected from near the hinge zone of the of the Wirrealpa Syncline (Fig. 7), where they would be the least deformed. TH samples were taken from the base of the cliff (4.15 m) below the base of thrombolitic growth from branching to sub-parallel columns of thrombolites that are up to 8 m high and vary between 300 mm and 1 m in width. James and Gravestock (1990) interpreted these numerous metre-sized build-ups in the NW region of the Old Wirrealpa Mine to be composed of thrombolites consisting of an intergrowth of *Renalcis.*

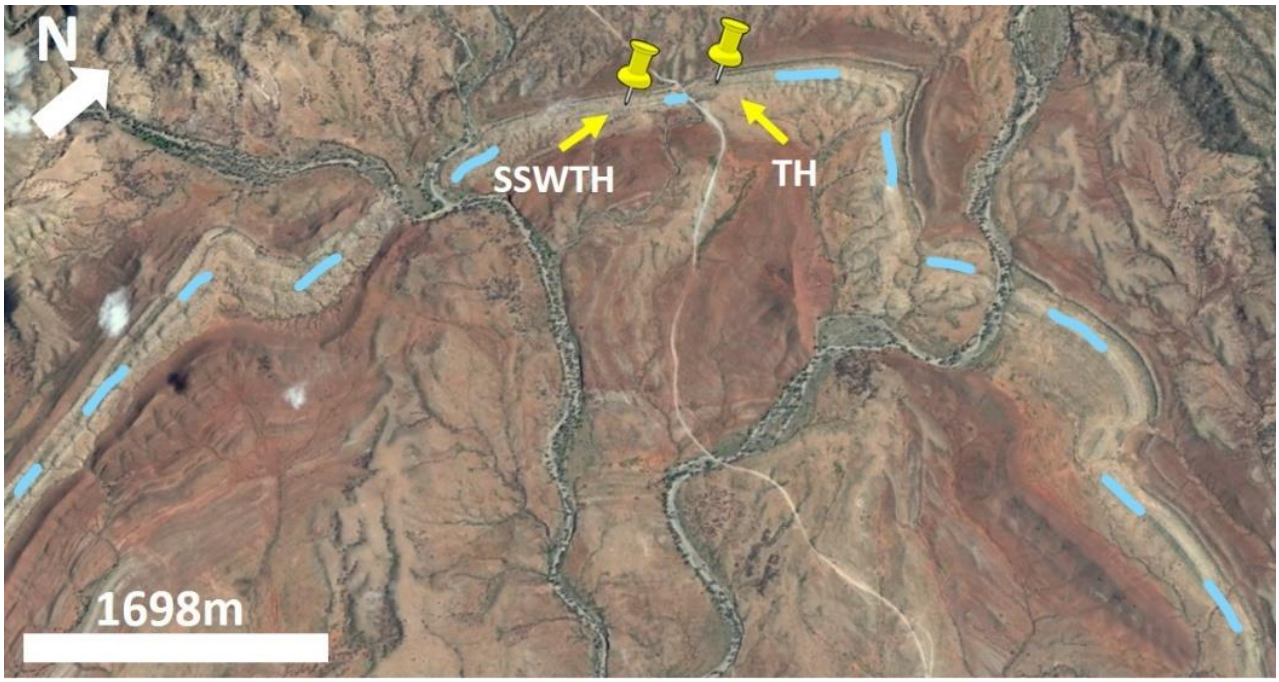

Figure 7. Google Earth image showing where Locality 2 samples were collected from the hinge of the Wirrealpa Syncline where the Wirrealpa Limestone crops out (blue dashed line). TH indicates the location where samples from giant 6-7 m thrombolites were collected. SSWTH is the location from which a large oncolitic sample was collected.

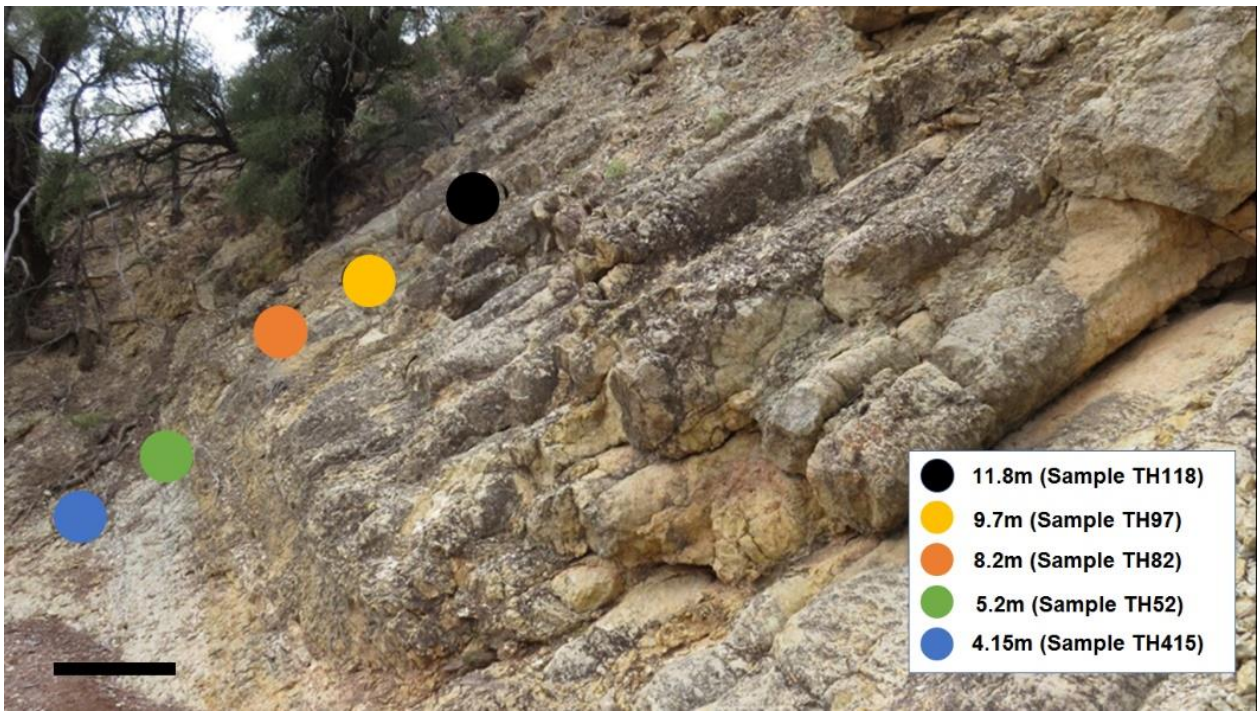

Figure 8. TH - Thrombolite cliff, with coloured dots indicating where each sample was collected for analysis and description. Scale bar = 1 m.

2.2.2 Geological setting

The Wirrealpa Limestone represents the youngest shallow marine carbonate unit in the Cambrian of South Australia. The formation crops out over a wide area across the Wirrealpa Hinge Zone in the Flinders Ranges (Gravestock and Cowley, 1995) and is a very useful stratigraphic marker for regional mapping of Cambrian units across the Arrowie Basin (Youngs, 1977; Brock and Cooper, 1993). The stratigraphy and sedimentology of the Wirrealpa Limestone was carefully documented by Youngs (1977), whilst Brock & Cooper (1993) described the shelly fossils and Kruse (1991) the archaeocyaths and radiocyaths. The Wirrealpa Limestone has a thickness ranging between 105-140 m, and the main area of outcrop is a 25-km tract of gently folded north-south striking, nodular and well-bedded, bioclastic carbonates in the Bunkers Range-Wirrealpa area (Youngs, 1977; Brock and Cooper, 1993). The Wirrealpa Limestone comformably overlies the red beds of the Billy Creek Formation and is comformably overlain by the micaceous shales, siltstones, and sandstones of the Moodlatana Formation (Brock and Cooper, 1993; Paterson and Brock, 2007). The Wirrealpa Limestone is a transgressive-regressive carbonate sequence which has two megafacies: lagoonal and ooid-bank (Youngs, 1977). The lagoonal facies association is characterised by lime mudstone and wavy-bedded to nodular limestone in a calcareous silty matrix, with subordinate skeletal, peloidal and oolitic beds, calcmicrobe build-ups, and stromatolite and columnar thrombolite bioherms. The ooid-bank facies association predominantly consist of oolitic and oncolytic lithologies (Fig. 9; Youngs, 1977).

2.2.3 Age

An ash bed located in the Warragee Member of the underlying Billy Creek Formation positioned stratigraphically ~40 m above the base of the formation has recently been dated using U-Pb isotope dilution thermal ionisation mass spectrometry (ID-TIMS) geochronology as 512.174 +/- 0.146Ma [95% c.i.] (Brock, 2017). This indicates that this level correlates with the upper part of Cambrian Series 2, Stage 4 based on the 2017 geological timescale (International Commission on Stratigraphy, 2017). The base of the Wirrealpa Limestone occurs approximately 850 m above this level (Moore, 1980). Based on sedimentation rates in the siliciclastic dominated Billy Creek Formation, this would indicate the transgressive event associated with the deposition of the carbonates of the Wirrealpa Limestone is likely to correlate with Cambrian Series 3, Stage 5 (traditional Middle Cambrian in the old nomenclature). Based on shelly fossils and the occurrence of the calcitic brachiopod *Trematobolus* sp. low in the unit, Brock and Cooper (1993) indicated a late early Cambrian (Toyonian-equivalent) age for the Wirrealpa Limestone. Paterson and Brock (2007) reported that *Redlichia guizhouensis* occurs throughout the Wirrealpa Limestone (WL section) at Balcoracanna Creek. This species correlates with the latest Lungwangmiaoan Stage in South China (Lu et al., 1974; Yin and Li, 1978; Zhou and Yuan, 1980; Peng and Babcock, 2001), which suggests that the Wirrealpa Limestone is of similar age. Zhang (2003) and Jell (in Bengtson et al., 1990) both considered that *R. guizhouensis* may be a synonym of *R. nobilis*, (Walcott, 1905), suggesting that the *R. guizhouensis* Zone is equivalent to the *R. nobilis* Zone of China. The thrombolitic samples (indicated with the prefix TH) and oncolitic samples (SSWTH) are located approximately 55-60 m above the base of the Wirrelapa Limestone (Fig. 9) which would correlate to a position low down in Series 2, Stage 4 (traditional middle Cambrian).

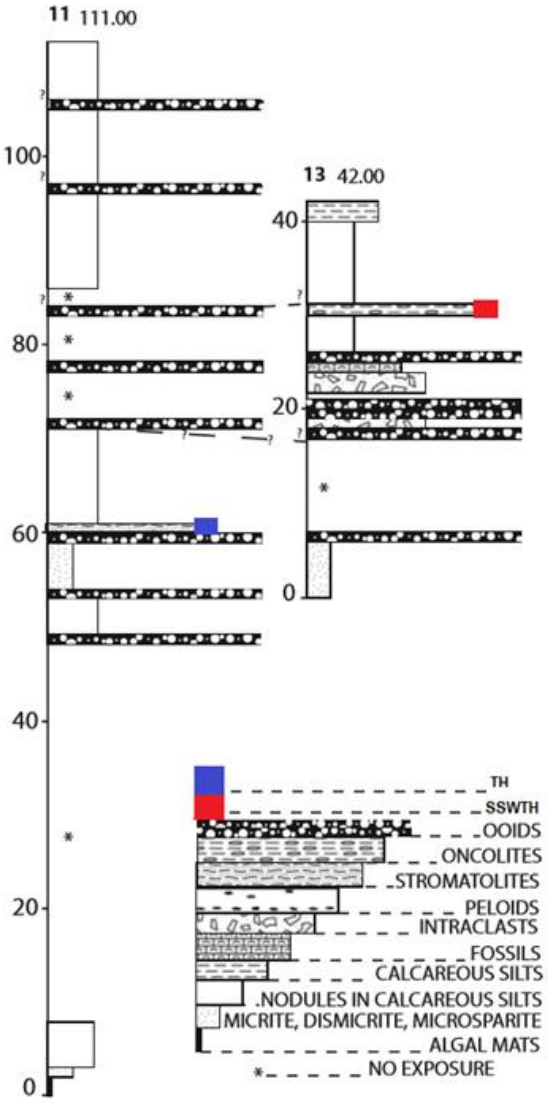

Figure 9. Stratigraphic log altered from Youngs (1977). TH indicates the location where samples from giant 6-7 m thrombolites were collected. SSWTH is the location from which a large oncolitic sample was collected.

3. Methods

3.1 Organic Geochemistry

3.1.1 Contamination prevention

A mixture of dichloromethane (DCM, Honeywell) and methanol (MeOH, Honeywell) (9:1 v/v) was used to extract organic compounds from the samples. All solvents and glassware were first checked for purity with a solvent blank by gas chromatography-mass spectroscopy (GC-MS) as described below. All glassware was cleaned in Decon90 solution, washed with Millipore water, and combusted in an oven at 400°C for 3hrs before use. All glassware was stoppered or covered with foil to prevent laboratory contamination (Illing et al., 2014). Blanks were utilised where possible to eliminate possible contaminants; blanks were taken on the rotary evaporator, the Accelerated Solvent Extractor (ASE), representative glassware, and the pre-extracted and combusted sand that was used on the rock crusher. In addition, a basalt blank was cut using the rock saw.

3.1.2 Sample Preparation

The outer surfaces of the samples were removed using a Buehler Isomett 4000 precision saw with a diamond blade, and the inner parts were cut to approximately 1– 1.5 cm rectangles. Weights ranging from 100 g to 200 g, except for the smallest sample 'MM' (54 g). Fine particles on the rock surfaces were removed by ultrasonication in Millipore water for two cycles of 10 minutes. The samples were placed in beakers and covered with a mixture of DCM and MeOH (9:1 v/v). The beaker was sonicated for two cycles of 10 minutes, and rested for 5 minutes in between. The solvent was decanted into a round bottom flask. This outside rinse solution was reduced by rotary evaporator until less than 2 mL remained, and was then transferred by pipette into a 2 mL vial. The vial was spiked with three compounds as internal standards by adding 1 mL of a DCM solution (solution-1) containing about 5 ng each of anthracene-d10 (98 atom%D, Isotec), p-terphenyl-d14 (98 atom %D, Isotec), and tetracosane-d50 (98 atom %D, Isotec). The outside rinse was then checked to ensure there were no contaminants by GC-MS. Once the chromatograms obtained from the GC-MS were checked, the samples were crushed with a tungsten carbide ring mill crusher. The crusher was cleaned with Millipore water and ethanol between each use and a blank was taken to ascertain purity levels before any crushing took place. 5 g of the powder was separated and put aside for FTIR and other analyses.

3.1.3 Solvent extraction (Bitumen I Extract)

A blank was taken through the Accelerated Solvent Extractor. However due to contamination levels in the blank (due to small inter-sample carry-over from the tubing) this instrument was not further used in this study, and instead hydrocarbons were extracted by sonication. The rock powder was

solvent extracted using a mixture of DCM and MeOH (9:1 v/v) by sonication for 10 minutes, resting for 5 minutes, and sonication for a further 10 mins. Between each sonication the solution was stirred and left to resettle for 5 minutes. The solvent solution was then decanted into a round bottom flask and the process was repeated twice more for each sample. The second and third solvent mixtures were added to the first for each sample. Before rotary evaporation a blank was performed and the machine was checked to be free of contamination. The collected solvent mixtures were reduced by rotary evaporation to ~40 ml. The samples were centrifuged, to remove fine rock particles, at 2000 rpm for 10 minutes and then the solution was decanted into round bottom flasks. If, after centrifuging, there were still fine particles suspended in the mixture, the mixture was filtered through silica gel (silica gel 60, 0.063-0.200mm) which was activated at 120 °C for >4 hours before use. The extractable organic matter (EOM) solution of each sample was then reduced using rotary evaporation until <2 mL remained, and then transferred by pipette to a 2 mL vial. The solution was spiked with the standard solution-1, further evaporated by hot plate and nitrogen blow down and pipetted into a 100 μL vial insert and then analysed by the GC-MS, without prior fractionation, so as to prevent the loss of hydrocarbons.

3.1.4 Second solvent extraction (Bitumen II Extract)

After the first solvent extraction, the residual rock powder was treated with hydrochloric acid (4 M) to remove the carbonate minerals. Initially a 1 M HCl solution (100–150mL) and eventually a 4 M HCl solution was added to the powder on a hot plate at 70°C until the addition of acid produced no further reaction. The resultant solution was washed with 500 mL of filtered water 12-15 times, and tested with a pH indicator. The surplus acid-water mixture was discarded, and the remaining powder slurry was dried in a drying oven. Extraction of the decarbonated rock powder was performed as described above for the first extraction. A basalt blank was also put through this process, but there was no significant contamination.

3.1.5 Gas chromatography-mass spectrometry

GC-MS analysis was carried out on an Agilent gas chromatograph (6890N) coupled to an Agilent mass selective detector (5975B). A 1 μL portion of the EOM solution was injected into a programmable temperature vaporisation (PTV) inlet operating in splitless mode with a J&W DB5MS capillary column (length 60 m, inner diameter 0.25 mm, film thickness- 0.25 μm). Helium was used as the carrier gas (1.5 mL/min, constant flow), and the temperature of the GC oven was ramped from 40°C (2 min isothermal) to 310°C (30 min isothermal) at a rate of 4°C/min. The MS data were acquired in scan (m/z 50 to 550) and single ion monitoring modes. Hydrocarbon identification was based on comparisons of relative GC retention times and mass with previously reported. Semi quantitative analyses were performed in which solution 1 was used as an internal

standard.

3.2 Other Geochemical analyses

3.2.1 FTIR

For FTIR (Attenuated Total Reflection (ATR)) analysis, a small amount of non-extracted rock powder was placed onto the sample platform of the instrument (a Nicolet iS10 ATR-FTIR; Thermo Scientific). Prior to analysis, the FTIR instrument was purged with N_2 gas until the signal stabilised for a background reading, which was taken off the clean platform surface prior to loading the catalyst sample. The spectra were acquired in a wavenumber area between 4000 and 500cm^{-1} with 64 accumulations and a spectral resolution of 4cm^{-1} wavenumbers. The background was corrected in air between sample collections. Data acquisition used the Omnic Spectra Software (Thermo Scientific).

3.2.2 Raman Spectroscopy

Raman spectra were collected on the black clots and clasts seen in thin section. It is preferable to study these materials in thin section rather than bulk powders because natural carbonaceous materials are generally disordered, but more importantly, are structurally, microtexturally, and texturally heterogeneous (Allwood et al., 2006). Care was also taken to target dense black material that is part of the primary rock fabric, avoiding material in cross-cutting (younger) veins. A 633nm (red) wavelength laser was used with a Horiba Jobin Yvon LABRAM HR (high resolution) Evolution confocal laser Raman system. The spectrometer was equipped with an integrated Olympus BX41 optical microscope with an automated x-y stage. A 10x long-distance objective was used. The system was initially checked for calibration using the 520.7 cm^{-1} band of a silicon wafer. A grating of 1800 grooves/mm was selected for maximum spectral resolution. Spectra were collected over a duration of 3-5 minutes and averaged over at least 2 accumulations for spectral clarity. This method was repeated on 2-3 spots per thin section. Data acquisition and spectra treatment were carried out with the commercially available program LabSpec v6 (HORIBA Jobin Yvon GmbH). Multiple analyses were performed on each thin section on carbon clots a few mm away from one another.

3.2.3 micro-XRF

Micro-XRF data was collected on the following samples; WP1, a horizontal cut of WP2 with MM attached, TH52, TH97, TH118 and SSWTH. Analyses were carried out using a Bruker M4 Tornado micro-XRF equipped with a Rh anode tube that was operated at 50 kV and 40 mA, and dual Bruker silicon drift detector energy dispersive spectrometers. The poly-capillary X-ray optics were able to analyse 25-μm spot sizes. The Advanced Mineral Identification and Characterisation System (AMICS) software (Bruker Corp., Billerica, MA, U.S.A.) compared the X-ray spectra from each

pixel with spectra from pure mineral standards and assigned a mineralogical identity to each pixel. Micro-XRF maps were generated using the Bruker M4 Tornado acquisition software and were acquired at 100 μm steps with a 25 μm spot size. Some higher resolution maps were taken at 20 μm steps with a 25 μm spot size. The minimum dwell time per point was 25 ms unless otherwise stated.

3.3 Morphological Analyses

3.3.1 Polished blocks and thin sections

Offcuts from organic geochemical analysis were labelled with way-up orientations. Each sample was separated into two for further morphological analysis. Small rock saw cuts were used to produce small blocks suitable for standard 30 μm thin sections. The larger blocks were polished using increasingly finer grades of wet/dry sandpaper (240-2200μm).

4. Results.

4.1 Morphological and Petrographic Descriptions

Both macro- and microscopic investigation of the sampled carbonates from both locations showed allochems occurring in varying quantities and in many samples, carbonate-replaced extraclasts set in a recrystallised, micritic-microsparitic dolomitic matrix. The allochems described include intraclasts, peloids, and stromatoclasts. All samples are classified using the Dunham scheme.

4.1.1 Locality 1. WAR Section, northern Bunkers Range

WPO - Peloidal grainstone

Morphology: There were only small off cuts remaining after organic geochemistry, so no polished slab was made.

Petrography: WP0 has a homogenous, peloidal allochem grain-supported fabric (Fig. 10A). The peloids are well-sorted, ovoid and equally sized (~2 μm) (Fig. 10A). There are rhombic crystals present. Stylolites are filled with secondary iron precipitates. There are some quartz grains in the matrix which exhibit undulose extinction and there are 2 poikiloblasts present in thin section (e.g. Fig. 10B). Three secondary veins of carbonate cross-cut the thin section lengthways (Fig. 10C).

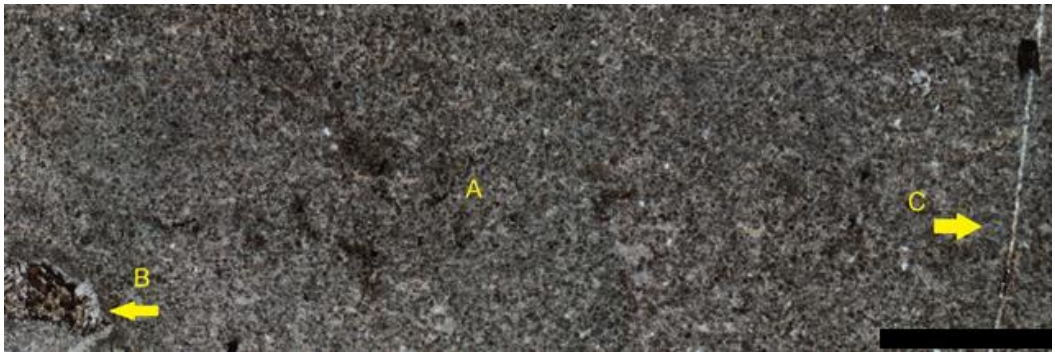

Figure 10. Thin section photomicrograph of Sample WP0. A. peloidal matrix; B. poikiloblast; C; a secondary vein. Scale bar is 2.0 mm.

Sample WP1: Laminated fine-grained cm-wide agglutinated columnar stromatolites, overlying a flat pebble conglomerate.

Morphology: Sample WP1 is a tabular intraclastic flat pebble (carbonate) conglomerate which has been overgrown by columnar stromatolites that range in height from 0.7 – 2.0 cm (Fig. 11A). In hand specimen, the intraclasts (Fig. 11B) are varying shades of orange-brown and range in shape from tabular to coniform with a size range from 0.2 - 1.4 cm. The clasts appear to occur, or were possibly injected, between adjacent very finely layered columnar stromatolites, and are primarily oriented with a mostly vertical major axis. However, some clasts do not conform to this orientation and appear on a between 0-45° slant. The stromatolites consist of alternating layers (~0.8 µm thick) which are well defined, and distinct boundaries are clearly observed.

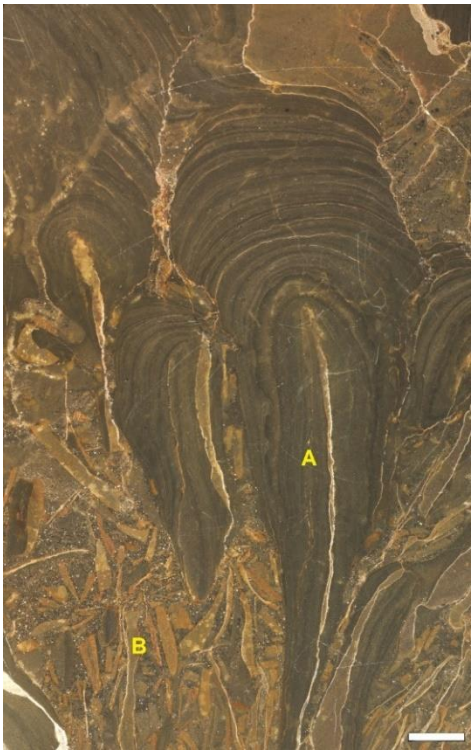

Figure 11. Photograph of the hand specimen of WP1. A. columnar stromatolites; B. flat pebble intraclasts. Scale bar is 5.0 mm.

Petrography: Small black crystals (0.2 - 0.4 µm) are dispersed within the laminae of the stromatolites (Fig. 12A). Subrounded to subangular intraclast debris occur throughout the sample. There are rhombic ghosts (Fig. 12B), that appear to be an artefact of contamination. Stromatolitic laminations transform from fine-scale (Fig. 12C) to clotted (Fig. 12D) and back to fine-scale (Fig. 12E). There are un-laminated layers of fine-grained material (micrite) that appears to 'blanket' the stromatolites, in-filling the space between the stromatolites (Fig. 12B). The laminae gradually become more undulose and eventually grade back into stromatolites with low domical relief. Fragmentary bioclasts in the micritic matrix consist mainly of hollow recrystallised sclerites with faceted knob-like terminations, which narrow and taper to a distal tip.

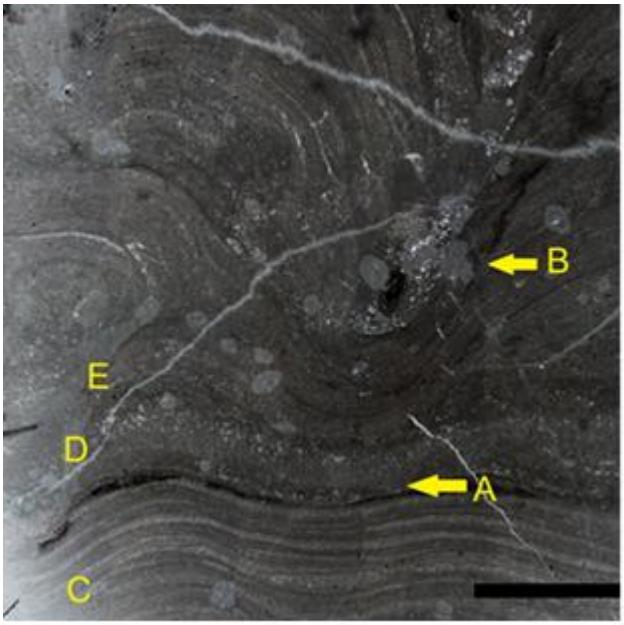

Figure 12. Thin section photomicrograph of WP1. A. dark crystals in laminae; B. contamination; C. finescale laminations; D. clotted laminations; E. finescale laminations. Scale bar is 2mm.

These most likely are isolated rays from chancelloriid sclerites (Fig. 13A), which occur throughout the matrix. Their fragmentary character indicates an allochthonous origin.

Sample WP2 and MM (microbial mat): WP2: Peloidal grainstone, **MM:** Laminated microbial mat

Morphology: The polished slab has a distinct lower and upper part. The lower part (Fig. 14, WP2) consists of fine scale (1 mm) finely laminated bedding made up of micritic carbonates with fine quartz grains and horizontally aligned hexactinellid sponge spicules (Fig 14A). The contact between the overlying microbial mat (MM) and underlying spicultic bedding is distinct (Fig 14, contact). The microbial layers (MM) are undulose, mound forming and more finely grained than the WP2 microlayers.

Petrography: The matrix of WP2 (Fig. 15 WP2) consists of dark circular to elliptical grains in cross section and averaging about 0.1 mm in diameter. There are intraclasts of carbonate within a micritic matrix; quartz grains vary from angular to subangular; monaxon spicules appear to be broken and fragmented but long axes are generally aligned parallel to bedding (Fig. 15A). The microbial contact (Fig. 15 Contact) has a clearly defined dark line which appears to be a thin iron-rich layer (possibly a firmground). The MM section is heterogenous, and the microbes grow over clots (Fig. 15B) in round build-ups. The microbial interactions transition between the clots and fine scale matrix (Fig. 15 Above and below B).

Sample WAR/405: Archaeocyath framestone

Morphology: The limestone matrix (Fig. 16A) is grey to blue in colour with micritic to relatively course rubble-like matrix. The fabric of the biohermal sample is primarily composed of fragmentary, overturned and largely transported archaeocyaths (Fig. 16B), with some (possibly) dendritic calcmicrobial fragments throughout (Fig. 16C).

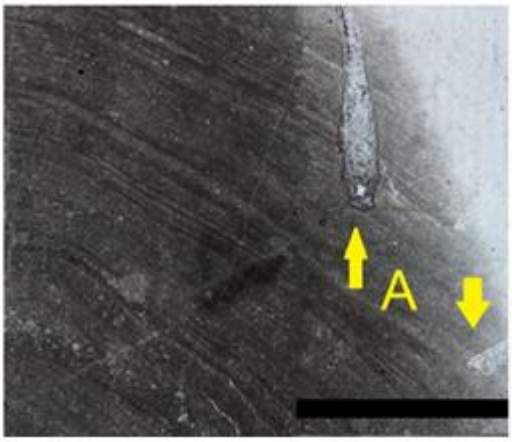

Figure 13. Thin section photomicrograph of WP1. A. fossilised shells. Scale bar is 2 mm.

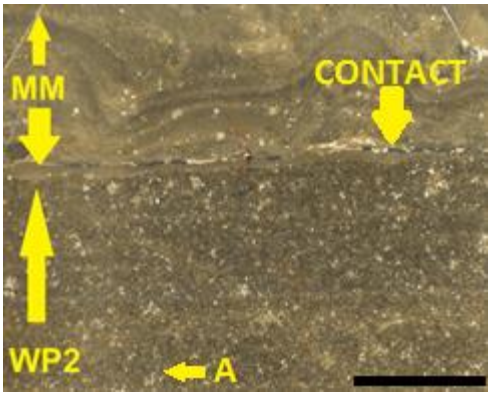

Figure 14. Photograph of the hand specimen of WP2 and MM. A. sponge spicules. Scale bar is 1cm.

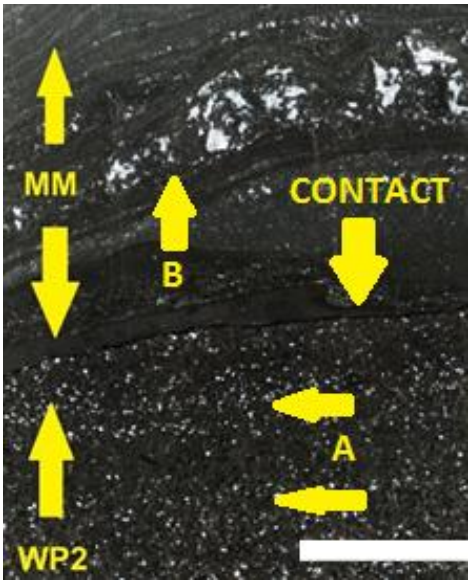

Figure 15. Thin section photomicrograph of WP2 and MM. A. monaxon spicules in matrix; B. coarse grained material with microbial overgrowth. Scale bar is 2mm.

Petrography: Peloidal grains infill void space between archaeocyaths (Fig. 17A). Mosaics of rhombic crystals are characteristic of this sample (Fig. 17B) and, possibly syndepositional, spar recrystallisation mixed with micrite. Stylolites (Fig. 17C) form boundaries surrounding matrix changes throughout the sample. Some archaeocyaths have microbial rinds surrounding them.

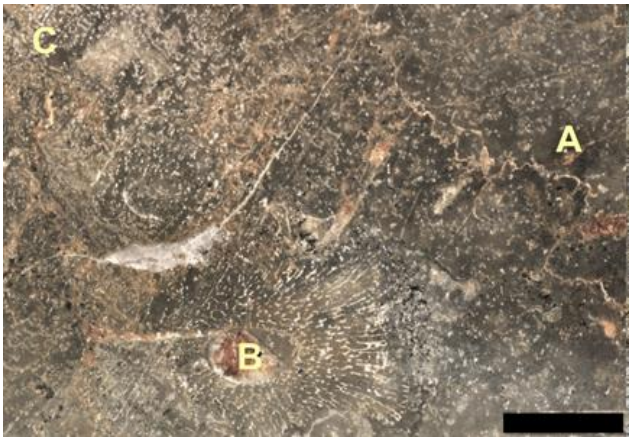

Figure 16. Photograph of the hand specimen of WAR/405 in hand specimen. A. limestone matrix; B. archaeocyath; C. dendritic fabric. Scale bar is 1 cm.

4.1.2 Locality 2. Wirrealpa Limestone, Bunkers Range

Thrombolite Hill, 4.15 m above base of the section:

Morphology: Small off cuts were sufficient only for organic geochemistry, so no polished slab was made. The sample was collected in a layer directly beneath thrombolitic mounds (Fig. 3).

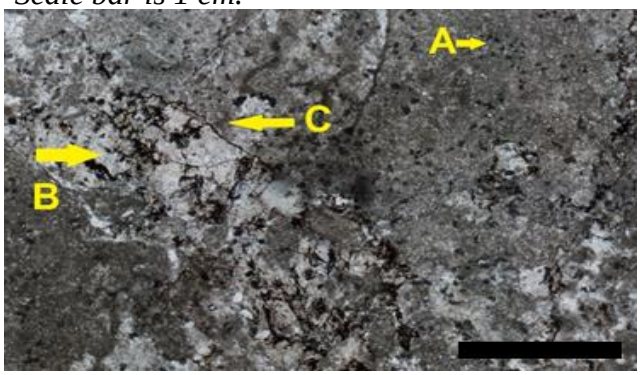

Figure 17. Thin section photomicrograph of WAR/405. A. peloids; B. rhombic crystals; C. stylolite. Scale bar is 1 mm.

Petrography: Sample has a calcite spar matrix, dominated by bioclasts (Fig. 18A). Bioclasts include brachiopod shell fragments (? *Trematobolus*) (Fig. 18B) and siliceous monaxons entrained throughout. Additionally, there are ladder-like bioclasts belonging to indeterminate archaeocyaths.

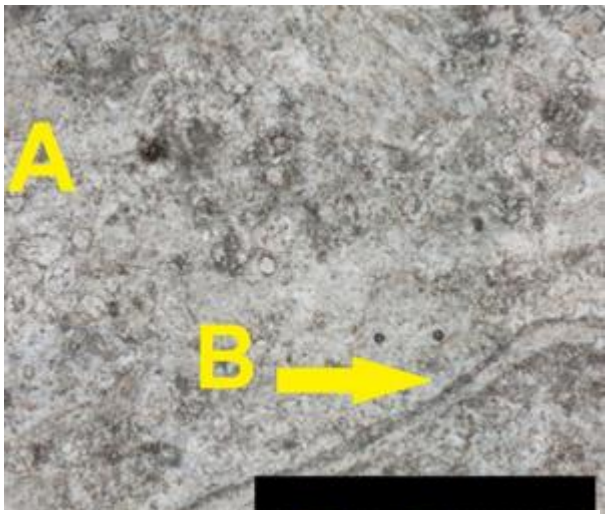

Figure 18. Thin section photomicrograph of TH415. A. bioclastic matrix; B. large shell fragments. Scale bar is 2mm.

Samples TH5.2, TH97 and TH118 Name: Coarse Agglutinated Thrombolites, after the classification structure developed by Riding (2000).

Samples TH5.2, TH97 and TH118

Mesostructure Morphology: Thrombolites have a similar mesostructure throughout their growth. Both depositional and diagenetic processes are present: a depositional microclotted fabric (Fig. 19A) with diagenetic clay infills (Fig. 19B). These features are apparent in polished hand specimen but not easily distinguishable in outcrop.

The clotted thrombolitic fabric is dark brown, and the clays are light brown. Individual clots occur irregularly, but some are connected and have an incipient digitate and columnar form with some laminae (which may be old growth surfaces) present in columns with replaced clay-like material (Fig. 19C). Clots vary from 2.0 mm to 3.0 cm in diameter. Clay infills are irregularly shaped, spaced and sized within accommodated void space.

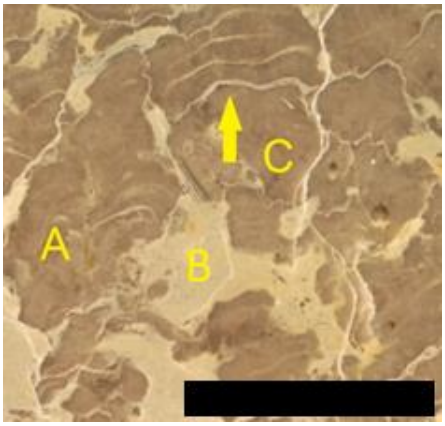

Figure 19. Hand specimen of TH97 showing representative thrombolitic mesostructure. A. clotted fabric; B. clay infills; C. incipient columns with clay replaced laminae. Scale bar is 1cm.

Thrombolite Hill, 5.2 m above base of section:

Petrography: An intra-bioclastic limestone. Spar has formed rosette arrays (possibly aragonitic pseudomorphs) around microbial precipitates (Fig. 20A). Some tubiform biolclasts, likely belonging to hyolithelminthid tubes (Fig. 20B), are entrained throughout the matrix, and secondary dogtooth calcitic crystals infill void space. Abundant isolated eocrinoidal columnals and partial stem fragments (Fig. 20C) occur throughout the matrix (5-10%).

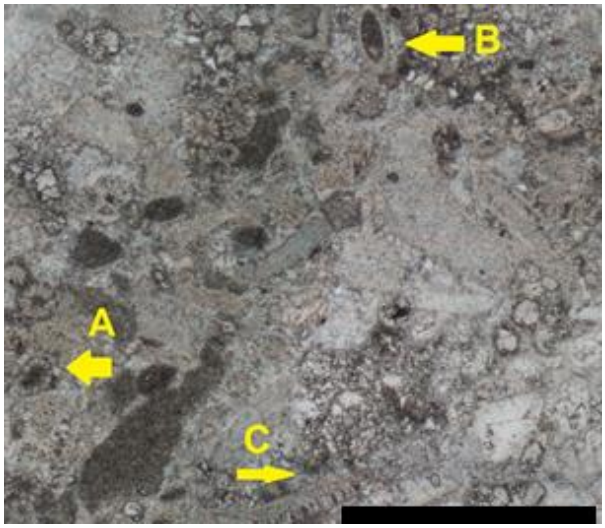

Figure 20. Thin section photomicrograph of TH52. A. spar rosettes; B. indeterminate tubes; C. stem fragment. Scale bar = 2 mm.

Thrombolite Hill, 9.7m above the base of section:

Petrography: This sample has a biomicrite matrix which is chancelloriid bioclast supported (Fig. 21A), and recrystallised via dissolution. There are stylolites present and the matrix is uniform throughout the thin section. Chancellorids include isolated sclerites, single rays (Fig. 21B), and recurved rays, which are diagnostic as from the chancelloriid taxon, *Archiastrella*, are extremely abundant.

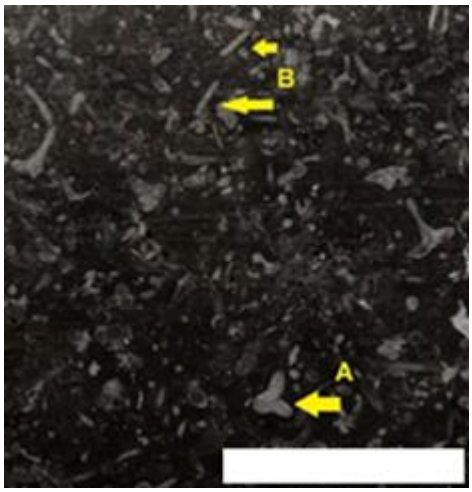

Figure 21. Thin section of photomicrograph of TH97. A. Chancelloriid sclerite; B. individual rays. Scale bar = 2 mm.

Thrombolite Hill, 11.8 m above the base of section:

Petrography: The sample has a mineral that resembles dolomite concentrated on the interiors of the rosette arrays (Fig. 22A). The mineral is associated with calcititc spar. There were previous bioclasts where the fossil has been dissolved away, and spar has filled the space (Fig. 22B).

The sample is fossiliferous and contains calcitic valves of a rhynchonelliform brachiopod (*Trematobolis* sp.*)* (Fig. 22C) and macroscopic trilobite fragments (*Redlichia* sp.*)* (Fig. 22D).

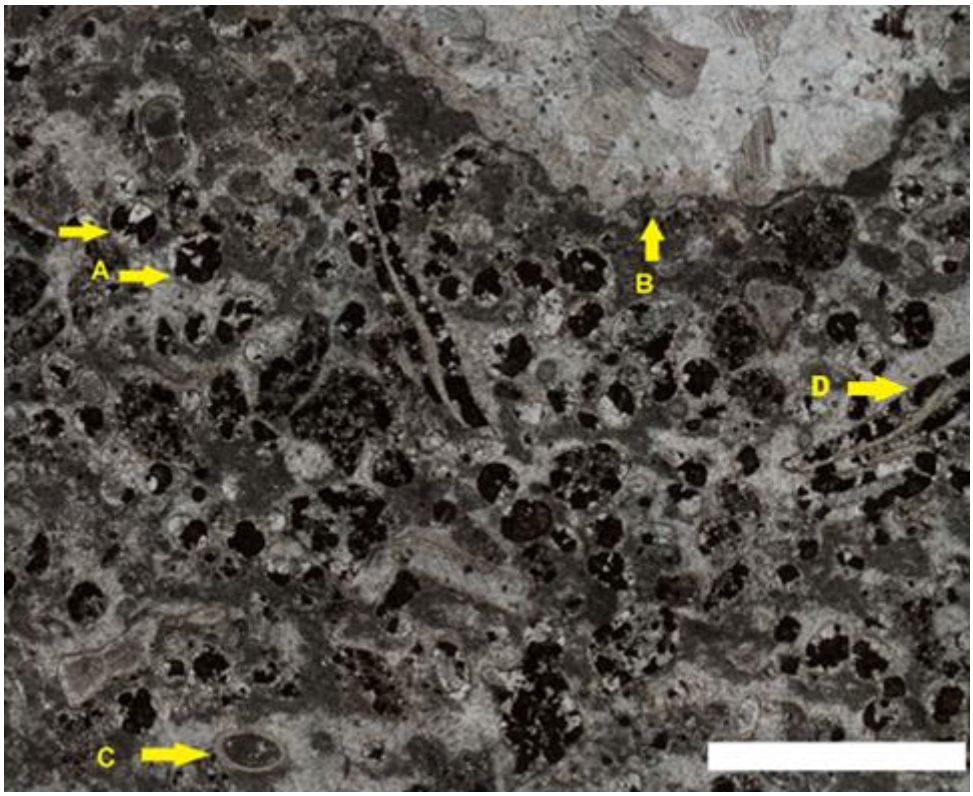

Figure 22. Thin section photomicrograph of TH118. A. spar rosettes with dolomite infill; B. a spar filled clast; C. a brachiopod shell; D. trilobite fragments. Scale bar is 2 mm.

SSWTH: Oncolitic grainstone

Morphology: The matrix consists of grain-supported bioclastic fragments of shell, tubes, spicules and trilobite fragments as well as peloids with microbial crusts forming around the material (Fig. 23A). The matrix colour ranging from a red-brown (Fig. 24A) to a grey-brown (Fig. 24B). Oncolites most commonly nucleate around trilobite pleural fragments (Fig. 24C) or chanceloriid sclerites (Fig. 24D). Oncolites range in shape from subrounded to oblate ellipsoid, and each has irregular concentric laminae with individual laminae approximately 0.5 µm thick, producing oncolites with the major length axis 1.5-2x longer than the width. The largest oncolites have a maximum length 2.9 cm, but can be much smaller than 0.1 cm. A rose diagram (Fig. 25) was created using the angle of each oncolites major diameter, that was larger than 0.1 cm, indicating that the oncolites have a north-south preferential orientation with a mean vector of 338°.

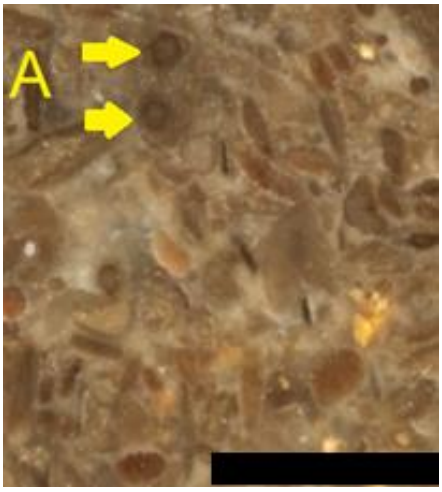

Fig. 23 Photograph of the hand specimen of SSWTH, showing the matrix. A. microbial rinds growing on peloids. Scale bar is 5mm.

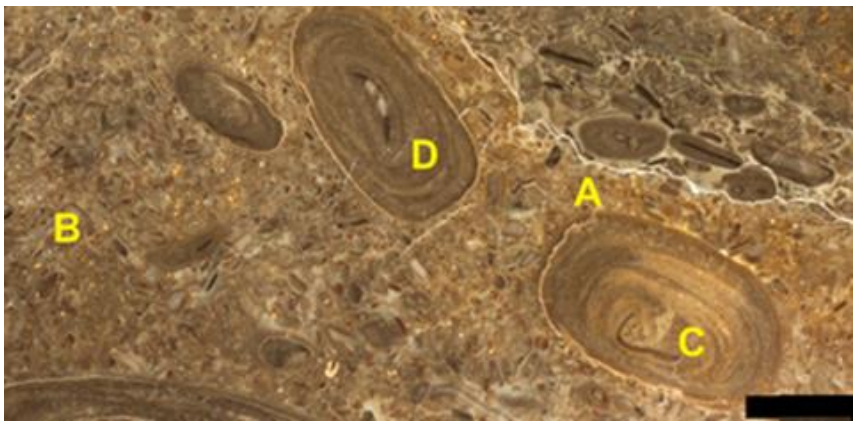

Figure 24. Photograph of the hand specimen of SSWTH. A. reddy brown bioclastic matrix; B. grey brown bioclastic matrix; C; Trilobite pleural fragment as oncolitic nucleus, D; chancellorid sclerite as oncolitic nucleus. Scale bar is 1 cm.

Petrography: The largest oncolitic concretion (8 mm) is nucleated around bioclastic material (Fig. 26A), but K-feldspar is also present in the nucleus (Fig. 26B), and pyrite occurs sporadically throughout the concretions (Fig. 26C). The matrix contains trilobite pleural fragments (Fig. 26D), brachiopods, and the matrix transitions from muddy brown (Fig. 26E) to micrite (Fig. 26F) as it does in hand specimen. The matrix has the same spar calcite rosettes growing around bacterial precipitates as found in the TH thrombolites. The trilobite sclerites are oriented in a similar orientation as the major axis of the oncolites, but most of the smaller material (<0.5mm) in the matrix has chaotic orientations.

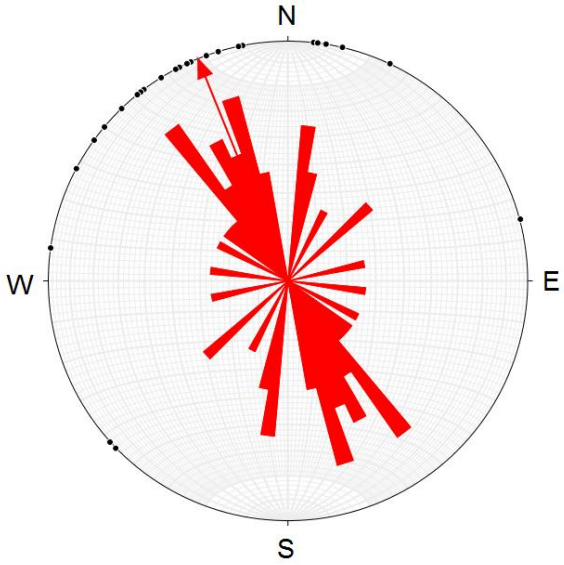

Figure 25. Rose diagram showing orientation of the longest axis of oncolites, 38 measurements were taken with a mean vector of 338°.

4.2 FTIR Results

The primary domains of biomolecules that are easily categorised by FTIR include a) proteins, peptides and enzymes, b) lipids and fatty acids that include cell membranes, c) carbohydrates and polysaccharides, and d) nucleic acids (Anderson et al., 2005). These groups have distinct infrared functional groups and wavelength ranges of absorption (Anderson et al., 2005). FTIR spectra collected from the rock powder of all samples exhibit peaks at ~712 cm^{-1}, ~872 cm^{-1}, ~1300-1500 cm^{-1}, and ~1795 cm^{-1}, which can be attributed to calcite (Figs 27, 28, S2 Reig, 2002; Kovač, 2009). Samples WAR/405, WP0, and

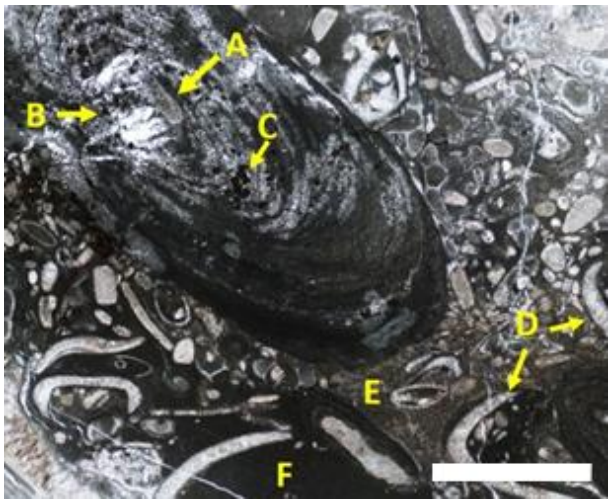

Figure 26. Thin section of SSWTH. A. Organic fossil; B. K-feldpars; C. Pyrite; D. Trilobite sclerites; E. red-brown matrix; F. dark brown micritic matrix. Scale bar is 2mm.

WP2 from Locality 1 (Fig. 29), and TH415, TH52, TH118 and SSWTH from Locality 2 exhibit a peak at ~2511 cm^{-1}, which can also be attributed to calcite (Gunasekaran et al., 2006). The absorption band at ~2520 cm^{-1} occurs because of the HCO_3 group vibrational mode that arises inside a carbonate crystal lattice or in the interface between a mineral and an organic, and is directly related to the peak at ~1795 cm^{-1} which is a part of the carbonate group vibrational mode (Preston et al., 2014). A doublet of peaks occurs in all samples at ~780 cm^{-1} and ~800 cm^{-1}, which can be attributed to silica (Reig, 2002). The large broad band centred between 1397-1405 cm^{-1} occurs because of the asymmetric C-O stretching modes and is related to the weak bending mode frequencies around 700 cm^{-1} and 785 cm^{-1} (Mastandrea et al., 2011). These bands inhibit clear assignment of organics that inhibit the same wavenumbers as samples in the mineral matrix, and create strong interference between the geological bands and the organic bands, particularly when there is low OM content (Mastandrea et al., 2011). All samples produce peaks between 1000-1150 cm^{-1} which is the main region for carbohydrate peaks (Mastandrea et al., 2011). The band at ~1085 cm^{-1} , which is present in varying pronouncements in all samples, could be attributed to quartz or polysaccharide components (Schmitt and Flemming, 1998; Innocenzi et al., 2003). These peaks have shoulders on the high wavenumber side, which could indicate the presence of siloxanes due to the Si-O stretching vibrations of the SiO_4 tetrahedra (Mastandrea et al., 2011). Additionally, there are two weak aliphatic carbon-hydrogen (C-Hx) methylene stretching modes (2875.56 cm^{-1} and 2983.04 cm^{-1}) in sample WP0 (Fig. 29). These peaks may not be real, as there are no related peaks in Fig. 27.

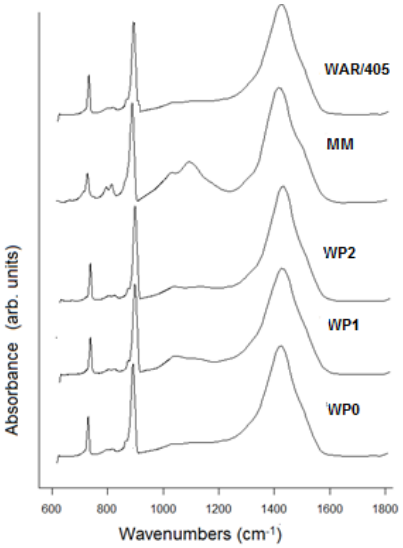

Figure 27. Absorbance FTIR spectra between 600-1800 cm^{-1} for the samples WP0, WP1, WP2, MM and WAR/405 from locality 1.

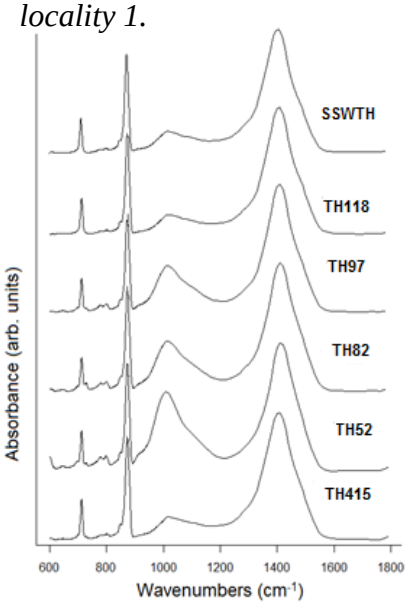

Figure 28. Absorbance FTIR spectra between 600-1800 cm^{-1} for the samples, TH415, TH52, TH82, TH97, and SSWTH from Locality 2.

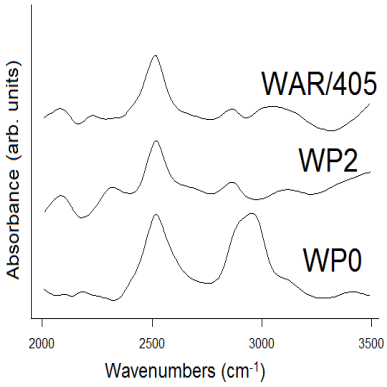

Figure 29. Absorbance spectra between 2000-3500 cm^{-1} for samples WP0, WP2 and WAR/405 from Locality 1.

4.3 Raman Results

All samples have typical calcite bands at 157 cm^{-1}, 715 cm^{-1}, 1047 cm^{-1} and 1361 cm^{-1} (Figs 30 and 31) (Gunasekaran et al., 2006; Wehrmeister et al., 2010; Wehrmeister et al., 2011; De La Pierre et al., 2014). All samples have a band at 258 cm^{-1} which is indicative of the beginnings of dolomitisation (Gunasekaran et al., 2006; Sun et al., 2014), although it was less pronounced in WP0 and WP1, and the samples from Locality 2. There are marked differences between the collective spectra from Locality 1 and Locality 2, and there is generally less intensity in any peak from Locality 2. The 157 cm^{-1} and 715 cm^{-1} peaks of every sample from Locality 2 are much smaller and less pronounced, and the peak at 258 cm^{-1} gets smaller with sample height up the section, and is the least prominent in the SSWTH sample (Fig. 31).

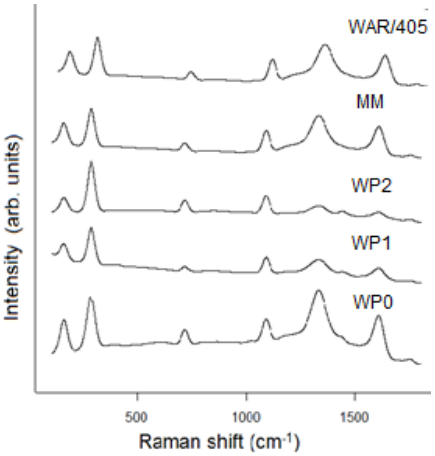

Figure 30. Raman spectra between 0-1800 cm^{-1} for the Locality 1 samples WP0, WP1, WP2, MM, and WAR/405.

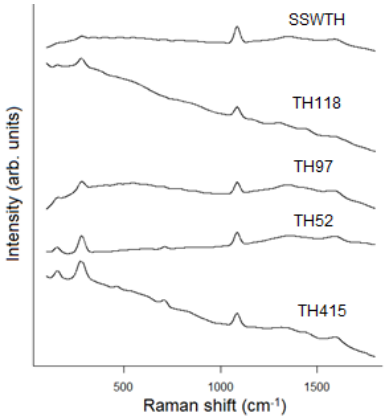

Figure 31. Raman spectra between 0-1800 cm^{-1} for the Locality 2 samples, TH415, TH52, TH97, TH118, and SSWTH.

The WP0, WAR405, MM, TH415, TH52 and TH118 samples have a peak at 1436 cm^{-1}. WP1 also has this peak but it is much larger and has a shoulder (Figs 32 and 33). This peak has previously been attributed to an additional calcite peak which occurs in single crystalline calcite (Krishnamurti, 1957) and single crystal aragonite (De La Pierre et al., 2014). Furthermore the WAR405, WP0, WP1, MM, TH415 and TH52 samples have an additional peak at ~1750 cm^{-1} (Figs 32 and 33), which has previously been attributed to both calcite (Krishnamurti, 1957) and epigraphene (Ferralis, 2010; Rajput et al., 2014). The latter can occur when graphene grows on SiC surfaces (Ferralis, 2010).

All samples from Locality 1 have prominent D_1 band (1350 cm^{-1}) and G band (1580 cm^{-1}) (Fig. 32). These bands are also present in the Locality 2 samples (Fig. 33), but are much less pronounced. These band names are termed D_1 and G because these bands are related to disordered carbonaceous material (or defect) and fully ordered graphite, respectively (Aoya et al., 2010; Marshall et al., 2010). As metamorphic temperature increases the intensity of the D_1 band decreases relative to the G-band, and the G band becomes narrower

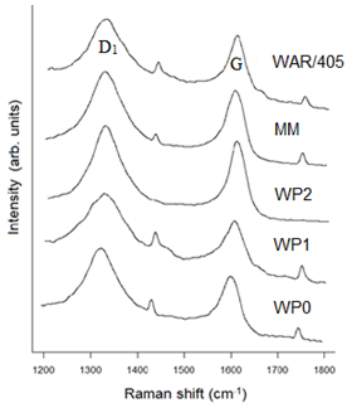

Figure 32. Raman spectra from 1200-1800 cm^{-1} for Locality 1 samples, WPO, WP1, WP2, MM, and WAR/405.

(Beyssac et al., 2002). Deconvoluted spectra were then characterised by the parameters listed in Table 1: full width at half maximum (FWHM), the intensity ratio (I_{D1}/I_G), and $I_{D1}/(I_{D1} + I_G)$ *(%)* (Beyssac et al., 2002; Allwood et al., 2006; Marshall et al., 2007). The (I_{D1}/I_G), and $I_{D1}/(I_{D1} + I_G)$ values range from 0.87 to 1.99, and 47% to 67%. respectively. These values indicate very structurally disordered carbonaceous material (Marshall et al., 2007). The FWHM is known to decrease with increasing thermal maturity (Allwood et al., 2006). Samples from Locality 1 have more noticeable D_1 and G peaks in their spectra (Fig. 32), higher intensity ratios (Table 1, Figs 34 and 35), higher $I_{D1}/(I_{D1} + I_G)$ percentages (Table 1, Figs 34 and 36) , and lower FWHM values (Table 1, Figs 35 and 36). In contrast, the Locality 2 have less prominent D_1 and G peaks in their spectra (Fig. 33), lower intensity ratios (Table 1, Figs 34 and 35), lower $I_{D1}/(I_{D1} + I_G)$ percentages (Table 1, Figs 34 and 36) , and larger FWHM values (Table 1, Figs 35 and 36). For samples from this study, there were no significant correlations found between the parameters I_{D1}/I_G and $G_{(FWHM)}$ (Fig. 35), nor between the parameters $I_{D1}/(I_{D1} + I_G)$ *(%)* and $G_{(FWHM)}$ (Fig. 36). However, the parameters $I_{D1}/(I_{D1} + I_G)$ *(%)* and I_{D1}/I_G, have a significant correlation (Fig. 34). Regardless of correlation, Figs 34, 35, and 36, show that the samples from Locality 1 have experienced a greater thermal maturity than those from Locality 2.

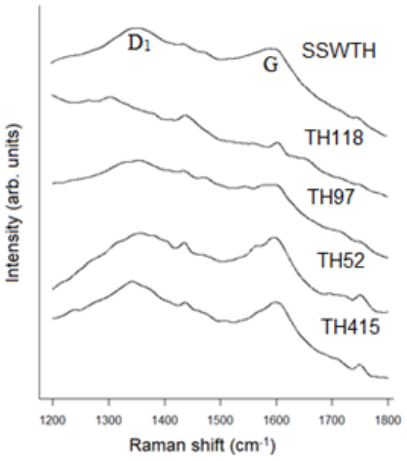

Figure 33. Raman spectra from 1200-1800 cm^{-1} for Locality 2 samples, TH415, TH52, TH97, TH118, and SSWTH.

Table 1. Raman spectral data for samples from Localities 1 and 2, showing the number of spots that were analysed, and the total number of spectra generated for each sample. A representative spectrum from each thin section was deconvoluted to yield the values for the G band width (FWHM), (I_{D1}/I_G), and $I_{D1}/(I_{D1} + I_G)$.

Sample	Locality	Number of Spots	Number of Spectra	$G_{(FWHM)}$	I_{D1}/I_G	$I_{D1}/(I_{D1} + I_G)$
WP0	1	2	2	45.2	1.99	*0.67*
WP1	1	3	3	57.25	1.61	0.62
WP2	1	3	4	42.09	1.65	0.62
MM	1	2	2	46.18	1.59	0.61
WAR/405	1	2	2	45.41	1.48	0.60
TH415	2	3	5	68.35	1.57	0.61
TH52	2	3	4	115.49	1.63	0.62
TH97	2	2	3	86.77	1.21	0.55
TH118	2	3	3	138.88	0.87	0.47
SSWTH	2	3	3	68.5	1.01	0.50

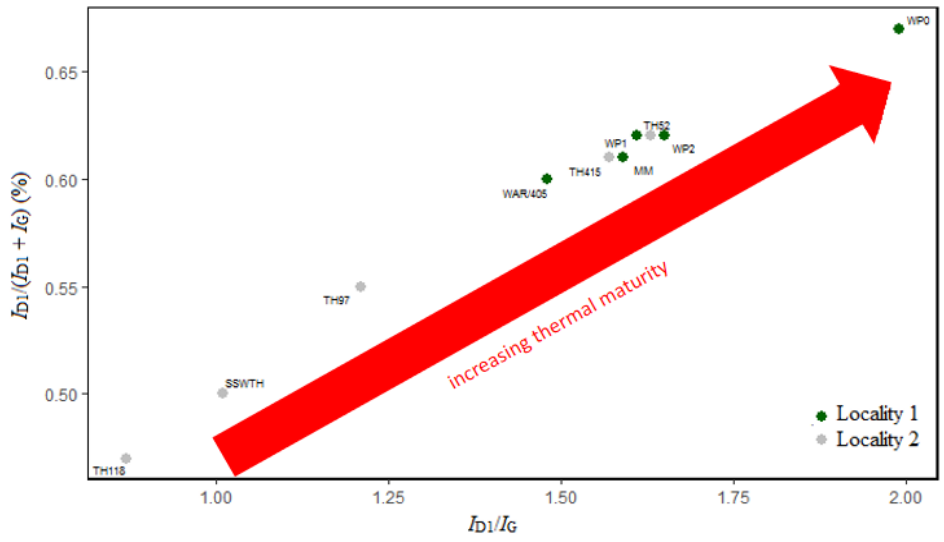

Figure 34. Cross plot showing the relationship between $I_{D1}/(I_{D1} + I_G)$ (%) and I_{D1}/I_G for all samples from Table 1. The Spearman's rank correlation of $I_{D1}/(I_{D1} + I_G)$ (%) and I_{D1}/I_G is -0.975, and the p-value was significant (0.0048).

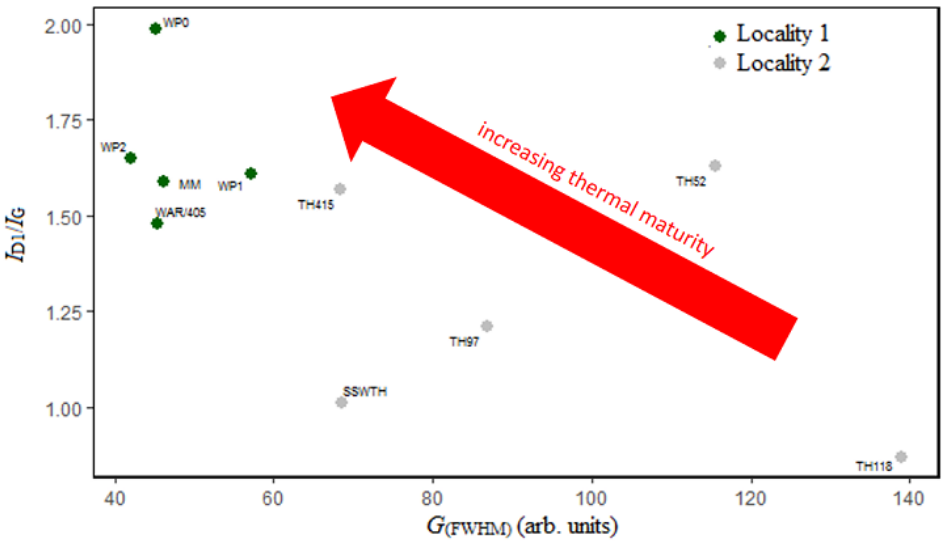

Figure 35. Cross plot showing the relationship between I_{D1}/I_G and $G_{(FWHM)}$ for all samples from Table 1. The Spearman's rank correlation of I_{D1}/I_G and $G_{(FWHM)}$ is -0.5, and the p-value was not significant (0.45).

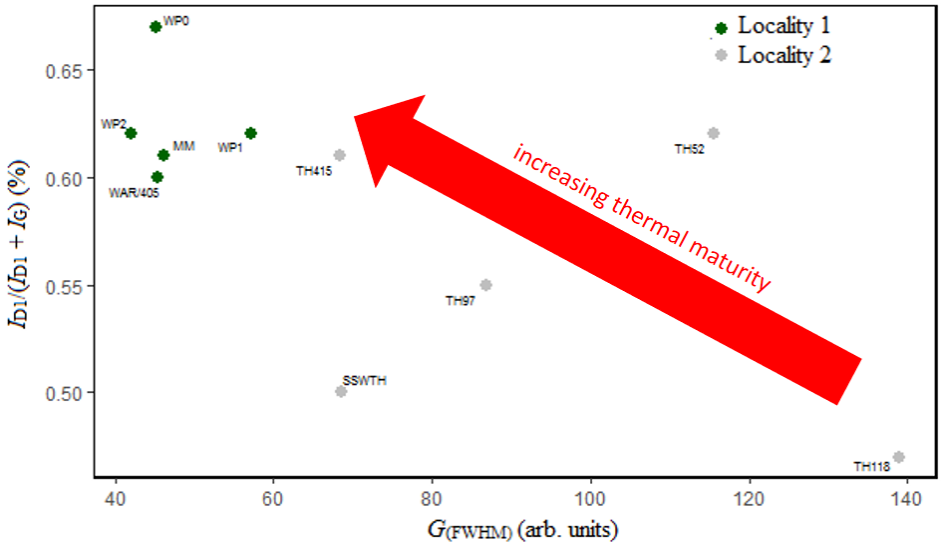

Figure 36. Cross plot showing the relationship between $I_{D1}/(I_{D1} + I_G)$ (%) and $G_{(FWHM)}$ for all samples from Table 1. The Spearman's rank correlation of $I_{D1}/(I_{D1} + I_G)$ (%) and $G_{(FWHM)}$ is -0.308, and the p-value was not significant (0.614).

4.4 Micro-XRF results

4.4.1 Locality 1. WAR Section, northern Bunkers Range

WP1

The section of WP1 that was element mapped is shown in Figs 37 and 38A. Al, Ca, Fe, K, Mg, Mn, P, Pd, Rh, S, Si, Sr, Ti, and Zn were detected in this sample (Fig. S3), but there are significant differences in the elemental composition throughout the sample. WP1 has Ca widely distributed through the sample (Fig. 38B & C). Mg was found in trace amounts throughout the sample, but Fe was not found in association with Ca, indicating that the primary composition of the sample is likely calcite, rather than dolomite, even though this sample is from the Woodendinna Dolostone (Petrash et al., 2016, Douglas et al.,2015). The K, Si, and Al association is inverse to Ca and is found in the matrix surrounding the stromatolite, and in non-biogenic layers (Fig. 38D). Al and Fe compositional zoning is present in rip-up clasts that surround the stromatolite, and in these zones K and Si are also present, which could indicate the presence of illite or smectite, from the clay-mica group. Illitisation of smectite can occur during diagenesis (Fig. 38D) (Liu et al., 2012). However, the clays were not decipherable petrographically because they are too fine-grained. There are traces of Mn and Ti surrounding the stromatolitic material (Fig. S3). Mg, P, S and Sr were found throughout the entire sample. However, as an artefact of the XRF lighter elements can appear consistently blotchy, so no specific zones can be

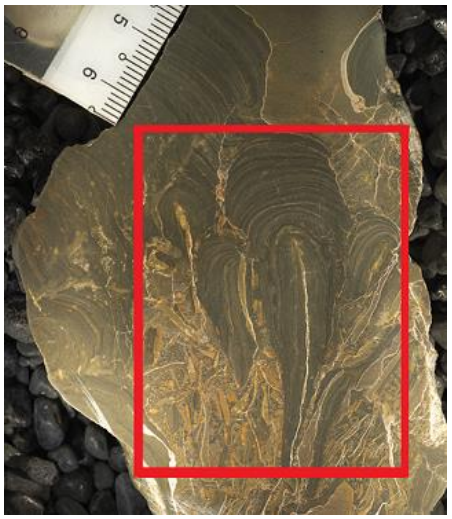

Figure 37. Hand specimen of WP1, the red box indicates the section that was element mapped with XRF.

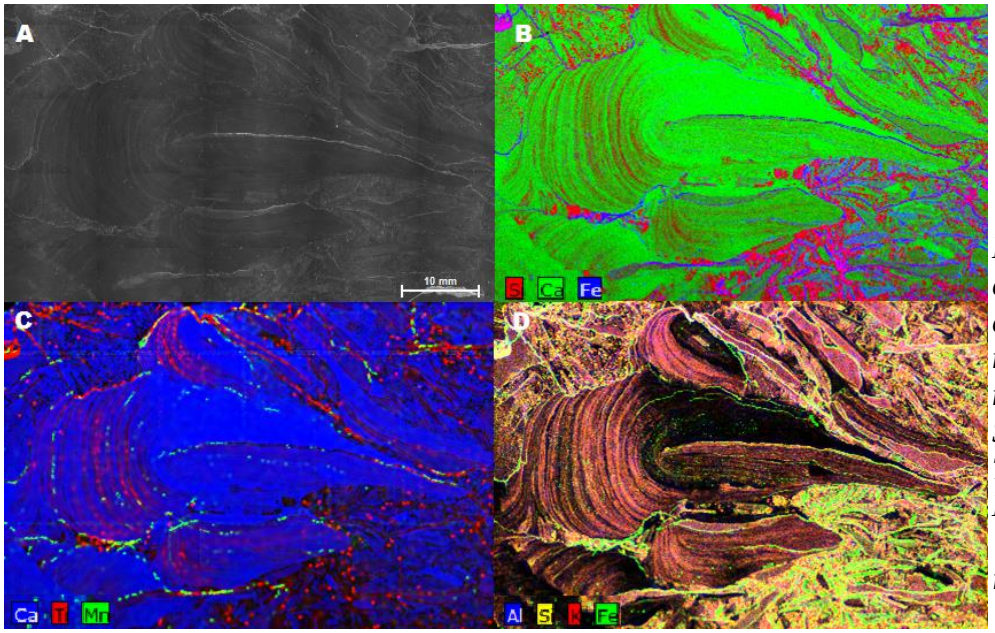

Figure 38. False colour maps of WP1 created by XRF mapping. A. microphotograph; B. Si, Ca and Fe; C. Ca, Ti, and Mn; D. Al, Si, K, and Fe. Scale bar = 10 mm for all images.

accounted for (Fig. S3). Mn, Zn, and Ti are transition metals, which can be effectively chelated by chitin, which could occur in metazoans (Delben and Muzzarelli, 1989). Siderophores (produced by cyanobacteria) are effective chelators of iron (Zürcher et al., 2006), and other metals, which could explain the distribution of some elements within the sample. Pd is an artefact of XRF.

WP2 and MM

The entire hand specimen of WP2 and MM was element mapped (Fig. 39A), and contains Al, Ca, Fe, K, Mn, Ni, Rb, S, Si, Sr, Ti and Zn (Fig. S4). The contact between WP2 and MM is enriched in Fe (Fig. 39B & D), and Si is not present in this layer, which may be due to the contact between an iron encrusted hardground, common throughout Locality 1, and the microbial mat. Within the matrix of WP2 the layers alternate between Si-rich and Ca-rich (Fig. 39B, C & D), and these alternations continue into the microbial mat layer above. Si co-occurs with K (Fig. 39C & D). Al, Sn, S and Sr are distributed throughout the entire sample, so no specific spatial inferences can be made. Ti occurs in patches throughout the sample (Fig. S4), which supports the identification of rutile which was noted in the thin section. Rb is an artefact of XRF.

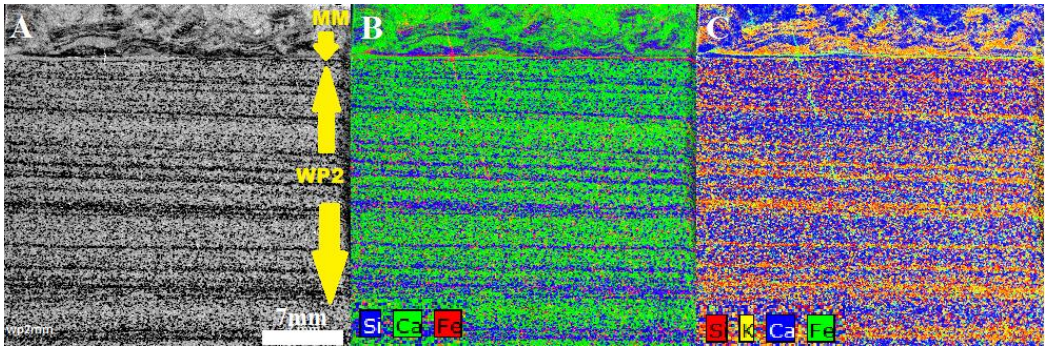

Figure 39. False colour element maps of WP2 and MM created by XRF. A. Black and white image of the WP2 and MM hand specimen, labelled to show the separate parts; B. Si, Ca and Fe; C. Si, K, Ca, and Fe. The entirety of the hand specimen was element mapped. Scale bar = 7mm in all images.

WAR/405

The section of WAR/405 that was element mapped is shown in Figs 40 and 41A. Al, Ca, Fe, K, Mn, P, S, Si, Sr, Ti and Zn were detected within this sample (Fig. S5). WAR/405 contains high amounts of Ca, and rather low abundances of Fe and Mg, so the mineral composition is calcite (Fig, 41 B, C and D). The distribution of Si, Al and K is interpreted to be due to K-feldspars which are observed in thin section (Fig. 41C). Zn appears within the cracks. There is a large Sr-filled cavity in the middle of the sample (Fig. 41B).

Figure 40. Photograph of the hand specimen of WAR/405, showing the area that was element mapped inside the red box. A. an archaeocyath.

This cavity was not seen in thin section so it has not been possible to determine the mineralogy. Si has an inverse relationship to Ca. Mn and Fe are concentrated on the middle of the archaeocyath fossils.

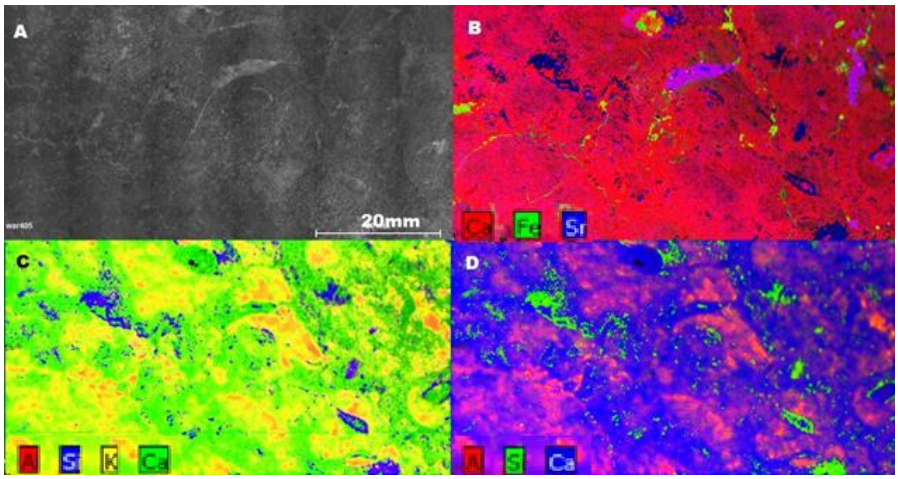

Figure 41. False colour maps of sample WAR/405 created by XRF mapping. A. photomicrograph; B. Ca, Fe, and Sr; C. Al, Si, K, and Ca; D. Al, Si, and Ca. Scale bar = 20 mm in all images.

4.4.2 Locality 2. Wirrealpa Limestone, Bunkers Range

Thrombolite Hill Samples (TH)

TH52, TH97, and TH118 (Figs. 42 & 43A) were mapped by XRF. All three TH samples contain the same elements: Ca, Al, Fe, K, Mg, Mn, P, Rb, Rh, S, Si, Sr, Ti, and Zn (Fig. S6). Areas composed of Al, Fe, K, Mg, Mn, Rb, Si, and Ti are interpreted to be due to clays, and these have an inverse relationship to Ca, P, and S, which represent carbonates (Fig. 43B). Clays were seen in thin section, but were too fine-grained for their mineralogy to be determined.

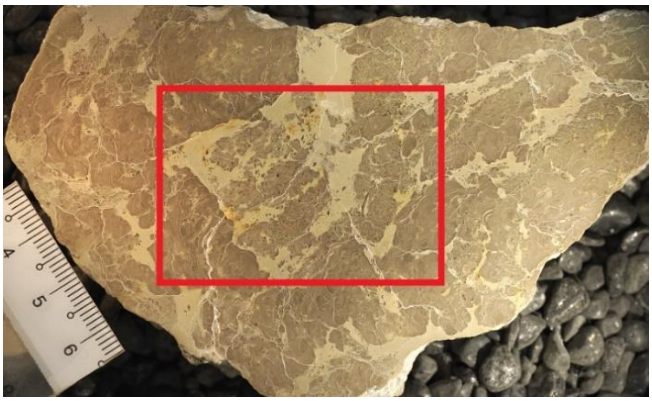

Figure 42. Photograph of the hand specimen of TH118, showing the area that was element mapped inside the red box.

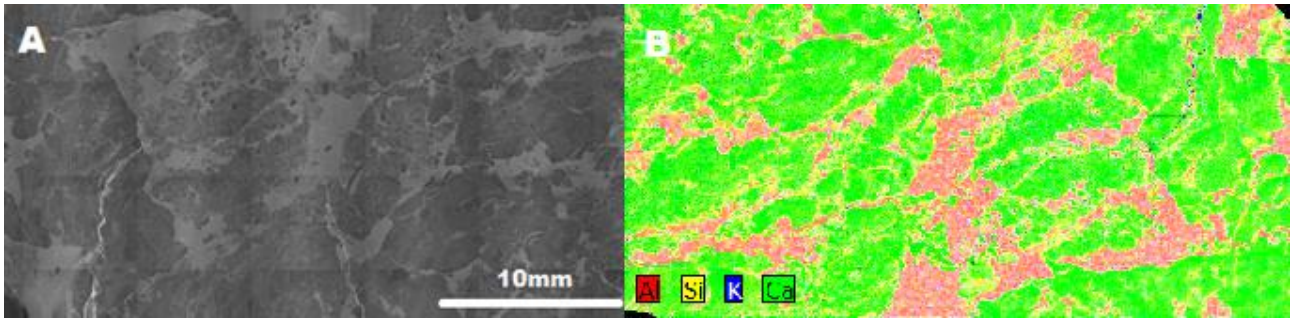

Figure 43. False colour elemental maps of TH118, created by XRF. A. photomicrograph; B. Al, Si, Ca, and K. Scale bar = 10 mm in both images.

SSWTH

The SSWTH sample was element mapped by XRF (Figs 44 and 45A) and contains Al, Ca, Cu, Fe, K, Mn, P, S, Si, Sr, Ti and Zn (Fig. S7). Of these elements, P, S, and Mg are distributed throughout the entire sample, whereas Al, Fe, K, Sr, and Si are concentrated in the concentric concretions of the oncolites (Fig. 45B, C and D). The centre of some oncolites are composed of K-feldspars partly altered to clays, as confirmed by thin section petrography. Other oncolites contain calcitic fossils at their core. Mn and Ca have an inverse relationship to Al, Fe, K, Sr and Si. Sr is also present in some thin stringers where other elements are not, except for Ca and S (which is present throughout), indicating that this mineral assemblage could be Celestine ($SrSO_4$).

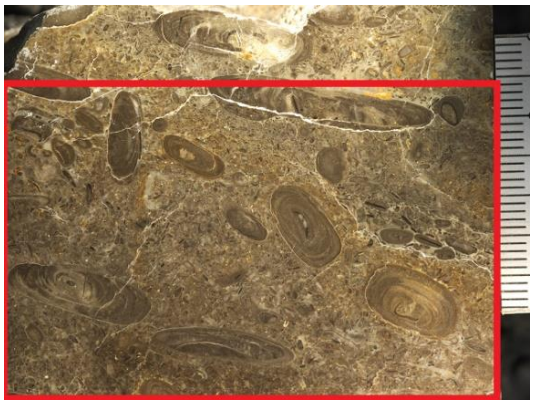

Figure 44. Photograph of the hand specimen of SSWTH, showing the area that was element mapped inside the red box.

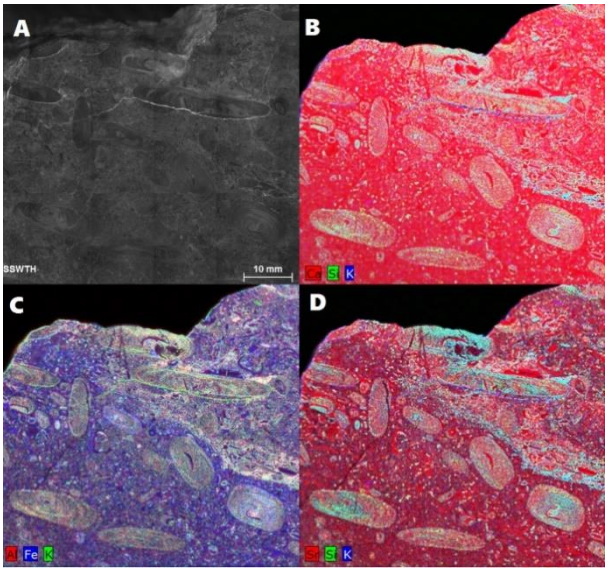

Figure 45. False colour elemental maps of SSWTH, created by XRF. A. photomicrograph; B. Ca, Si, and K. C: Al, Fe, and K; D. Sr, Si, and K. Scale bar = 10 mm in all images.

4.5 Organic Geochemistry

4.5.1 Locality 1. WAR Section, northern Bunkers Range

All samples from Locality 1 contain a series of *n*-alkanes in their bitumen I fraction. However, no aromatic hydrocarbons or other aliphatic hydrocarbons, except long-chain monomethyl alkanes, were detected. Other highly thermally mature samples (eg. French et al., 2017) have monomethyl alkanes, *n*-alkanes, and aromatic hydrocarbons, and it is unclear why the samples from this study have few aromatic and aliphatic hydrocarbons. The *n*-alkanes ranged from C_{17}-C_{34}, with unimodal and smooth distributions, and with the maxima ranging from C_{25}-C_{29} (Fig. 46). Sample WP2 was contaminated with phthalic acids which made it impossible to distinguish any *n*-alkanes in the region C_{26}-$C_{30.}$ The MM and WP2 sub-samples have slight differences in their distribution of *n*-

alkanes, which might indicate two different organic inputs between the hard ground and the microbial mat. WP0, which is the oldest sample and comes from a reddened horizon, has the least *n*-alkanes, and the amount of *n*-alkanes increases as the age of the sample decreases and the distance from the reddened horizon increases, with WAR/405 containing the most *n*-alkanes. This finding supports the Raman data, which show that WP0 is the most thermally mature of the Locality 1 samples, and WAR/405 is the least thermally mature.

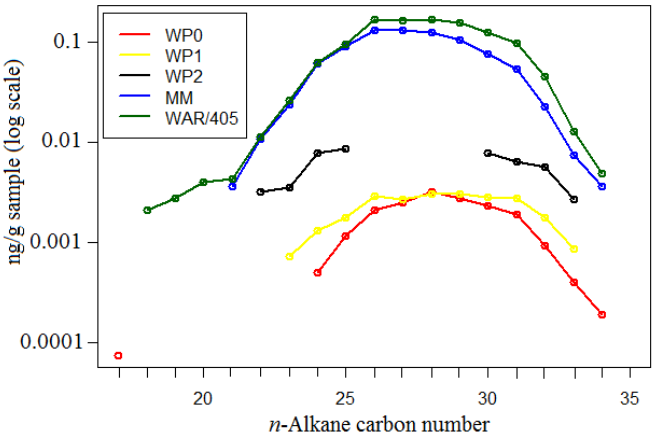

Figure 46. Amount (ng/g sample) and distribution of n-alkanes in the samples from Locality 1 for bitumen I. Procedural blanks yielded no n-alkanes.

Bitumen II extraction was performed on sample MM from Locality 1, hereafter called MMBi2. MMBi2 contains a range of *n*-alkanes from C_{21}-C_{34}, which are present in lower abundances than in bitumen I, except for C_{33} and C_{34} which are present in equal amounts (Fig. 47). The *n*-alkanes range from C_{21}-C_{34}, with a unimodal and primarily smooth distribution (Fig. 47). The maxima for bitumen II is $C_{28,}$ compared to C_{27} for bitumen I (Figs S8 and S9).

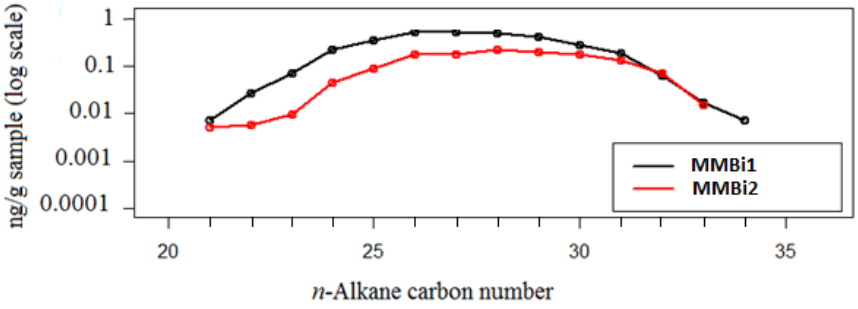

Figure 47. Amount (ng/g sample) and distribution of n-alkanes in the sample MM from Locality 1 for bitumen I and bitumen II.

In both bitumen I or II there is either a lack of any odd or even-carbon number n-alkane predominance, as shown by the carbon preference index (CPI) values of ~1.0, or a very slight even carbon number n-alkane predominance (CPI = 0.90–0.96) (Table 2). These data are suggestive but not confirmative of thermally mature samples, but are also consistent with carbonate/hypersaline environments that are characterised by an even carbon number n-alkane predominance (Peters et al., 2005).

Table 2. Carbon Preference Indexes for WP0, WP1, MMBi1, MMBi2 and WAR/405. WP2 was excluded due to no n-alkanes being detected between C_{26} and C_{29}.

Ratios	WP0	WP1	MMBi1	MMBi2	WAR/405
CPI (22-32)	0.97	1.01	0.98	0.95	0.98
CPI (26-32)	1.02	1.04	1.04	1.00	1.05

CPI 2 (26-28)	0.96	0.90	1.02	0.93	0.98

Monomethylalkanes were detected in WP0, MM and WAR/405 (Fig. 48). 2- and 3-methyl alkanes are considered ambiguous biomarkers because they do not have biological specificity and may be formed by inorganic processes (Peters et al., 2005). Monomethyl branched alkanes are mainly derived from bacterial input, such as sulphate reducing bacteria which produce both 2-methyl and 3-methyl fatty acids, which can be transformed into 2-methyl and 3-methyl monomethylalkanes (Peckmann et al., 2004). Mid-chain branched monomethylalkanes are typically attributed to cyanobacteria as these are the only microorganisms known to biosynthesise these alkanes (Shiea et al., 1990). Modern microbial mats are dominated by short-chain monomethyl and dimethyl alkanes (Brocks et al., 2003), although Kenig et al., (1990) found that the composition of monomethylalkanes from microbial mats changes with depth. Long-chain even monomethylalkanes from C_{24} to C_{34} have been found in both transgressive and regressive mats (Kenig et al., 1990; Kenig et al., 1995) in Precambrian carbonate rocks (Klomp, 1986; Fowler and Douglas, 1987; Hoshino et al., 2012; Hoshino and George, 2015). However, long-chained MMAs are also frequently encountered in the surface lipids and waxes of arthropods (Kenig et al., 1995; Stökl et al., 2014; Moore et al., 2016; Soares et al., 2017), as they are cuticular hydrocarbons. Even within extant species, intra-species variation is under-researched (Menzel et al., 2017). It is unclear whether these monomethyl alkanes could have some from a specific source such as an arthropod, a bacterial source, or maybe simply reflect the high thermal maturity of these samples.

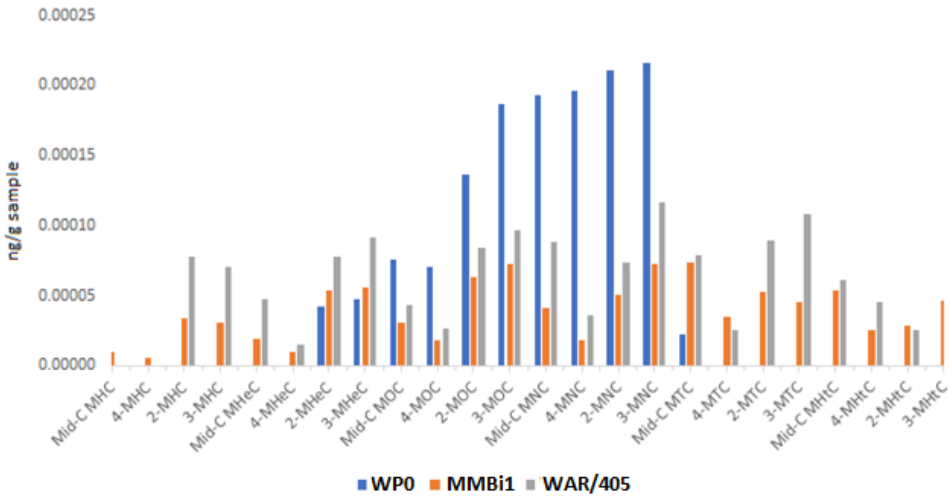

Figure 48. Histograms of monomethyl alkane abundances (ng/g sample) for the Locality 1 samples WP0, MM, and WAR/405. Mid-C = midchain; MHC =methylhexacosane; MHeC=methylheptacosane; MOC = methyloctacosane; MNC = methylnonacosane; MTC = methyltriacontane; MHtC =methylhentriacontane.

The samples from Locality 1 contain monomethyl alkanes from C_{26}-C_{31}, with the 3-methyl isomers usually being the largest non-coeluting peaks (Fig. 48). WP0 has a short range of long-chain monomethyl alkanes from C_{27} to C_{29}, whereas MM and WAR/405 contains long-chain monomethyl alkanes from C_{26} to C_{30} (Fig. 48). Where WAR/405 has monomethylalkanes it generally has them in higher abundance than WPO and MMBi1 (Fig. 48; Table 3). The monomethyl alkanes in MMBi2

(Fig. S10) are largely the same as for MMBi1 (Fig. S11) but are in lower abundance. However mid-chain methylhexacosane and 4-methylhexacosane were not detected (Fig. 49).

Table 3. Monomethylalkane ratios for the Locality 1 samples.

Ratios	WP0	MMBi1	MMBi2	WAR/405
4-methylhentriacontane/2-methylhentriacontane	0.28	0.90	0.51	1.81
3-methylheptacosane/2-methylheptacosane	1.12	1.03	0.47	1.17
3-methylnonacosane/2-methylnonacosane	1.02	1.44	1.49	1.57
3-methylhentriacontane/2-methylhentriacontane	1.23	1.61	1.83	2.99

4.5.2 Locality 2. Wirrealpa Limestone, Bunkers Range

Three samples from Locality 2 contain a series of *n*-alkanes, in the bitumen I. As for Locality 1, no other aliphatic or aromatic hydrocarbons, except long-chain monomethyl alkanes and isoprenoids were detected. Sample TH52 contains *n*-alkanes ranging from C_{20}-C_{35} and TH82 contains *n*-alkanes ranging from C_{20}-C_{36} (Fig. 50). TH415 contains *n*-alkanes ranging from C_{14}-C_{35}, and a predominance of long-chain *n*-alkanes >C_{20}, and also contains the acyclic isoprenoids pristane and phytane (Fig. 50). All three samples have unimodal and smooth *n*-alkane distributions, with the maxima ranging from C_{25}-C_{29} (Fig. 50). Whilst the C_{27}, C_{29} and C_{31} *n*-alkanes originate mainly from higher plant epicuticular waxes,

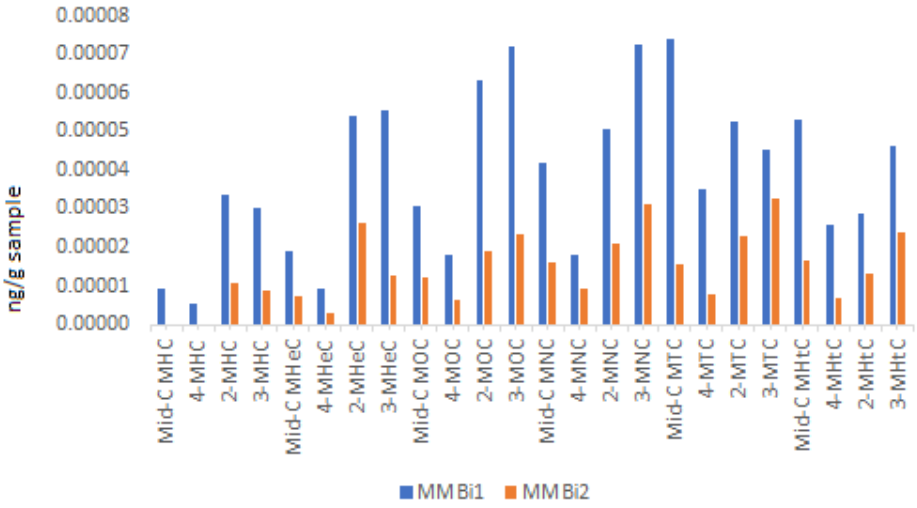

Figure 49. Histograms of monomethyl alkane abundances (ng/g sample) for the Locality 1 sample MMBi1 and MMBi2. Mid-C = midchain; MHC =methylhexacosane; MHeC=methylheptacosane; MOC = methyloctacosane; MNC = methylnonacosane; MTC = methyltriacontane; MHtC =methylhentriacontane.

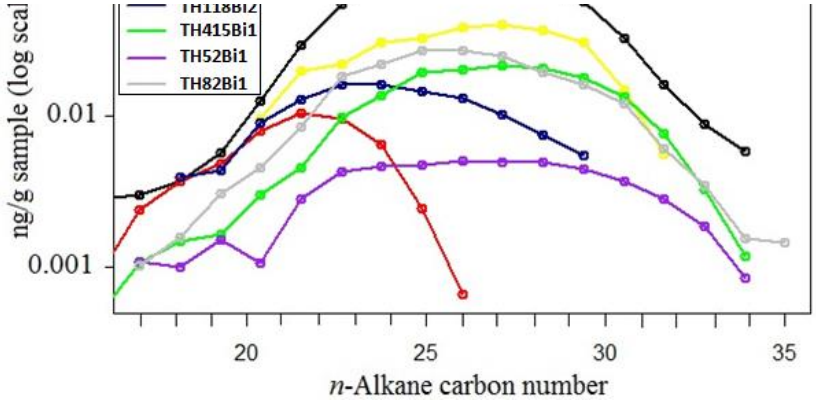

Figure 50. Amount (ng/g sample) and distribution of n-alkanes in the samples from Locality 2 for Bitumen I and Bitumen II. Procedural blanks yielded no n-alkanes.

certain algae can also contain higher molecular weight *n*-alkanes, which may explain their source as higher plants had not yet evolved.

The bitumen II of SSWTH contains a series of siloxanes that obscure the *n*-alkanes, and TH52 was destroyed before the bitumen II extraction process could be completed. However, the rest of the samples that underwent the bitumen II extraction process produced a series of *n*-alkanes. All samples that underwent bitumen II processing will hereafter be referred to as the Bi1 or Bi2 fractions. The bitumen II sample of TH415 (TH415Bi2) has the same distribution of *n*-alkanes from C_{14} to C_{35} as the bitumen I extract, but in much higher abundance. The bitumen I also contained pristane and phytane (Fig. S12) with a Pr/Ph ratio of 1, which is consistent with a somewhat reducing environment. The bitumen II sample TH97Bi2 has unimodal and mostly smooth distributions of *n*-alkanes, but TH82Bi2 and TH118Bi2 have shorter ranges (C_{19}-C_{28} and C_{21}-C_{31} respectively) (Fig. 50). TH82Bi2 has maxima at C_{24}, and *n*-alkanes drop off rapidly at higher molecular weights.

Pristane and phytane are molecules which come from chlorophyll (Rontani and Volkman, 2003) and are used to infer information about the depositional environments. Reducing conditions are commonly inferred based on Pr/Ph ratios that are <1.0. TH415 Bi1 has a Pr/Ph ratio of 0.94 and TH415 Bi2 a Pr/Ph ratio of 1 (Table 4; Fig. S12). There is a general lack of any odd or even-carbon number n-alkane predominance, as shown by the CPI values that are ~1.0 (Table 4). An exception is sample TH82Bi2 which has a CPI (26-32) of 0.62 and CPI 2 of 0.69 indicates an even-over-odd predominance (Table 4). As with Locality 1, CPIs of ~1.0 are consistent with other data, suggesting that the samples are thermally mature (Peters et al., 2005; Olivares et al., 2013). The ratios Pr/n-C_{17} and Ph/n-C_{17} are sometimes used in petroleum correlation studies. If the Pr/n-C_{17} ratio is <0.5 it indicates open water conditions. However, these ratios decrease with thermal maturity, so are unreliable source indicators. This is because increasing thermal maturity causes *n*-alkanes to be generated faster, in contrast to highly biodegraded samples in which isoprenoidal hydrocarbons are more likely than *n*-alkanes to remain (Nwadinigwe and Alumona, 2017). Therefore, the low Pr/n-C_{17} ratio for sample TH415 (0.34) means a high level of maturity, supporting the interpretation of a high thermal maturity for these samples (Nwadinigwe and Alumona, 2017).

Table 4. Carbon Preference Indices and pristane/phytane ratio for Locality 2 samples.

Ratios	TH415Bi1	TH415Bi2	TH52Bi1	TH82Bi1	TH82Bi2	TH97Bi2	TH118Bi2
Pr/Ph	0.94	1.0	nd	nd	nd	nd	nd
CPI (22-32)	0.98	1.01	1.05	0.96	1.01	1.02	1.07
CPI (26-32)	1.03	1.04	1.05	1.00	0.62	1.06	1.05
CPI 2 (28-30)	1.05	1.05	1.06	0.95	0.69	0.95	0.99

nd =not determined.

Only two samples from Locality 2 yielded monomethyl alkanes (TH415 and TH82; Fig. 51). TH415 contains monomethyl alkanes from C_{26}-C_{31} and TH82 contains monomethyl alkanes from C_{26}-C_{30}. Although TH82 and TH415 contain comparable quantities of *n*-alkanes (Fig. 48), where MMAs are present TH82 generally has higher abundances of MMAs than TH415 (Table 5; Fig. 49). TH82 did not contain mid-chain methylheptacosanes, 4-metheylheptacosane, mid-chain methyloctacosanes, 4-methyloctacosane, 2-methyltriacontane, or 2-methyltriaconane, although it contains monomethyl alkanes both with shorter and longer chains than these. There is a larger abundance of monomethyl alkanes in the bitumen II of TH415 than in its bitumen I. However, sample TH82 yielded fewer and a much shorter distribution of monomethyl alkanes (Fig. 51). There has also been little research into the organic geochemistry of trilobites, which are also arthropods and found in abundance in samples (eg Fig. 22). So as in Locality 1, it is unclear whether these monomethyl alkanes could have come from specific arthropod sources, bacterial sources, or are an artefact of high thermal maturity.

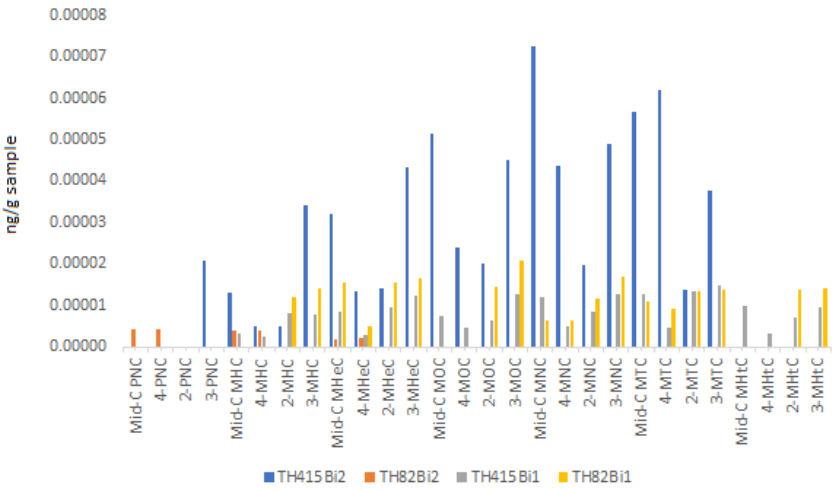

Figure 51. Histograms of monomethyl alkane abundances (ng/g sample) for the Locality 2 samples TH415 and TH82 in both bitumen I and II. Mid-C = midchain; PNC=pentacosane; MHC =methylhexacosane; MHeC=methylheptacosane; MOC = methyloctacosane; MNC = methylnonacosane; MTC = methyltriacontane; MHtC = methylhentriacontane.

Table 5. Monomethylalkane ratios for bitumen I, Locality 2 samples.

Ratios	TH415	TH82
3-methylnonacosane/n-triacontane (n-C_{30})	0.07	0.11
3-methylhexacosane/2-methylhexacosane	0.95	1.19
mid-chain methylhexacosanes/(3-methylhexacosane + 2-methylhexacosane)	0.20	nd
mid-chain methyloctacosanes/(3methyloctacosane + 2-methyloctacosane)	0.38	nd

nd = not determined.

The lack of aromatic hydrocarbons in the bitumen I of most of the samples, combined with the lack of high molecular weight *n*-alkanes with an odd carbon number predominance (which could indicate plant lipids if they were present), make it likely the *n*-alkanes and monomethyl alkanes are a syngenetic signal. This is supported by the several blanks which were performed, including those on the rock crusher, the glassware (Fig. S13), and on the rotary evaporator, which yielded no *n*-alkanes, only siloxanes and phthalates.

However, two samples from Locality 2 have a bitumen II extract that contains aromatic hydrocarbons, including phenanthrene and methylphenanthrenes, (Fig. S14), which were absent from the bitumen I of these samples. These hydrocarbons are often used to calculate maturity parameters, because the distribution of methylphenanthrenes changes with increasing degree of thermal alteration (Radke et al., 1982). Sample SSWTH has a methylphenanthrene index (MPI) of 0.44, and TH415 has an MPI of 0.10. As in the case of George et al. (1998), phenanthrene is more than 5 times more abundant than the methylphenanthrene isomers (6-9x for SSWTH; >40x for TH415), so it is likely that both MPIs indicate samples that are highly thermally mature with demethylation the dominant process. Thus, it is more appropriate to use the calculated reflectance calibration (Rc = (-0.6 × MPI) + 2.3), which shows that both TH415 (2.24) and SSWTH (2.04) are very thermally mature (Radke et al., 1982). This finding is consistent with the Raman data obtained (Table 1). Wang et al. (2005) developed the following equation for deriving maximum palaeotemperatures $MaxT = \frac{In\%Rc+1.78}{0.0124}$ which are 209°C for TH415 and 201°C for SSWTH.

5. Discussion

5.1 Depositional environments

5.1.1 Locality 1. WAR Section, northern Bunkers Range

The base of the WAR section is the contact between siliclastic sandstones of the Parachilna Formation and the lowermost shallow marine carbonates of the Woodendinna Dolostone. Sample WP0, collected from near the contact between the two formations, is a peloidal grainstone, representing a current- or wave-influenced shallow marine, inner shelf to lagoonal peritidal platform (Flügel, 2004). WP0 came from a high energy environment, as shown by well-sorted, equally-sized grains (Fig. 10), and may have undergone periods of subaerial exposure as shown by the secondary veins of carbonate, which may represent desiccation cracks (Fig. 10C). This is consistent with Haslett's (1975) interpretation of the Woodenedinna Dolostone (and overlying Wirrapowie Limestone) as representing high intertidal and supratidal mudflats with periods of subaerial exposure.

Sample WP1 consists of a basal flat pebble conglomerate overgrown by relatively small columnar stromatolites. There is controversy over the origin of flat pebble conglomerates because they come from highly varied depositional environments and lack common modern analogues (Myrow et al., 2004). These conglomerates are usually found with an absence of deep-burrowing organisms and have previously been found with microbial communities overgrowing them (Myrow et al., 2004). Peritidal carbonate cycles consisting of flat pebble conglomerates with microbialites growing over them, along with evidence of desiccation are commonly interpreted to be

transgressive lags (James, 1984 and references therein). Modern day columnar stromatolite analogues from Hamelin Pool, in Shark Bay, Western Australia grow in a subtidal environment (Fig. 51), which is periodically affected by storm activity, and these living stromatolites have been partially accreted during variable sea-level conditions, with the growth of the columnar stromatolite representing periods of slightly deeper water punctuated by shallowing and desiccation (Jahnert and Collins, 2012). This is further supported by petrographic changes in lamination (Fig. 12), between smooth and pustular/clotted fabrics which are comparable to the modern day forms where high energy water near these domains supplies microbial communities with fine carbonate particles (Jahnert and Collins, 2012).

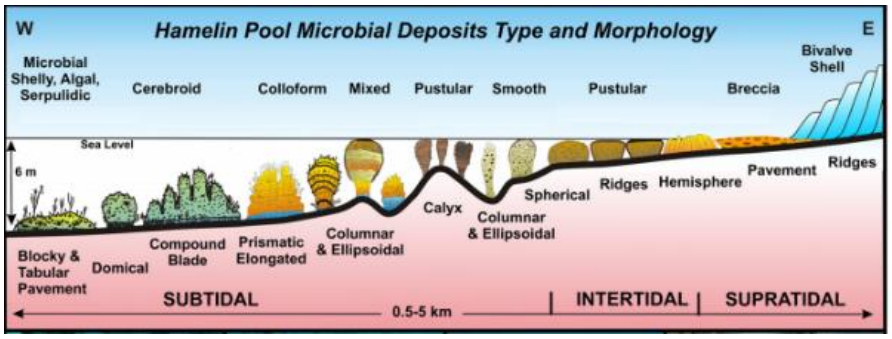

Figure 51. Model of deposition for the microbial deposits in Hamelin Pool showing the varying morphologies present (Jahnert and Collins, 2012). The columnar stromatolites in the subtidal zones display similar morphology to those growing in WP1.

The Vendian-Cambrian interval on the Siberian platform likewise has flat-pebble conglomerates at the base of thick carbonate and evaporite sequences, with peloidal grainstones and columnar stromatolites (Kuznetsov and Suchy, 1992). It is likely that these two samples (WP0 and WP1) represent a relatively shallow, supratidal to sabkha evaporative basin.

The environment transitioned between WP2 and MM, where the presence of an iron encrusted hardground represents a change that caused sediments to lithify as they form. The firmground surfaces suggest slow sedimentation rates and restricted lagoonal environments (Betts et al., 2016). A regular and even sedimentation rate was noted in WP2 (Figs 14 and 15). Changes in seawater chemistry can include enriched Fe which is seen at the contact between the firmground and the microbial mat (Christ et al., 2015; Douglas et al., 2015). The transition could also be microbially induced. However, microbial controls on syn-depositional lithification are poorly understood, and stromatolites are biased towards formation in carbonate environments and show Fe enrichment in associated sediments (Grotzinger and Knoll, 1999; Christ et al., 2015). Often marine cement precipitation below the sediment water interface is composed of low-Mg calcite as seen here (Christ et al., 2015). However, the geochemical results are inconsistent with regard to the dolostone in samples WP0, WP2 and MM. Whilst thin section observations revealed what looked like dolomite crystals, and FTIR (Fig. 29) and Raman (Fig. 30) produced some dolomite peaks, XRF only found traces of Mg. Thus, any dolomitisation is likely minor or in preliminary stages. All geochemical results are consistent with main the carbonate type being calcite. The absence of

metazoans in these samples is consistent with the slight even number carbon predominance of *n*-alkanes from GC-MS which indicate that the environments were hypersaline.

Sample WAR/405 is from the Wirrapowie Formation. The archaeocyath framestone is primarily composed of fragmentary, overturned and largely transported archaeocyaths. Some types of archaeocyath are rarely preserved in their growth position, cups are often toppled and incorporated into the framestone by providing hard substrates for bacterial growth, which means that energy levels must have been moderate (Figs 16 and 17) (Kruse, 1991). The only frame-building organisms from the Cambrian were cyanobacteria and archaeocyaths (Kruse, 1991). The abundance of archaeocyaths means the environment was relatively well oxygenated at the sediment-water interface (Haslett, 1975). There is no crossbedding, or coarse detrital material in this sample which indicates a primarily low energy environment. Thus Daily's (1972) interpretation of a shallow shelf under stable marine conditions is supported here.

5.1.2 Locality 2. Wirrealpa Limestone, Bunkers Range

The thrombolites present in the Wirrealpa Limestone are coarse agglutinated thrombolites, very similar inform to those seen at Hamelin Shark Bay (Riding, 2011). Originally thrombolites were thought to form through metazoan disruption of laminated bacterially communities, but formation of these coarse grained thrombolitic structures is now thought to be a culmination of mat community, water movement and turbid waters (Riding, 2011). The Shark Bay thrombolites are thought to have formed subtidally before being subject to sea level fall. This is consistent with the low Pr/Ph ratios derived from sample TH415 which are inferred to represent a somewhat reducing environment. Braga et al., (1995) described the same depositional environment for Miocene thrombolites from South East Spain, where strong water turbulence supplied irregular and uneven sediment resulting in patchy encrustation of domes by skeletal benthos. This description and the internal microstructure is similar to that of the Cambrian thrombolites described in this study (Fig. 52).

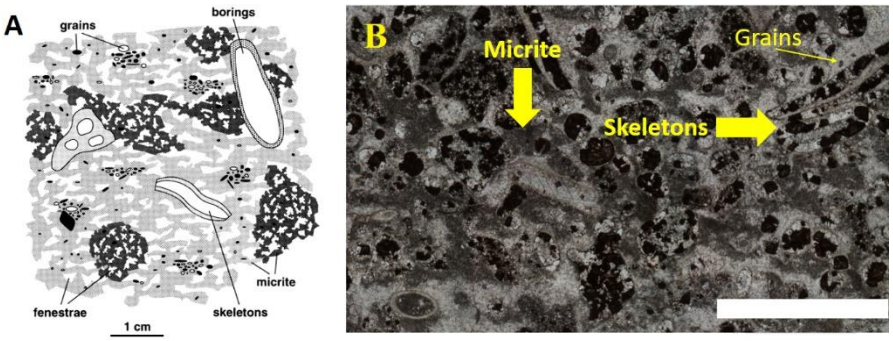

Figure 52. Comparison of the internal structure of two different aged thrombolitic structures. A: Characteristic shelf margin thrombolite fabric produced by irregular areas variously dominated by different structure, Miocene from Braga et al., (1995). B: Internal structure of TH118 from this study, Cambrian. Scale bar in B is 2mm.

Modern stromatolites typically have a microscopic and peloidal form to their clots, whilst ancient thrombolites have macroscopic clots with varied shapes (Soudry and Weissbrod, 1995). In Miocene microbialites that underwent continual transgressions and evaporative conditions, sedimentation of interbedded claystones occurred with microbialites (Peryt et al., 2004). The clays (Fig. 19B) seen in the thrombolites from this study have a similar morphology to the clots that Barlow et al., (2016) found and described as a 'lighter, beige-coloured supporting framework' (p. 328) in the Palaeoproterozoic Turee Group of Western Australia. Barlow et al. (2016) interpreted the contrasting texture of the clays to the clots as indicative of marine cements overgrowing biological carbonates in a low-energy, subtidal environment with high levels of $CaCO_3$, based on analogous thrombolites where structures are preserved by microbially driven precipitation and sedimentation (eg. Kennard and James, 1986; Jahnert and Collins, 2012).

Riding (2011) proposed that typically strong wave currents would help raise sand to the mat surface, which would be further supported by seasonal hypersalinity. Braga et al., (1995) found that steady accretion resulted in stromatolitic microfabrics, whereas uneven accretion resulted in thrombolites. Five factors primarily control thrombolite production: 1) patchy sediment supply, 2) highly varied grain size in sediment, 3) uneven microbial colonisation, 4) irregular dispersal of skeletal encrusters, and 5) damage to the biotic construction by macroborers and encrusters (Baga et al., 1995). Four of these five factors are seen in the thrombolites from this study 1) sedimentology between different heights of the thrombolites is radically different, 2) matrices from different stratigraphic levels have differentially sorted fragments and bioclasts, 3) microbial colonisation is present as spar arrays growing around bacterial cells, and microbial rinds surround some fossil fragments, and 4) the distribution of skeletal encrusters differs with depth and are variously dispersed. Furthermore, fragmented fossils are found throughout this locality, further supporting wave currents being a primary sedimentation control.

Whilst thrombolites themselves are common in the Cambrian, particularly the upper Cambrian (Furongian), these thrombolitic structures represent the oldest coarse grained agglutinated thrombolites heretofore described (Kennard and James, 1986; Riding, 1991). Further similarities between the thrombolites described here and those in Hamelin Pool at Shark Bay are that these thrombolites possess domical morphologies which resemble stromatolites (Fig. 53) but are without lamination (Riding, 1991).

Figure 53. Field photograph of the multi-metre thrombolites. Scale bar is 2.0 m.

The oncolitic grainstone (SSWTH) has an alochem assemblage indicative of an open marine environment. Youngs (1977) interpreted this locality to have undergone north-south transgression and regression events (Fig. 54), which is supported by the rose diagram depicting palaeocurrents based on major-axis orientation of oncolites (Fig. 25). Fragmented fossils, and oncolites indicate a previously high energy environment which transitioned into a calmer, deeper environment, allowing microbial rinds to grow around the fossils (Fig. 23aA). Furthermore, XRF analysis show the carbonate phase in the oncolites themselves (Fig. 45) is likely celestine ($SrSO_4$), which forms when biogenic calcite transforms to low-Sr calcite, and is generally associated with coastal marine carbonate-evaporite sequences (Hanor, 2004). Thus, it is likely that the oncolites formed in a high energy evaporite sequence, and then were redeposited at the height of a marine transgression (Fig. 54B).

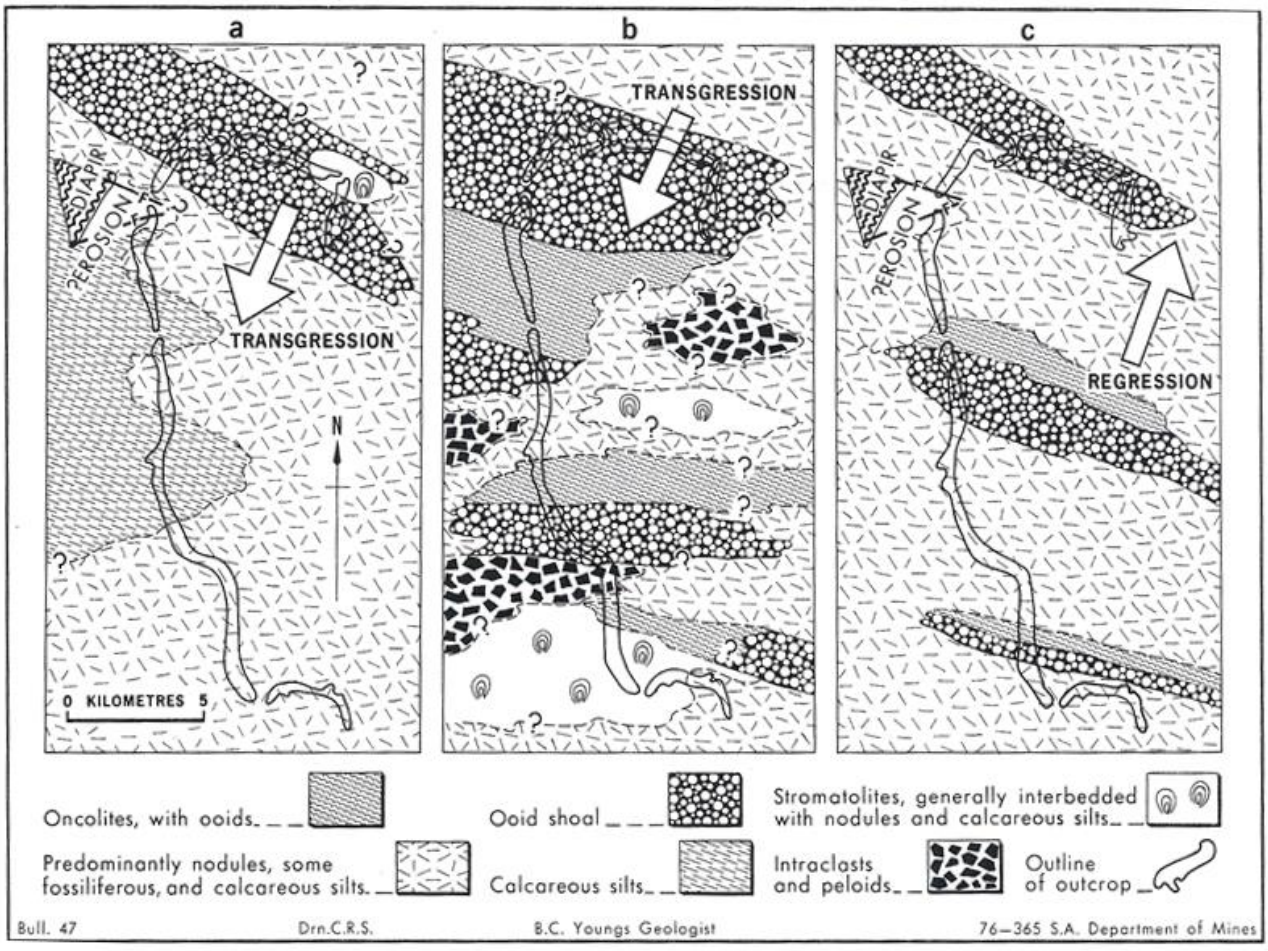

Figure 54. Palaeogeographic reconstructions for three periods during deposition in the Wirrealpa Limestone: (a) Represents the thrombolitic samples from Locality 1 and (b) represents the height of the marine transgression when SSWTH was deposited (Youngs, 1977).

5.2 Thermal maturity and diagenesis

5.2.1 Locality 1. WAR Section, northern Bunkers Range

The samples from the Woodendinna Dolostone and the Wirrapowie Limestone (Locality 1) have a higher thermal maturity than those from the younger (Cambrian Stage 5) Wirrealpa Limestone

(Locality 2), with Raman spectroscopy $I_{D1}/(I_{D1} + I_G)$ values between 60 and 67. The samples have undergone extensive diagenetic processes, as shown by the presence of stylolites (Fig. 17C), poikiloblasts (Fig. 10B), and illitisation of smectite (Fig. 38D). Also, because the majority of modern marine carbonates are aragonite or high-Mg calcite, the occurrence of low-Mg calcite in WP1 implies that diagenesis of the laminae must have occurred (Grotzinger and Knoll, 1999). Raman data indicate that WP0 is the most thermally mature of the Locality 1 samples, followed by WP1, WP2, MM and then WAR/405 (Fig. 34). In the Woodendinna Dolostone and Wirrapowie Limestone, thermal maturity decreases in the younger stratigraphic rocks and with stratigraphic distance from the reddened horizon. This is consistent with the recovery of abundant *n*-alkanes which increase in the strata above the reddened horizon disconformity (Fig. 46). There are no short or mid-chain *n*-alkanes ($< C_{15}$) in any of the samples, a feature which has also been seen in other highly thermally mature samples (Aharonovich and George, 2016). Furthermore, the near unity CPI values of the samples from Locality 1 (Table 2), together with the lack of any biomarkers including isoprenoids and the lack of any aromatic hydrocarbons, are suggestive of highly thermally mature samples.

5.2.2 Locality 2. Wirrealpa Limestone, Bunkers Range

The samples from the Wirrealpa Limestone (Locality 2) were collected from the hinge zone of the Wirrealpa Fold (Fig. 7). The samples from Locality 2 have a lower thermal maturity than those from Locality 1, as supported by Raman data (Table 1), but are still highly thermally mature, with $I_{D1}/(I_{D1} + I_G)$ values between 47 and 62 (Table 1). These samples have spar-forming rosette arrays around microbial precipitates (Figs 20A and 22A), and marine cement clays overgrowing thrombolitic clots. The oncolitic sample from SSWTH has some oncolites composed of K-feldspars partly altered to clays, and the oncolites are made of celestine which occurs as biogenic calcite transforms to low-Sr calcite. As for Locality 1, CPIs of ~1.0 suggest that the samples are thermally mature. This is further supported by a low Pr/n-C_{17} ratio for sample TH415 (0.34), and maximum palaeotemperatures of 209°C and 201°C for TH415 and SSWTH respectively, based on their distribution of phenanthrene and methylphenanthrenes. SSWTH was shown by Raman data to be the second least thermally mature sample from either Locality (Table 1, Figs, 34, 35 and 36), which is consistent with it having a lower maximum palaeotemperature than TH415. If 201°C is the lowest palaeotemperature, this is indicative of over-mature samples, in the zeolite facies, and dependent on pressure, perhaps approaching the lower greenschist facies metamorphic grade.

5.2.3 Thermal maturity of the Bunkers Range in context

Allwood et al. (2006) interpreted two members from the 3.4 Ga Strelley Pool Chert (M3, M4) and the underlying strata (Fig. 55) to have been formed in a hydrothermal environment, and a marine

environment for the M2 member which contained stromatolites. The samples from Locality 1 all have higher $I_{D1}/(I_{D1} + I_G)$ values than any from the Strelley Pool Chert. Samples TH415, and TH52 are more highly mature than any Strelley Pool Chert sample, and samples TH118 and SSWTH have $I_{D1}/(I_{D1} + I_G)$ values comparable to the marine environment from M2. No absolute temperatures have been published for the Strelley Pool Chert, but Raman spectra are comparable with other spectra taken from chlorite up to biotite grade metamorphic rocks, with peak temperatures from ~300°-400°C (Allwood et al., 2006; Marshall et al., 2007). Allwood et al., (2006) concluded that based on stratigraphic, palaeoenvironmental, and Raman data, M2 would have reached maximum burial temperatures of 200°C . The Raman data from this study (Fig. 55) indicates that TH415 and SSWTH are of comparable values to M2, which is supported by the max palaeotemperature calculations from the methylphenanthrenes.

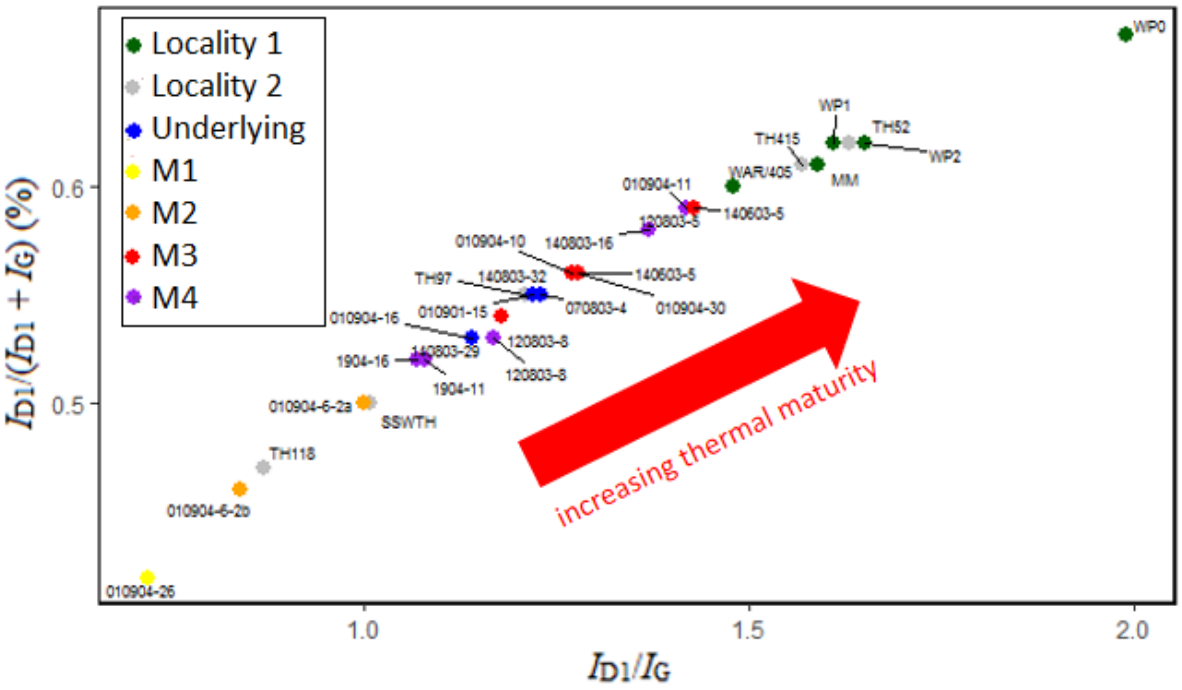

Figure 55. Cross plot showing the relationship between $I_{D1}/(I_{D1} + I_G)$ (%) and I_{D1}/I_G for samples from localities 1 and 2 from this study and 3.4 Ga Archaean cherts from the Pilbara described by Allwood et al. (2006) and Craig et al., (2007). Localities 1 and 2 defined from this study; Underlying = Underlying member, Strelley Pool Chert, volcaniclastic sediments and bedded black chert; M1 = Member 1, Strelley pool chert, a thin discontinuous jasper/chert boulder conglomerate layer; M2 = Member 2, Strelley Pool Chert, a layer of stromatolitic chert; M3 = Member 3, Strelley Pool Chert, bedded black chert; M4= Member 4, Strelley Pool Chert, a volcaniclastic unit.

Carr et al. (2010) conducted seismic surveys of the Arrowie Basin; the formations considered here are less than ~N 0°10' from the Parachilna seismic line (09TE-01), and E 0°30' from the Nilpena seismic line (09TE-O3) (Fig. S15). High heat flow values were recorded from the Parachilna seismic line, which were deemed attractive for geothermal energy exploration. The high heat flow in the area of the Parachilna seismic line was attributed to (1) the Ediacara fault being reactivated in the Quaternary, (2) other faults in the area, and (3) high heat-producing granites of the

Hiltaba Suite. The Nilpena seismic line crosses rocks that are being thrust by the currently active Ediacara fault (and other minor faults) to the north, which has displaced the base of the Cenozoic section ~1000 m. Whilst Carr et al., (2010) state that the general thermal maturity of the Arrowie Basin is at a sufficient level for hydrocarbon generation, they also assess the Cambrian rocks as immature to mature dependent on their location within the Arrowie Basin. The detailed study of the Woodendinna Dolostone, the Wirrapowie Limestone and the Wirrealpa Limestone in this work shows that these rocks are over-mature, and any fine-grained rocks interbedded with these units should not be considered as possible source rocks for oil or gas.

5.3 Organics

5.3.1 Locality 1. WAR Section, northern Bunkers Range

The only organic particles present within the Woodendinna Dolostone samples (WP0, WP1, WP2, and MM) derive from stromatolites, a microbial mat, and fragmented fossils, which reflects the restricted lagoonal facies that has been interpreted. Furthermore, Betts et al. (2016) reported that no small shelly fossils have been retrieved from this location. Aliphatic carbon-hydrogen methylene stretching modes were detected by FTIR in WP0 (Fig. 29). Whilst these may be an artefact of thermal maturation processes, they may also reflect bacterial input. In modern day sedimentary environments that have low to no terrigenous matter, these chains have been observed as the result of residues of algal biomass (Blokker et al., 2000; Zang et al., 2001).

The Wilkawillina Limestone sample (WAR/405) has fragmentary archaeocyaths throughout and some calcimicrobial fragments, and occurs at the base of the *Kulparina rostrata* zone (Fig. 6) as defined by Betts et al. (2016). This zone is pre-trilobitic and characterised by low diversity shelly fossils. The base of this biostratigraphic zone is defined by the eccentrothecimorph tommotiid *K. rostrata* and the paterinid brachiopod *Askepasma saproconcha*. WAR/405 represents small shallowing and biohermal accumulation of the Wilkawillina Limestone interfingering or onlapping with the lagoonal facies of the Wirrapowie limestone. This lateral interfingering is characterised by largely redeposited limestone, with archaeocyaths, clotted microbial textures, and small shelly fossils.

5.3.2 Locality 2. Wirrealpa Limestone, Bunkers Range

Throughout the TH samples from Locality 2, a variety of metazoans are seen in association with microbialites; brachiopod shell fragments (Figs 18 and 22), tubiform bioclasts (Fig. 20), eocrinoidal columnals and stem fragments (Fig. 20), chancelloriids (Fig. 21), and trilobite fragments (Fig. 22). There are also microbial precipitates present throughout (Fig. 20). The presence of a variety of fragmented fossils that vary with height up the stratigraphic column seem to be indicative of the

formation method of these thrombolites being depositional as suggested earlier, rather than due to the presence of borers or other factors, particularly as no borers are observed in these samples. Monomethyl alkanes also revealed different signatures for TH415 and TH82 (Fig. 51) which may reflect changes in depth of microbial communities, as suggested by Kenig et al., (1990), but also may be representative of significant metazoan taxa changes with depth.
SSWTH is a grain-supported oncolite, with bioclastic fragments of shell, tubes, spicules and trilobite fragments (Figs 24 and 26). The oncolites nucleated around trilobite fragments or chancelorriid sclerites, and rosettes grow around bacterial precipitates within this sample (Figs 23, 24 and 26). In both the thrombolitic samples and this oncolitic sample, there are no skeletal fossils preserved in life position.

5.3.3 Origin of biomolecules

All samples contain FTIR peaks between 1000-1150 cm^{-1} which is the main window for carbohydrate peaks (Mastandrea et al., 2011). This band could be diagnostic of either polysaccharide components (Schmitt and Flemming, 1998), or, more likely, silica (Innocenzi et al., 2003). Polysaccharide components are common in bacteria which use extracellular polysaccharides. Polysaccharide capsules are ubiquitous structures found on the cell surface of a broad range of bacterial species (Roberts, 1996). Polysaccharides have a variety of functions in bacteria including prevention of desiccation, and adherence (Roberts, 1996). Adherence is a commonly observed bacterial feature in these samples, with stromatolitic accretion forming and growing over flat pebble rip up clasts (Fig. 11), lithification into hardground surfaces and growth over those hard ground surfaces (Figs 14 and 15), thrombolitic growth over a variety of structures (Figs 19-22), rosettes around bacterial precipitates (Figs 20 and 22), microbial rinds growing around peloids (Fig. 23), and the nucleation of oncolites around fossil fragments (Figs 24 and 25). Bacteria, including cyanobacteria, are able to secrete extracellular polymeric substances (EPS); on sediment surfaces these can develop as well-defined protective envelopes surrounding cells as cyanobacterial sheaths (Riding, 2000). Clotted microfabrics have been known to result from these EPS (Riding, 2000). Furthermore, the Gunflint Chert in Canada has ancient *Leptothrix* cyanobacteria, which in the modern day produce enormous amounts of polysaccharides, particularly in association with Fe (Golubic and Seong-Joo, 1999). There is Fe content in these samples (Figs 38, 39, 41, 43 and 45), typically in layers with inorganic materials that have been chelated by organic material. Polysaccharides degrade quickly after death, but can be preserved in humic acid-like polymers or in the glycosidic parts of collagens (Bobroff et al., 2016). Fossilised bacterial polysaccharides have been reported from a cyanobacterial mat from the 440 Ma early Silurian Passage Creek biota (Tomescu et al., 2008), and chitin from a 505 Ma demosponge from the Burgess Shale (Ehrlich et

al., 2013). However, given the high thermal maturity of these samples this shouldered peak is more likely representative of silicification processes in post mature samples (McNeil et al., 2015). Sponge spicules and algae have been shown to display biogenically mediated silica, with vibration modes of the [SiO_4] tetrahedron. Furthermore, Innocenzi et al., (2003) showed that the shouldered silica peaks are actually convoluted spectra of several peaks which show different evolutions based on temperature grade (Fig. 57). and that the silica peak decreases with temperature (Fig. 58).

The high thermal maturity of these samples means that most of the hydrocarbons have been destroyed, and only homologous series of *n*-alkanes and mono-methylalkanes could be extracted from most samples. The isoprenoids Pr and Ph and some aromatic hydrocarbons are preserved, but are not indicative of any specific organic information. Additionally, no complex multi-ring biomarkers were detected. The *n*-alkanes that remain are long-chain *n*-alkanes which are generally indicative of terrigenous input, but these have no odd carbon number predominance. There is no evidence of any contamination as all procedural blanks were devoid of these analytes, and the results are consistent with one another (e.g. maturity parameters from extract geochemistry agree with the Raman data). Aharonovich et al., (2016) detected high molecular weight *n*-alkanes, with similar CPIs (between 0.99 and 1.05) to those detected in this study, in thermally mature (>200°C) mudstones from the Carboniferous Namoi Formation. Controversial hydrocarbon biomarkers from Archaean rocks (Brocks et al., 1999) were re-examined by French et al. (2015) to assess syngeneity and contamination potential. The study used ultra-clean drilling and laboratory protocols and showed that 1) there were no biomarkers in the internal parts of the Archaean samples, 2) some syngenetic compounds such as *n*-alkanes, diamondoids and aromatic hydrocarbons had survived to the present, and 3) that external surfaces had been exposed to contamination. Peters et al. (2016) showed that the reason for this was that the rocks were exposed to temperatures higher than 300°C and probably ~400°C, consistent with greenschist-facies metamorphism. Pedentchouk et al. (2006) noted increasing *n*-alkane chain lengths with depth and

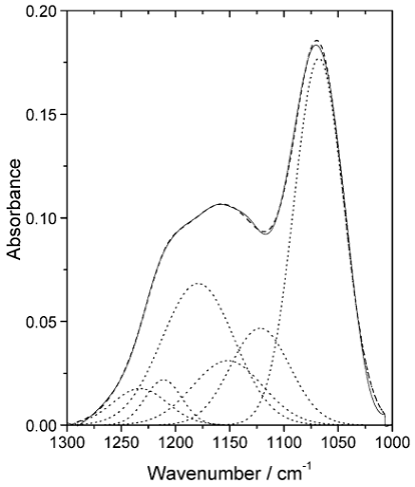

Figure 57. Deconvolution of the FTIR absorption spectrum, in the 1100-1300 cm^{-1} interval, for a silica film (Innocenzi et al., 2003).

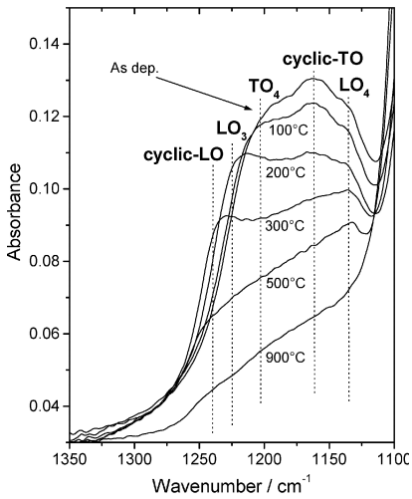

Figure 58. FTIR absorption spectra, in the range 110-1350 cm^{-1}, of silica mesoporous films treated at different temperatures (Innocenzi et al., 2003).

maturity in a continuous core from the Lower Cretaceous Kissendra Formation, but concluded that *n*-alkanes could preserve the original biological signal before the onset of oil generation. The procedural blanks in this study showed no evidence of any contamination. Thus, it is likely these residual hydrocarbons reflect a genuine syngenetic input that has been preserved in these sediments.

6. Conclusions

The Cambrian Period represents a shift from a unicellular dominated marine realm to a multicellular dominated biosphere. The Cambrian is a time with widespread evidence for bioturbation, mineralisation and a number of other evolutionary and ecological milestones including the rise of predation and the first animal-based reefs. Research on Cambrian palaeobiology is important for untangling the relationships between evolutionary innovation, ecological interactions and how ecosystems are engineered. The radiation of animals led to the widespread demise of microbial ecosystems of the Precambrian. Although there has been a lot of research into stromatolite evolution and prevalence through Earth's Precambrian history, there have been few detailed studies on the effect of multicellular (especially animal) evolution on microbialites and stromatolites throughout the early to mid-Cambrian. The presence of these holdover microbial forms in the Arrowie Basin provided an opportunity to investigate the architecture, geochemistry, depositional environments of these relic ecosystems.

6.1. Aim: Describe and reconstruct the depositional environments of the samples in this study.

Outcome: Two samples from the Cambrian Stage 2, Woodendinna Dolostone (WP0 and WP1) are interpreted as being formed in relatively shallow, supratidal to sabkha evaporative environments. The firmground surface in WP2 and MM suggests slow sedimentation rates which transitioned into a restricted lagoonal environment. The Archaeocyath framestone sample (WAR/405) represents a brief shallow shelf (?patch reef) formed under stable marine conditions.

The thrombolites of the Cambrian Stage 5 Wirrealpa Limestone were likely deposited subtidally prior to transgression, wherein a low-energy, subtidal environment with high levels of $CaCO_3$ caused the precipitation of the clays. This environment is consistent with the formation of the oncolite, and is characterised by fragmented fossils and celestine that indicate a previously high energy evaporative environment that transitioned into a calmer environment at the height of the transgression.

6.2. Aim: To assess the thermal maturity of the samples taken from the Arrowie Basin.

Outcome: Raman, FTIR, and organic geochemical results are consistent and indicate that the samples from both localities were highly mature (>200°C). The samples from Locality 1 are more thermally mature than those from Locality 2, suggesting a decrease in thermal maturity from the older to the younger strata in the basin, especially above the regionally significant karstic Flinders disconformity associated with the reddened horizon.

6. 3. Aim: To examine the organics present in the samples of this study, with particular attention to the interactions between microbialites and metazoans.

Outcome: At both locations microbes were either not found in association with metazoans or only found in association with fossils not preserved in life position. The high thermal maturity of the samples resulted in the destruction of most of the hydrocarbons. However, *n*-alkanes and monomethylalkanes were detected in several samples, and FTIR revealed carbohydrate absorption bands that may be related to EPS secretions by bacteria, or silicification of fossils.

References

Aharonovich, S., and George, S., 2016, A possible shale gas prospect? First results of the organic composition and thermal maturity of the Carboniferous Namoi Formation, northern NSW, Australia: Australian Journal of Earth Sciences, v. 63, no. 6, p. 771-780.

Aitken, J., 1967, Classification and environmental significance of cryptalgal limestones and dolomites, with illustrations from the Cambrian and Ordovician of southwestern Alberta: Journal of Sedimentary Research, v. 37, no. 4.

Allwood, A., Hurowitz, J., Tice, M., Hodyss, R., Knowles, E., and Wade, L., Investigating ancient microbial biosignatures with Micro-XRF in situ elemental analysis, *in* Proceedings AGU Fall Meeting Abstracts 2013.

Allwood, A. C., Walter, M. R., and Marshall, C. P., 2006, Raman spectroscopy reveals thermal palaeoenvironments of c. 3.5 billion-year-old organic matter: Vibrational Spectroscopy, v. 41, no. 2, p. 190-197.

Anderson, M. S., Andringa, J. M., Carlson, R. W., Conrad, P., Hartford, W., Shafer, M., Soto, A., Tsapin, A. I., Dybwad, J. P., and Wadsworth, W., 2005, Fourier transform infrared spectroscopy for Mars science: Review of Scientific Instruments, v. 76, no. 3, p. 034101.

Aoya, M., Kouketsu, Y., Endo, S., Shimizu, H., Mizukami, T., Nakamura, D., and Wallis, S., 2010, Extending the applicability of the Raman carbonaceous-material geothermometer using data from contact metamorphic rocks: Journal of Metamorphic Geology, v. 28, no. 9, p. 895-914.

Awramik, S. M., Hoover, R. B., Grey, K., Levin, G. V., Rozanov, A. Y., and Gladstone, G. R., 2005, Stromatolites: biogenicity, biosignatures, and bioconfusion: Optics and Photonics 2005, v. 5906, p. 59060P.

Bengtson, S., Morris, S. C., and Cooper, B., 1990, Early Cambrian fossils from south Australia: Association of Australian Palaeontologists, v. 9, p. 1-364.

Betts, M. J., Paterson, J. R., Jago, J. B., Jacquet, S. M., Skovsted, C. B., Topper, T. P., and Brock, G. A., 2016, A new lower Cambrian shelly fossil biostratigraphy for South Australia: Gondwana Research, v. 36, p. 176-208.

Beyssac, O., Goffé, B., Chopin, C., and Rouzaud, J., 2002, Raman spectra of carbonaceous material in metasediments: a new geothermometer: Journal of metamorphic Geology, v. 20, no. 9, p. 859-871.

Bischoff, G., 1976, Dailyatia, a new genus of the Tommotiidae from Cambrian strata of SE Australia (Crustacea, Cirripedia): Senckenbergiana lethaea, v. 57, no. 1, p. 1-33.

Blokker, P., Schouten, S., de Leeuw, J. W., Damsté, J. S. S., and van den Ende, H., 2000, A comparative study of fossil and extant algaenans using ruthenium tetroxide degradation: Geochimica et Cosmochimica Acta, v. 64, no. 12, p. 2055-2065.

Bobroff, V., Chen, H.-H., Javerzat, S., and Petibois, C., 2016, What can infrared spectroscopy do for characterizing organic remnant in fossils?: TrAC Trends in Analytical Chemistry, v. 82, p. 443-456.

Braga, J. C., Martin, J. M., and Riding, R., 1995, Controls on microbial dome fabric development along a carbonate-siliciclastic shelf-basin transect, Miocene, SE Spain: Palaios, v. 10, no. 4, p. 347-361.

Briggs, D. E., and Summons, R. E., 2014, Ancient biomolecules: their origins, fossilization, and role in revealing the history of life: Bioessays, v. 36, no. 5, p. 482-490.

Brock, G., 2017, Unpublished data, *in* Teece, B., ed.: email communication.

Brock, G., Engelbretsen, M., Jago, J., Kruse, P., Laurie, J., Shergold, J., Shi, G., and Sorauf, J., 2000, Palaeobiogeographic affinities of Australian Cambrian faunas: Memoir of the Association of Australasian Palaeontologists, v. 23, p. 1-61.

Brock, G. A., and Cooper, B. J., 1993, Shelly fossils from the Early Cambrian (Toyonian) Wirrealpa, Aroona Creek, and Ramsay limestones of South Australia: Journal of Paleontology, v. 67, no. 5, p. 758-787.

Brocks, J. J., Buick, R., Summons, R. E., and Logan, G. A., 2003, A reconstruction of Archean biological diversity based on molecular fossils from the 2.78 to 2.45 billion-year-old Mount Bruce Supergroup, Hamersley Basin, Western Australia: Geochimica et Cosmochimica Acta, v. 67, no. 22, p. 4321-4335.

Brocks, J. J., Jarrett, A. J., Sirantoine, E., Hallmann, C., Hoshino, Y., and Liyanage, T., 2017, The rise of algae in Cryogenian oceans and the emergence of animals: Nature, v. 548.7669, no. 7669, p. 578-581.

Brocks, J. J., Logan, G. A., Buick, R., and Summons, R. E., 1999, Archean molecular fossils and the early rise of eukaryotes: science, v. 285, no. 5430, p. 1033-1036.

Brocks, J. J., and Pearson, A., 2005, Building the biomarker tree of life: Reviews in Mineralogy and Geochemistry, v. 59, no. 1, p. 233-258.

Bush, A. M., Bambach, R. K., and Erwin, D. H., 2011, Ecospace Utilization During the Ediacaran Radiation and the Cambrian Eco-explosion, Quantifying the Evolution of Early Life Volume 36: Netherlands, Springer, p. 111-133.

Carr, L., Korsch, R., Jones, L., and Holzschuh, J., 2010, The role of deep seismic reflection data in understanding the architecture and petroleum potential of Australia's onshore sedimentary basins: The APPEA Journal, v. 50, no. 2, p. 726-726.

Chen, L., Wang, Y., Xie, S., Kershaw, S., Dong, M., Yang, H., Liu, H., and Algeo, T. J., 2011, Molecular records of microbialites following the end-Permian mass extinction in Chongyang, Hubei Province, South China: Palaeogeography, Palaeoclimatology, Palaeoecology, v. 308, no. 1-2, p. 151-159.

Chen, Y., Zou, C., Mastalerz, M., Hu, S., Gasaway, C., and Tao, X., 2015, Applications of Micro-Fourier Transform Infrared Spectroscopy (FTIR) in the Geological Sciences--A Review: International Journal of Molecular Science, v. 16, no. 12, p. 30223-30250.

Chopra, A., and Lineweaver, C. H., 2016, The case for a Gaian bottleneck: the biology of habitability: Astrobiology, v. 16, no. 1, p. 7-22.

Christ, N., Immenhauser, A., Wood, R. A., Darwich, K., and Niedermayr, A., 2015, Petrography and environmental controls on the formation of Phanerozoic marine carbonate hardgrounds: Earth-Science Reviews, v. 151, p. 176-226.

Coulson, K. P., and Brand, L. R., 2016, Lithistid sponge-microbial reef-building communities construct laminated, upper Cambrian (Furongian) 'Stromatolites': Palaios, v. 31, no. 7, p. 358-370.

Daily, B., Aspects of carbonate sedimentation in the Cambrian of South Australia, *in* Proceedings Abstracts, Joint Specialists Groups Meetings, Canberra, Geological Society of Australia1972.

De La Pierre, M., Carteret, C., Maschio, L., André, E., Orlando, R., and Dovesi, R., 2014, The Raman spectrum of CaCO3 polymorphs calcite and aragonite: a combined experimental and computational study: The Journal of Chemical Physics, v. 140, no. 16, p. 164509.

Delben, F., and Muzzarelli, R. A., 1989, Thermodynamic study of the interaction of N-carboxymethyl chitosan with divalent metal ions: Carbohydrate Polymers, v. 11, no. 3, p. 221-232.

Douglas, S., Perry, M. E., Abbey, W. J., Tanaka, Z., Chen, B., and McKay, C. P., 2015, The structure and chemical layering of Proterozoic stromatolites in the Mojave Desert: International Journal of Astrobiology, v. 14, no. 3, p. 517-526.

Ehrlich, H., Rigby, J. K., Botting, J., Tsurkan, M., Werner, C., Schwille, P., Petrášek, Z., Pisera, A., Simon, P., and Sivkov, V., 2013, Discovery of 505-million-year old chitin in the basal demosponge Vauxia gracilenta: Scientific reports, v. 3, p. 1-6.

Erwin, D. H., Laflamme, M., Tweedt, S. M., Sperling, E. A., Pisani, D., and Peterson, K. J., 2011, The Cambrian conundrum: early divergence and later ecological success in the early history of animals: Science, v. 334, no. 6059, p. 1091-1097.

Ferralis, N., 2010, Probing mechanical properties of graphene with Raman spectroscopy: Journal of Materials Science, v. 45, no. 19, p. 5135-5149.

Flannery, D. T., Allwood, A. C., and Van Kranendonk, M. J., 2016, Lacustrine facies dependence of highly 13 C-depleted organic matter during the global age of methanotrophy: Precambrian Research, v. 285, p. 216-241.
Flügel, E., 2004, Limestones are Biological Sediments, Microfacies of Carbonate Rocks, Springer, p. 369-398.
Fowler, M., and Douglas, A. G., 1987, Saturated hydrocarbon biomarkers in oils of Late Precambrian age from Eastern Siberia: Organic geochemistry, v. 11, no. 3, p. 201-213.
French, K. L., Hallmann, C., Hope, J. M., Schoon, P. L., Zumberge, J. A., Hoshino, Y., Peters, C. A., George, S. C., Love, G. D., Brocks, J. J., Buick, R., and Summons, R. E., 2015, Reappraisal of hydrocarbon biomarkers in Archean rocks: Proceedings of the National Academy of Sciences, v. 112, no. 19, p. 5915-5920.
Garcia-Pichel, F., Al-Horani, F. A., Farmer, J. D., Ludwig, R., and Wade, B. D., 2004, Balance between microbial calcification and metazoan bioerosion in modern stromatolitic oncolites: Geobiology, v. 2, no. 1, p. 49-57.
George, S. C., Lisk, M., Eadington, P. J., and Quezada, R. A., Geochemistry of a palaeo-oil column: Octavius 2, Vulcan Sub-basin, *in* Proceedings Proceedings of Petroleum Exploration Society of Australia Symposium, The Sedimentary Basins of Western Australia 1998, Volume 2, p. 195-210.
Golubic, S., and Seong-Joo, L., 1999, Early cyanobacterial fossil record: preservation, palaeoenvironments and identification: European Journal of Phycology, v. 34, no. 4, p. 339-348.
Gravestock, D., and Cowley, W., 1995, Arrowie Basin: The Geology of South Australia, v. 2, p. 20-31.
Grotzinger, J. P., and Knoll, A. H., 1999, Stromatolites in Precambrian carbonates: evolutionary mileposts or environmental dipsticks?: Annual Review of Earth and Planetary Sciences, v. 27, no. 1, p. 313-358.
Groves, I. M., Carman, C. E., and Dunlap, W. J., 2003, Geology of the Beltana willemite deposit, Flinders Ranges, south Australia: Economic Geology, v. 98, no. 4, p. 797-818.
Gunasekaran, S., Anbalagan, G., and Pandi, S., 2006, Raman and infrared spectra of carbonates of calcite structure: Journal of Raman Spectroscopy, v. 37, no. 9, p. 892-899.
Hanor, J. S., 2004, A model for the origin of large carbonate-and evaporite-hosted celestine (SrSO4) deposits: Journal of Sedimentary Research, v. 74, no. 2, p. 168-175.
Harwood Theisen, C., and Sumner, D. Y., 2016, Thrombolite fabrics and origins: Influences of diverse microbial and metazoan processes on Cambrian thrombolite variability in the Great Basin, California and Nevada: Sedimentology, v. 63, no. 7, p. 2217-2252.
Haslett, P., 1975, The Woodendinna Dolomite and Wirrapowie Limestone—two new Lower Cambrian formations, Flinders Ranges, South Australia: Transactions of the Royal Society of South Australia, v. 99, p. 211-220.
Hicks, M., and Rowland, S. M., 2009, Early Cambrian microbial reefs, archaeocyathan inter-reef communities, and associated facies of the Yangtze Platform: Palaeogeography, Palaeoclimatology, Palaeoecology, v. 281, no. 1, p. 137-153.
Hong, Y. K., Tong, C., Wei, Q. L., and Pei, S. P., 2015, Research Development of Flat-pebble Conglomerate Characteristics and Their Origin in Early Paleozoic North China Platform: Acta Sedimentologica Sinica, v. 6, p. 005.
Hoshino, Y., Flannery, D., Walter, M., and George, S., Investigating the syngeneity and paleobiology of hydrocarbon biomarkers in the Fortescue Group at 2.7-2.8 Ga 2012, International Geological Congress.
Hoshino, Y., and George, S. C., 2015, Cyanobacterial Inhabitation on Archean Rock Surfaces in the Pilbara Craton, Western Australia: Astrobiology, v. 15, no. 7, p. 559-574.
Illing, C. J., Hallmann, C., Miller, K. E., Summons, R. E., and Strauss, H., 2014, Airborne hydrocarbon contamination from laboratory atmospheres: Organic Geochemistry, v. 76, p. 26-38.

Innocenzi, P., Falcaro, P., Grosso, D., and Babonneau, F., 2003, Order− disorder transitions and evolution of silica structure in self-assembled mesostructured silica films studied through FTIR spectroscopy: The Journal of Physical Chemistry B, v. 107, no. 20, p. 4711-4717.

Jago, J. B., Gatehouse, C., Powell, C. M., and Casey, T., 2013, Implications of cross-bedding data from the upper part of the Cambrian succession, Arrowie Basin, South Australia: Australian Journal of Earth Sciences, v. 60, no. 2, p. 231-240.

Jago, J. B., Gehling, J. G., Paterson, J. R., Brock, G. A., and Zang, W., 2012, Cambrian stratigraphy and biostratigraphy of the Flinders Ranges and the north coast of Kangaroo Island, South Australia: Episodes, v. 35, no. 1, p. 247-255.

Jago, J. B., Zang, W.-L., Sun, X., Brock, G., Paterson, J., and Skovsted, C., 2006, A review of the Cambrian biostratigraphy of South Australia: Palaeoworld, v. 15, no. 3-4, p. 406-423.

Jahnert, R. J., and Collins, L. B., 2012, Characteristics, distribution and morphogenesis of subtidal microbial systems in Shark Bay, Australia: Marine Geology, v. 303, p. 115-136.

James, N. P., 1984, Shallowing-upward sequences in carbonates, *in* Walker, R. G., ed., Facies Models: Toronto, Geological Association of Canada, p. 213–228.

James, N. P., and Gravestock, D. I., 1990, Lower Cambrian shelf and shelf margin buildups, Flinders Ranges, South Australia: Sedimentology, v. 37, no. 3, p. 455-480.

Kalnicky, D. J., and Singhvi, R., 2001, Field portable XRF analysis of environmental samples: Journal of Hazardous Materials, v. 83, no. 1, p. 93-122.

Kenig, F., Damsté, J. S. S., Kock-van Dalen, A., Rijpstra, W. I. C., Huc, A. Y., and de Leeuw, J. W., 1995, Occurrence and origin of mono-, di-, and trimethylalkanes in modern and Holocene cyanobacterial mats from Abu Dhabi, United Arab Emirates: Geochimica et Cosmochimica Acta, v. 59, no. 14, p. 2999-3015.

Kenig, F., Huc, A. Y., Purser, B. H., and Oudin, J.-L., 1990, Sedimentation, distribution and diagenesis of organic matter in a recent carbonate environment, Abu Dhabi, UAE: Organic Geochemistry, v. 16, no. 4-6, p. 735-747.

Kennard, J. M., and James, N. P., 1986, Thrombolites and stromatolites: two distinct types of microbial structures: Palaios, p. 492-503.

Klomp, U., 1986, The chemical structure of a pronounced series of iso-alkanes in South Oman crudes: Organic Geochemistry, v. 10, no. 4-6, p. 807-814.

Knoll, A. H., Bergmann, K. D., and Strauss, J. V., 2016, Life: the first two billion years: Philosophical Transactions of the Royal Society B, v. 371, no. 1707, p. 20150493.

Kovač, N., 2009, Chemical characterization of stromatolitic 'petola'layer (Sečovlje salt-pans, Slovenia) using FT-IR spectroscopy: Annales Series Historia Naturalis, v. 19, p. 1-8.

Krishnamurti, D., The Raman spectrum of calcite and its interpretation, *in* Proceedings Proceedings of the National Academy of Sciences, India Section A: Physical Sciences 1957, Volume 46, p. 183-202.

Kruse, P. D., 1991, Cyanobacterial–archaeocyathan–radiocyathan bioherms in the Wirrealpa Limestone of South Australia: Canadian Journal of Earth Sciences, v. 28, no. 4, p. 601-615.

Kuznetsov, V. G., and Suchy, V., 1992, Vendian-Cambrian tidal and sabkha facies of the Siberian platform: Facies, v. 27, no. 1, p. 285-293.

La Russa, M. F., Ruffolo, S. A., Barone, G., Crisci, G. M., Mazzoleni, P., and Pezzino, A., 2009, The Use of FTIR and Micro-FTIR Spectroscopy: An Example of Application to Cultural Heritage: International Journal of Spectroscopy, v. 2009, p. 1-5.

Liu, D., Dong, H., Bishop, M., Zhang, J., Wang, H., Xie, S., Wang, S., Huang, L., and Eberl, D., 2012, Microbial reduction of structural iron in interstratified illite-smectite minerals by a sulfate-reducing bacterium: Geobiology, v. 10, no. 2, p. 150-162.

Lu, Y., Chang, W., Chien, Y., Chu, C., Lin, H., Zhou, Z., Qian, Y., Zhang, S., and Yuan, J., 1974, Cambrian trilobites, Handbook of Stratigraphy and Paleontology of Southwest China: Beijing, Science Press, p. 82–107.

Łuczyński, P., and Kozłowski, W., 2014, Stromatoporoid beds and flat-pebble conglomerates interpreted as tsunami deposits in the Upper Silurian of Podolia, Ukraine: Acta Geologica Polonica, v. 64, no. 3, p. 261-280.

Marshall, C. P., Edwards, H. G., and Jehlicka, J., 2010, Understanding the application of Raman spectroscopy to the detection of traces of life: Astrobiology, v. 10, no. 2, p. 229-243.

Marshall, C. P., Love, G. D., Snape, C. E., Hill, A. C., Allwood, A. C., Walter, M. R., Van Kranendonk, M. J., Bowden, S. A., Sylva, S. P., and Summons, R. E., 2007, Structural characterization of kerogen in 3.4 Ga Archaean cherts from the Pilbara Craton, Western Australia: Precambrian Research, v. 155, no. 1, p. 1-23.

Marshall, C. P., and Olcott Marshall, A., 2013, Raman hyperspectral imaging of microfossils: potential pitfalls: Astrobiology, v. 13, no. 10, p. 920-931.

Marshall, C. R., 2006, Explaining the Cambrian “explosion” of animals: Annual Review of Earth and Planetary Sciences, v. 34, p. 355-384.

Mastandrea, A., Guido, A., Demasi, F., Ruffolo, S. A., and Russo, F., 2011, The characterisation of sedimentary organic matter in carbonates with Fourier-Transform Infrared (FTIR) spectroscopy, Advances in Stromatolite Geobiology, Springer, p. 331-342.

Mata, S., and Bottjer, D., 2012, Microbes and mass extinctions: paleoenvironmental distribution of microbialites during times of biotic crisis: Geobiology, v. 10, no. 1, p. 3-24.

McNeil, D. H., Schulze, H. G., Matys, E., and Bosak, T., 2015, Raman spectroscopic analysis of carbonaceous matter and silica in the test walls of recent and fossil agglutinated foraminifera: AAPG Bulletin, v. 99, no. 6, p. 1081-1097.

Menzel, F., Blaimer, B. B., and Schmitt, T., How do cuticular hydrocarbons evolve? Physiological constraints and climatic and biotic selection pressures act on a complex functional trait, *in* Proceedings Proc. R. Soc. B2017, Volume 284, The Royal Society, p. 20161727.

Moore, H. E., Butcher, J. B., Adam, C. D., Day, C. R., and Drijfhout, F. P., 2016, Age estimation of Calliphora (Diptera: Calliphoridae) larvae using cuticular hydrocarbon analysis and Artificial Neural Networks: Forensic science international, v. 268, p. 81-91.

Moore, P., 1980, Stratigraphy and depositional environments of the Billy Creek Formation (Cambrian), east of the Flinders Ranges, South Australia: Transactions of the Royal Society of South Australia, v. 104, p. 117-132.

Mukhopadhyay, A., and Thorie, A., 2016, Comparative study of two relatives, MISS and Stromatolites: example from the Proterozoic Kunihar Formation, Simla Group, Lesser Himalaya: Arabian Journal of Geosciences, v. 9, no. 9, p. 1-23.

Murphy, R., Van Kranendonk, M., Kelloway, S., and Wainwright, I., 2016, Complex patterns in fossilized stromatolites revealed by hyperspectral imaging (400–2496 nm): Geobiology, v. 14, no. 5, p. 419-439.

Myrow, P. M., Tice, L., Archuleta, B., Clark, B., Taylor, J. F., and Ripperdan, R. L., 2004, Flat-pebble conglomerate: its multiple origins and relationship to metre-scale depositional cycles: Sedimentology, v. 51, no. 5, p. 973-996.

Nwadinigwe, C., and Alumona, T., 2017, Assessment of n-alkanes and acyclic isoprenoids (geochemical markers) in crudes: A case study of Iraq and Niger delta, Nigeria: Egyptian Journal of Petroleum, v. in press.

Olcott Marshall, A., and Cestari, N. A., 2015, Biomarker Analysis of Samples Visually Identified as Microbial in the Eocene Green River Formation: An Analogue for Mars: Astrobiology, v. 15, no. 9, p. 770-775.

Olcott Marshall, A., and Marshall, C. P., 2015, Vibrational spectroscopy of fossils: Palaeontology, v. 58, no. 2, p. 201-211.
Olcott Marshall, A., Wehrbein, R. L., Lieberman, B. S., and Marshall, C. P., 2012, Raman spectroscopic investigations of Burgess Shale–type preservation: a new way forward: Palaios, v. 27, no. 5, p. 288-292.
Olivares, M., Irazola, M., Murelaga, X., Baceta, J., Tarriño, A., Castro, K., and Etxebarria, N., 2013, Sourcing sedimentary cherts with archaeological use through the combination of chromatographic and spectroscopic techniques: Applied geochemistry, v. 33, p. 252-259.
Pagès, A., Schmid, S., Edwards, D., Barnes, S., He, N., and Grice, K., 2016, A molecular and isotopic study of palaeoenvironmental conditions through the middle Cambrian in the Georgina Basin, central Australia: Earth and Planetary Science Letters, v. 447, p. 21-32.
Paterson, J. R., and Brock, G. A., 2007, Early Cambrian trilobites from Angorichina, Flinders Ranges, South Australia, with a new assemblage from the Pararaia bunyerooensis Zone: Journal of Paleontology, v. 81, no. 1, p. 116-142.
Pawlowska, M. M., Butterfield, N. J., and Brocks, J. J., 2013, Lipid taphonomy in the Proterozoic and the effect of microbial mats on biomarker preservation: Geology, v. 41, no. 2, p. 103-106.
Peckmann, J., Thiel, V., Reitner, J., Taviani, M., Aharon, P., and Michaelis, W., 2004, A microbial mat of a large sulfur bacterium preserved in a Miocene methane-seep limestone: Geomicrobiology Journal, v. 21, no. 4, p. 247-255.
Pedentchouk, N., Freeman, K. H., and Harris, N. B., 2006, Different response of δD values of n-alkanes, isoprenoids, and kerogen during thermal maturation: Geochimica et Cosmochimica Acta, v. 70, no. 8, p. 2063-2072.
Peng, S. C., and Babcock, L., 2001, Cambrian of the Hunan-Guizhou region, South China: Palaeoworld, v. 13, p. 3-51.
Peryt, T. M., Peryt, D., Jasionowski, M., Poberezhskyy, A. V., and Durakiewicz, T., 2004, Post-evaporitic restricted deposition in the Middle Miocene Chokrakian-Karaganian of East Crimea (Ukraine): Sedimentary Geology, v. 170, no. 1, p. 21-36.
Peters, K. E., Walters, C. C., and Moldowan, J. M., 2005, The biomarker guide, Cambridge University Press.
Pflug, H. D., and Jaeschke-Boyer, H., 1979, Combined structural and chemical analysis of 3,800-Myr-old microfossils: Nature, v. 280, no. 5722, p. 483-486.
Preston, L. J., and Genge, M. J., 2010, The Rhynie Chert, Scotland, and the search for life on Mars: Astrobiology, v. 10, no. 5, p. 549-560.
Preston, L. J., Melim, L. A., Polyak, V. J., Asmerom, Y., and Southam, G., 2014, Infrared Spectroscopic Biosignatures from Hidden Cave, New Mexico: Possible Applications for Remote Life Detection: Geomicrobiology Journal, v. 31, no. 10, p. 929-941.
Quezergue, K. R., 2014, Mesoscale X-Ray Fluorescence (XRF) Mapping Reveals Growth Processes for Stromatolites from the Nsuze Group [Master of Science]: Texas A&M University.
Radke, M., Welte, D. H., and Willsch, H., 1982, Geochemical study on a well in the Western Canada Basin: relation of the aromatic distribution pattern to maturity of organic matter: Geochimica et Cosmochimica Acta, v. 46, no. 1, p. 1-10.
Rajput, S., Li, Y., and Li, L., 2014, Direct experimental evidence for the reversal of carrier type upon hydrogen intercalation in epitaxial graphene/SiC (0001): Applied Physics Letters, v. 104, no. 4, p. 041908.
Reig, F., 2002, FTIR quantitative analysis of calcium carbonate (calcite) and silica (quartz) mixtures using the constant ratio method. Application to geological samples: Talanta, v. 58, no. 4, p. 811-821.
Riding, R., 1991, Classification of microbial carbonates: Calcareous algae and stromatolites, v. 2, p. 1-51.
Riding, R., 2000, Microbial carbonates: the geological record of calcified bacterial–algal mats and biofilms: Sedimentology, v. 47, no. s1, p. 179-214.

Riding, R., 2006, Microbial carbonate abundance compared with fluctuations in metazoan diversity over geological time: Sedimentary Geology, v. 185, no. 3, p. 229-238.
-, 2011, The nature of stromatolites: 3,500 million years of history and a century of research, Advances in Stromatolite Geobiology, Springer, p. 29-74.
Roberts, I. S., 1996, The biochemistry and genetics of capsular polysaccharide production in bacteria: Annual Reviews in Microbiology, v. 50, no. 1, p. 285-315.
Rontani, J.-F., and Volkman, J. K., 2003, Phytol degradation products as biogeochemical tracers in aquatic environments: Organic Geochemistry, v. 34, no. 1, p. 1-35.
Schmitt, J., and Flemming, H.-C., 1998, FTIR-spectroscopy in microbial and material analysis: International Biodeterioration & Biodegradation, v. 41, no. 1, p. 1-11.
Schubert, J. K., and Bottjer, D. J., 1992, Early Triassic stromatolites as post-mass extinction disaster forms: Geology, v. 20, no. 10, p. 883-886.
Sheehan, P. M., and Harris, M. T., 2004, Microbialite resurgence after the Late Ordovician extinction: Nature, v. 430, no. 6995, p. 75.
Shi, G. R., and Chen, Z.-Q., 2006, Lower Permian oncolites from South China: Implications for equatorial sea-level responses to Late Palaeozoic Gondwanan glaciation: Journal of Asian Earth Sciences, v. 26, no. 3, p. 424-436.
Shiea, J., Brassell, S. C., and Ward, D. M., 1990, Mid-chain branched mono-and dimethyl alkanes in hot spring cyanobacterial mats: a direct biogenic source for branched alkanes in ancient sediments?: Organic Geochemistry, v. 15, no. 3, p. 223-231.
Soares, E. R. P., Batista, N. R., da Silva Souza, R., de Oliveira Torres, V., Cardoso, C. A. L., Nascimento, F. S., and Antonialli-Junior, W. F., 2017, Variation of cuticular chemical compounds in three species of Mischocyttarus (Hymenoptera: Vespidae) eusocial wasps: Revista Brasileira de Entomologia, v. 61, no. 3, p. 224-231.
Soudry, D., and Weissbrod, T., 1995, Morphogenesis and facies relationships of thrombolites and siliciclastic stromatolites in a Cambrian tidal sequence (Elat area, southern Israel): Palaeogeography, Palaeoclimatology, Palaeoecology, v. 114, no. 2-4, p. 339-355.
Stökl, J., Dandekar, A.-T., and Ruther, J., 2014, High chemical diversity in a wasp pheromone: a blend of methyl 6-methylsalicylate, fatty alcohol acetates and cuticular hydrocarbons releases courtship behavior in the Drosophila parasitoid Asobara tabida: Journal of chemical ecology, v. 40, no. 2, p. 159-168.
Stratigraphy, I. C. o., 2017, ICS - Chart/Time Scale.
Summons, R. E., Brassell, S. C., Eglinton, G., Evans, E., Horodyski, R. J., Robinson, N., and Ward, D. M., 1988, Distinctive hydrocarbon biomarkers from fossiliferous sediment of the Late Proterozoic Walcott Member, Chuar Group, Grand Canyon, Arizona: Geochimica et Cosmochimica Acta, v. 52, no. 11, p. 2625-2637.
Sun, J., Wu, Z., Cheng, H., Zhang, Z., and Frost, R. L., 2014, A Raman spectroscopic comparison of calcite and dolomite: Spectrochimica Acta Part A: Molecular and Biomolecular Spectroscopy, v. 117, p. 158-162.
Tomescu, A., Honegger, R., and Rothwell, G., 2008, Earliest fossil record of bacterial–cyanobacterial mat consortia: the early Silurian Passage Creek biota (440 Ma, Virginia, USA): Geobiology, v. 6, no. 2, p. 120-124.
Topper, T. P., Holmer, L. E., Skovsted, C. B., Brock, G. A., Balthasar, U., Larsson, C. M., Stolk, S. P., and Harper, D. A., 2013, The oldest brachiopods from the lower Cambrian of South Australia: Acta Palaeontologica Polonica, v. 58, no. 1, p. 93-109.
Tosti, F., Guido, A., Demasi, F., Mastandrea, A., Naccarato, A., Tagarelli, A., and Russo, F., 2011, Microbialites as primary builders of the Ladinian-Carnian platforms in the Dolomites: biogeochemical characterization: Geo Alp, v. 8, p. 156-162.

Turner, S., Blichert-Toft, J., Schaefer, B., Albarède, F., and Foden, J., 2017, A reappraisal of the evolution of the palaeo-Pacific margin of Gondwana from the Pb and Os isotope systematics of igneous rocks from the southern Adelaide fold belt, South Australia: Gondwana Research, v. 45, p. 152-162.

Walcott, C., 1905, Cambrian Faunas of China, Nos. 1 & 2: Proceedings of the United States National Museum, v. 30, p. 1911.

WANG, W., ZHOU, Z. Y., and YU, P., 2005, Relations Between Vitrinite Reflectance, Peek Temperature and its Neighboring Temperature Variation Rate: A Comparison of Methods: Chinese Journal of Geophysics, v. 48, no. 6, p. 1443-1453.

Wehrmeister, U., Jacob, D., Soldati, A., Loges, N., Häger, T., and Hofmeister, W., 2011, Amorphous, nanocrystalline and crystalline calcium carbonates in biological materials: Journal of Raman Spectroscopy, v. 42, no. 5, p. 926-935.

Wehrmeister, U., Soldati, A., Jacob, D., Häger, T., and Hofmeister, W., 2010, Raman spectroscopy of synthetic, geological and biological vaterite: a Raman spectroscopic study: Journal of Raman Spectroscopy, v. 41, no. 2, p. 193-201.

Wilmeth, D. T., Corsetti, F. A., Bisenic, N., Dornbos, S. Q., Oji, T., and Gonchigdorj, S., 2015, Punctuated growth of microbial cones within Early Cambrian oncoids, Bayan Gol Formation, Western Mongolia: Palaios, v. 30, no. 12, p. 836-845.

Wright, V. P., and Cherns, L., 2016, Leaving no stone unturned: the feedback between increased biotic diversity and early diagenesis during the Ordovician: Journal of the Geological Society, v. 173, no. 2, p. 241-244.

Yin, G., and Li, S., 1978, Palaeontological Atlas of Southwest China. Guizhou Province. I. Cambrian–Devonian, Geological Publishing House Beijing, China.

Youngs, B. C., 1977, The sedimentology of the Cambrian Wirrealpa and Aroona Creek limestones, Department of Mines, Geological Survey of South Australia.

Zang, W.-L., Jago, J., Alexander, E., and Paraschivoiu, E., 2004, A review of basin evolution, sequence analysis and petroleum potential of the frontier Arrowie Basin, South Australia: Pesa Eastern Australasian Basins Symposium II.

Zang, X., Nguyen, R. T., Harvey, H. R., Knicker, H., and Hatcher, P. G., 2001, Preservation of proteinaceous material during the degradation of the green alga Botryococcus braunii: a solid-state 2D 15 N 13 C NMR spectroscopy study: Geochimica et Cosmochimica Acta, v. 65, no. 19, p. 3299-3305.

Zhang, X. L., Han, J., Zhang, Z. F., Liu, H. Q., and Shu, D. G., 2003, Reconsideration of the supposed naraoiid larva from the Early Cambrian Chengjiang Lagerstätte, South China: Palaeontology, v. 46, no. 3, p. 447-465.

Zhou, Z., and Yuan, J., 1980, Lower Cambrian trilobite succession in southwest China: Acta Palaeontologica Sinica, v. 19, no. 4, p. 331-339.

Zhuravlev, A. Y., 1996, Reef ecosytem recovery after the Early Cambrian extinction: Geological Society, London, Special Publications, v. 102, no. 1, p. 79-96.

Zhuravlev, A. Y., and Wood, R. A., 1996, Anoxia as the cause of the mid-Early Cambrian (Botomian) extinction event: Geology, v. 24, no. 4, p. 311-314.

Zürcher, S., Wäckerlin, D., Bethuel, Y., Malisova, B., Textor, M., Tosatti, S., and Gademann, K., 2006, Biomimetic surface modifications based on the cyanobacterial iron chelator anachelin: Journal of the American Chemical Society, v. 128, no. 4, p. 1064-1065.

Supplementary Material.

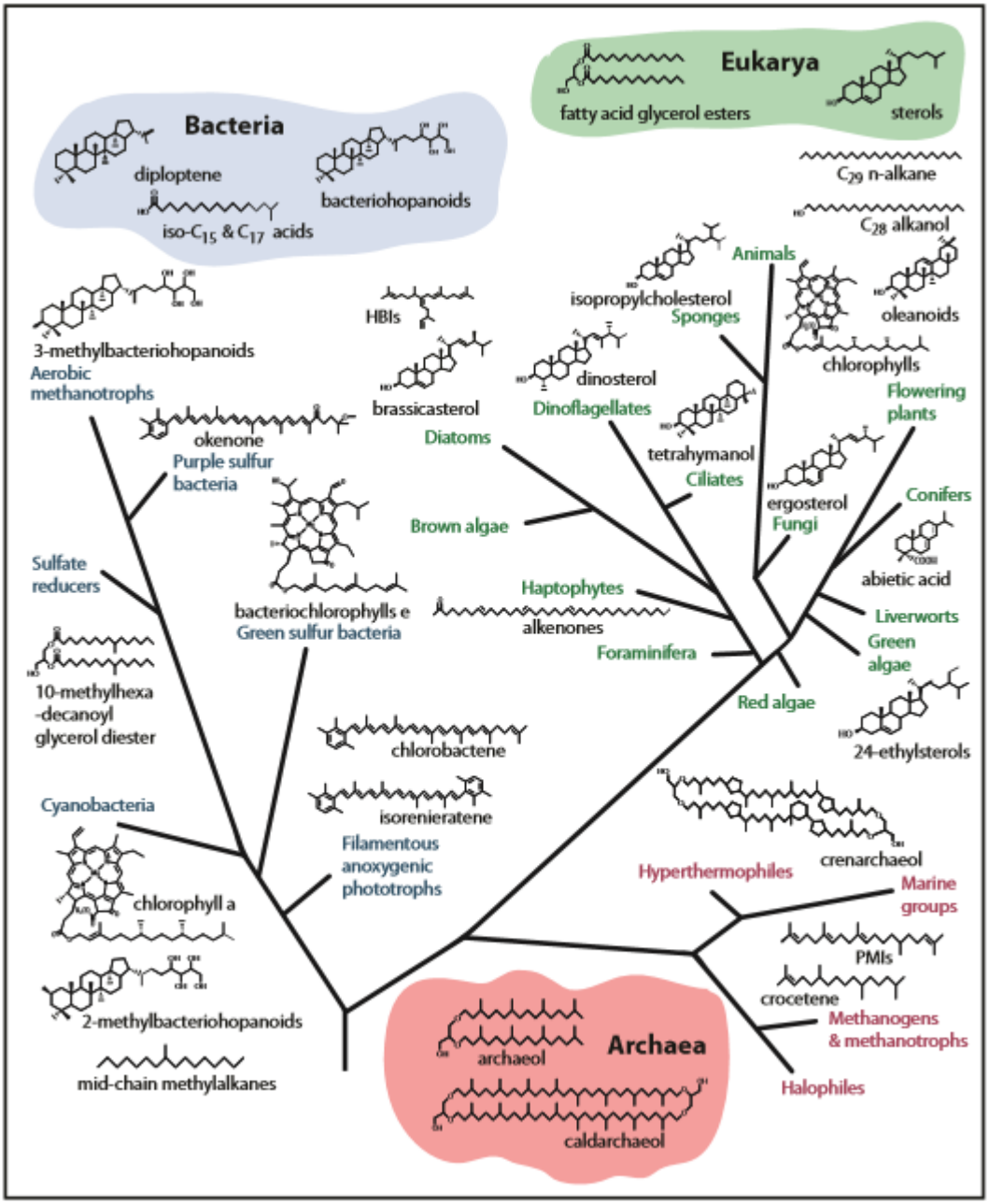

Figure S1. A version of the tree of life, showing life's three domains and the lipids that are characteristic of the major groups of organisms (Briggs and Summons, 2014).

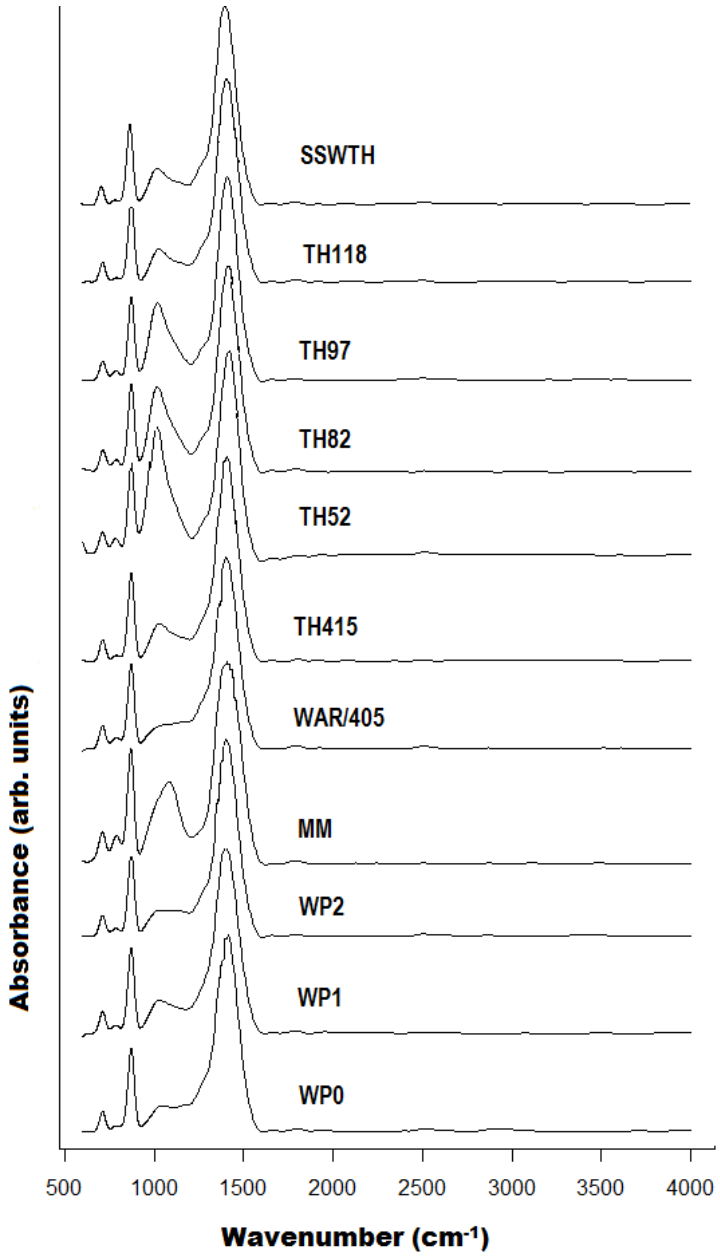

Figure S2. *Absorbance FTIR spectra between 600-4000 cm^{-1} for all samples.*

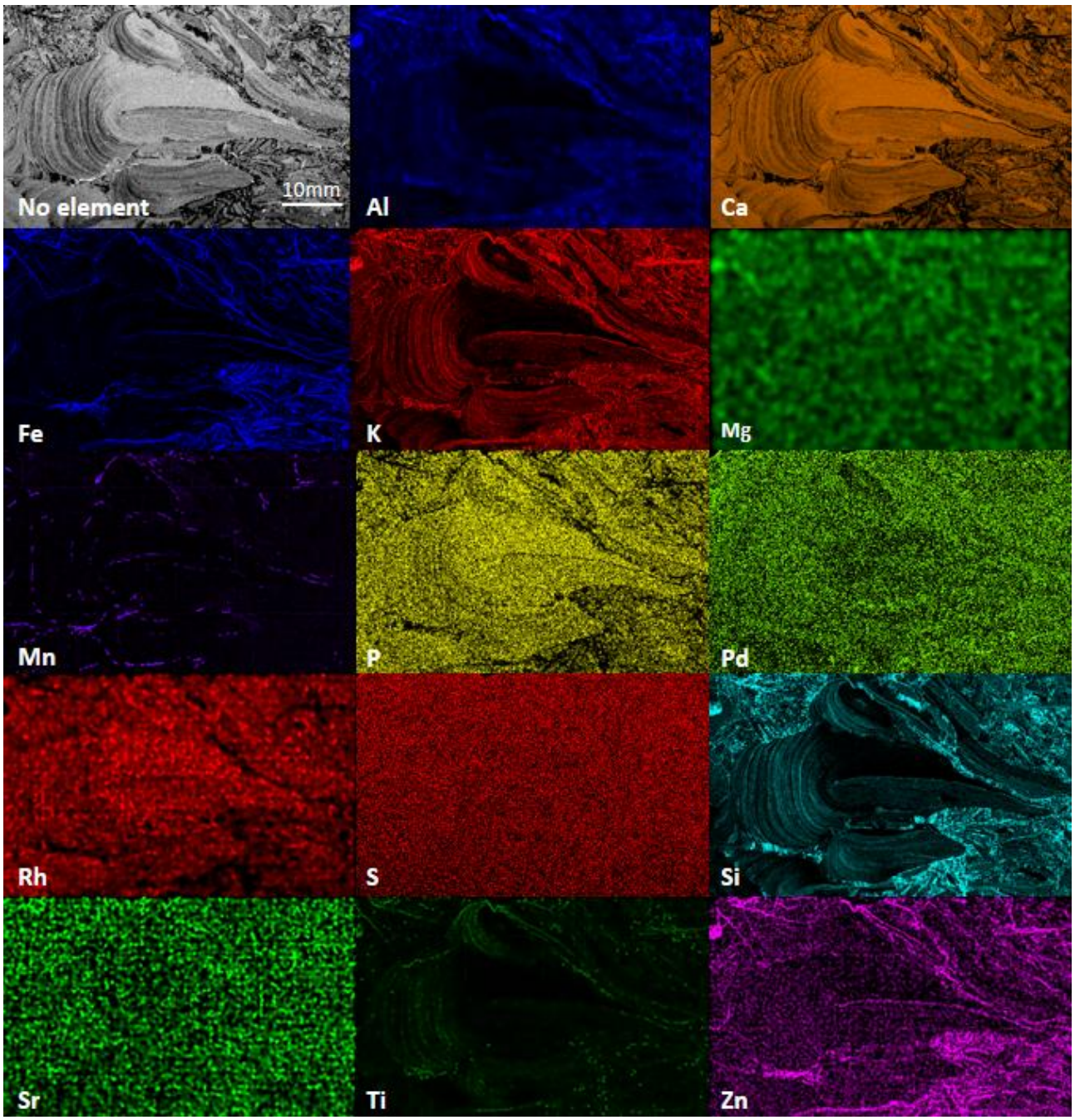

Figure S3. False colour maps of WP1 created by XRF mapping, from left to right, top to bottom; no element, Al, Ca, Fe, K, Mg, Mn, P, Pd, Rh, S, Si, Sr, Ti, and Zn are shown. Scale bar in all images is 10 mm.

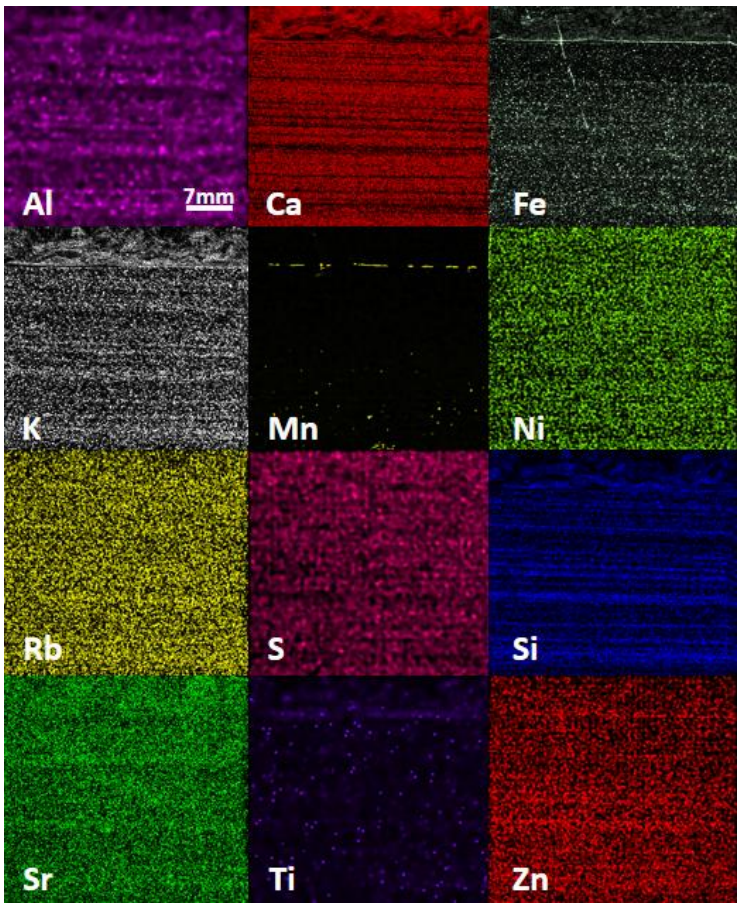

Figure S4. False colour element maps of WP2 and MM created by XRF, from left to right, top to bottom, Al, Ca, Fe, K, Mn, Ni, Rb, S, Si, Sr, Ti, Zn. Scale bar in all images is 7 mm.

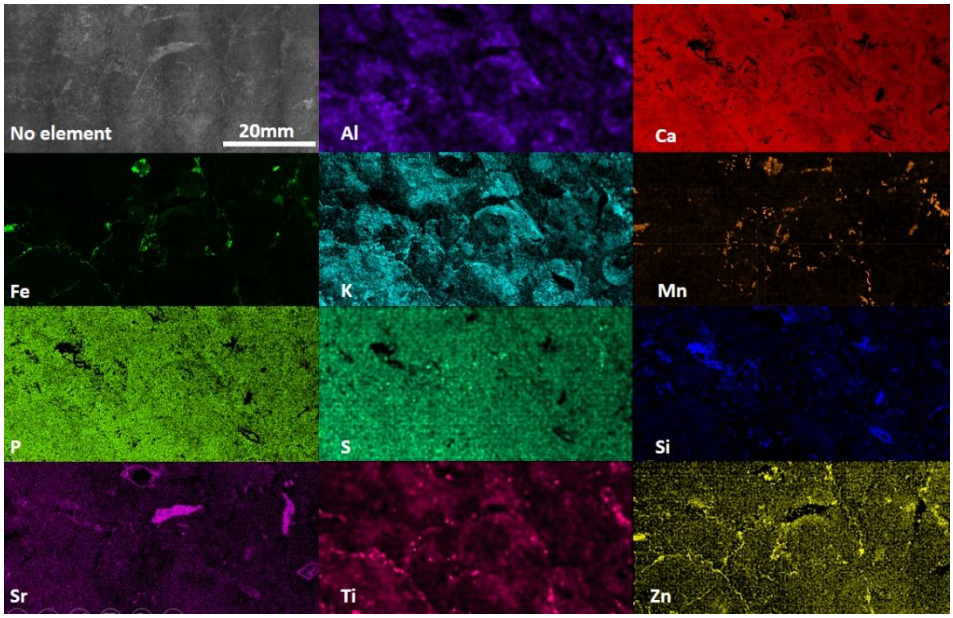

Figure S5. False colour element maps of WAR/405 created by XRF, from left to right, top to bottom, Al, Ca, Fe, K, Mn, P, S, Si, Sr, Ti, Zn. Scale bar in all images is 20mm.

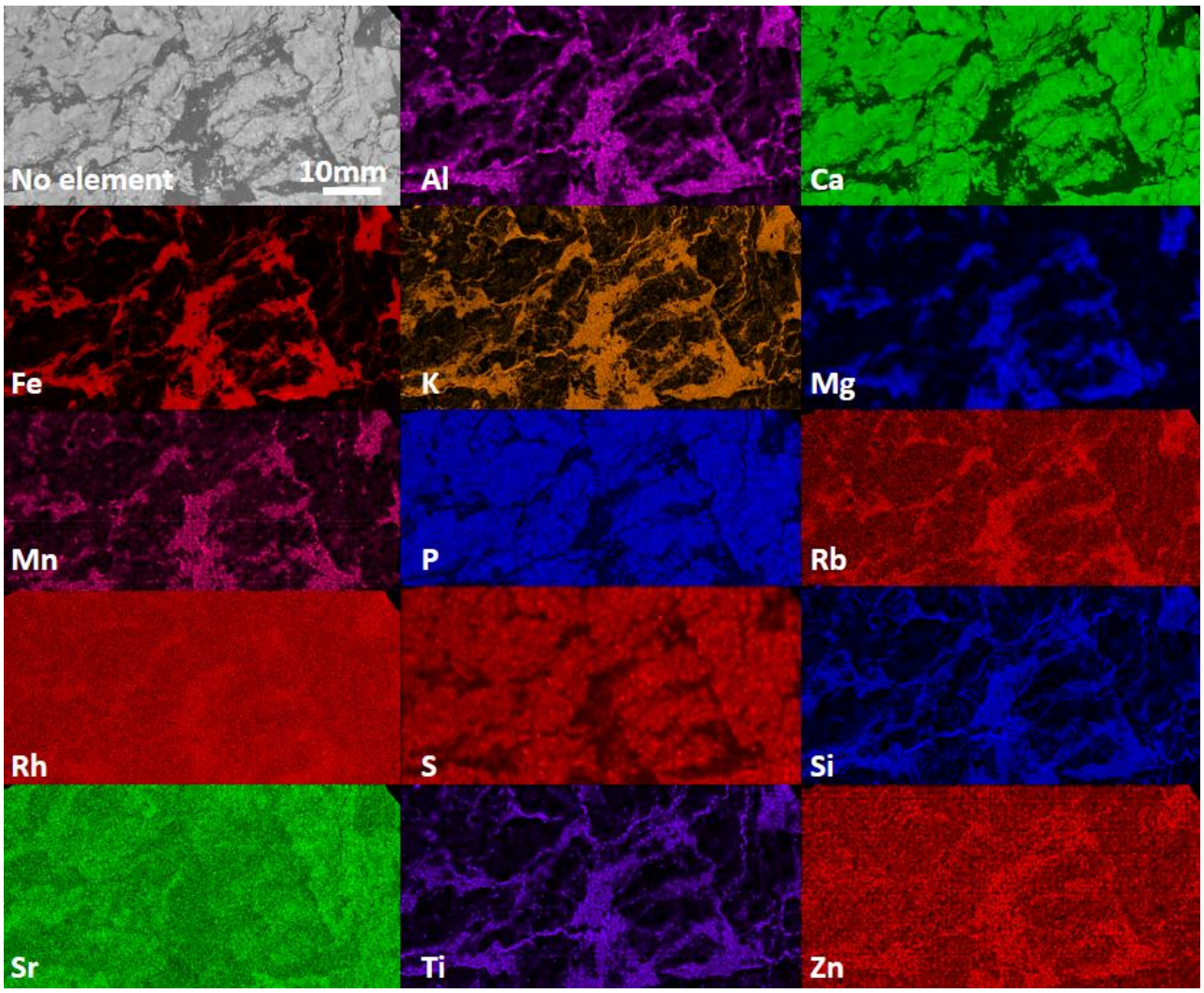

Figure S6. False colour elemental maps of TH118, created by XRF, from left to right, top to bottom; no element, Al, Ca, Fe, K, Mg, Mn, P, Rb, Rh, S, Si, Sr, Ti, Zn. Scale bar in all images is 10mm.

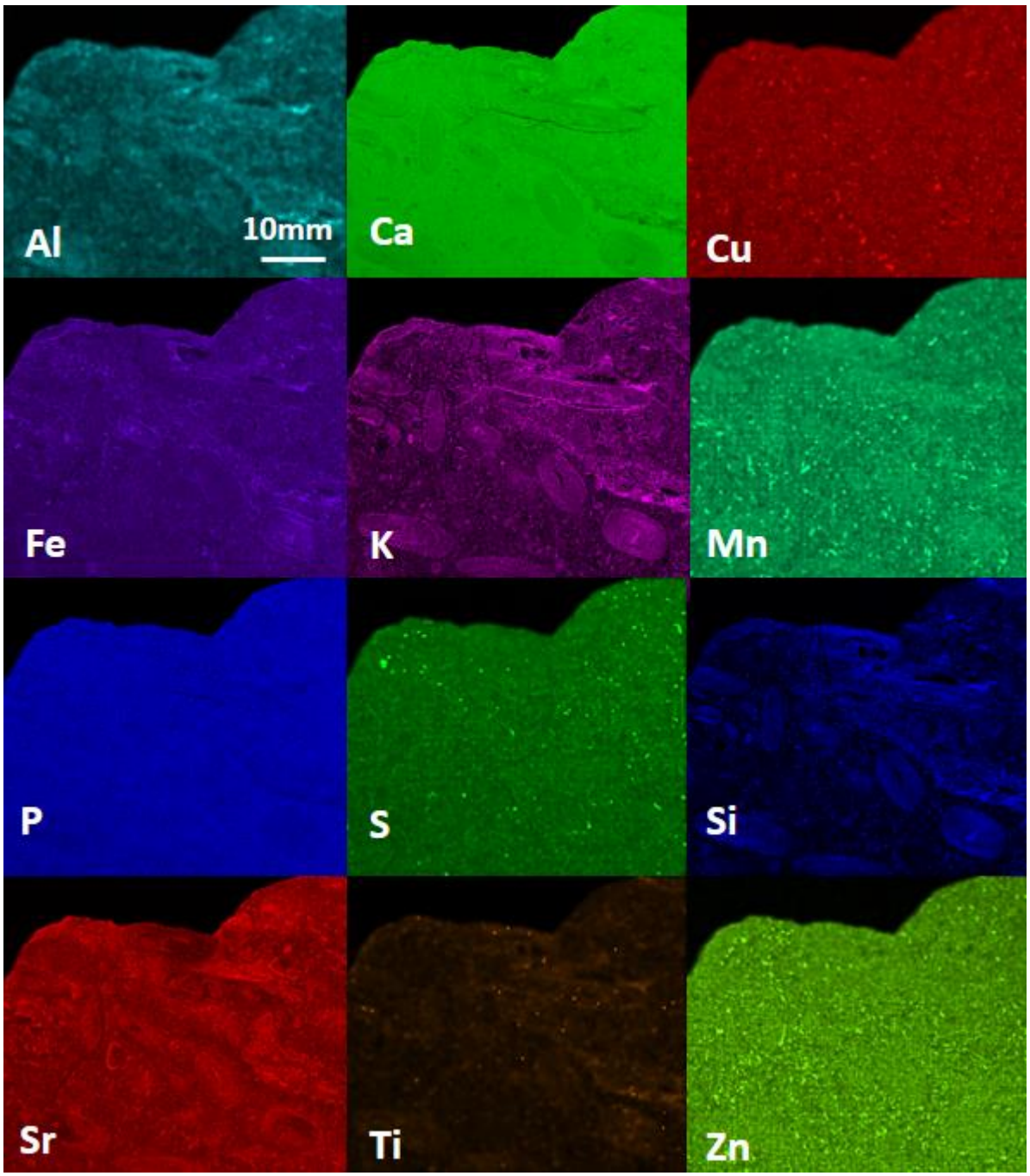

Figure S7. False colour elemental maps of TH118, created by XRF, from left to right, top to bottom; no element, Al, Ca, Cu, Fe, K, Mn, P, S, Si, Sr, Ti, Zn. Scale bar in all images is 10mm.

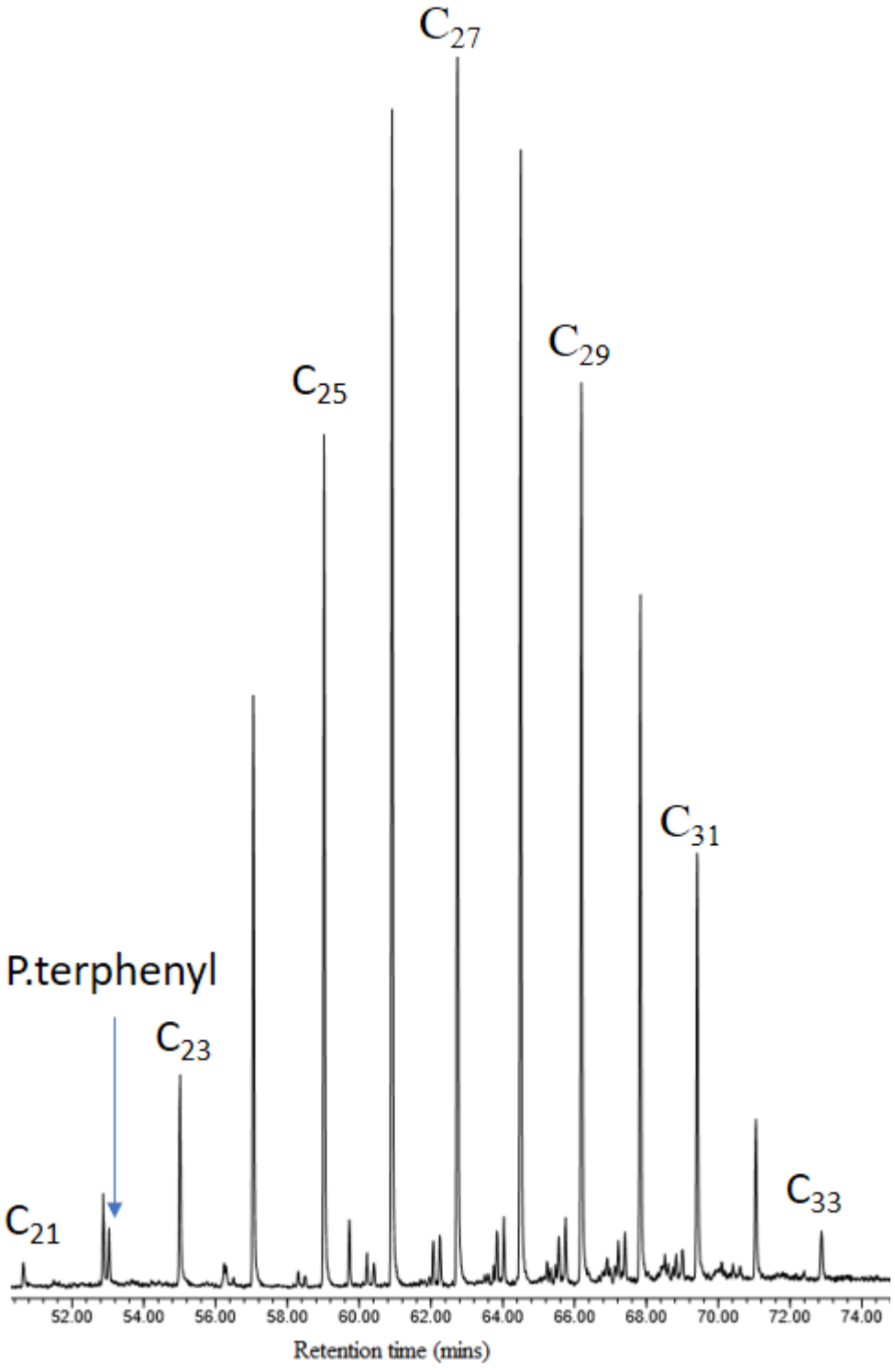

Figure S8. Partial m/z 57 chromatogram of MMBi1 showing n-alkanes, and the standard, P.terphenyl.

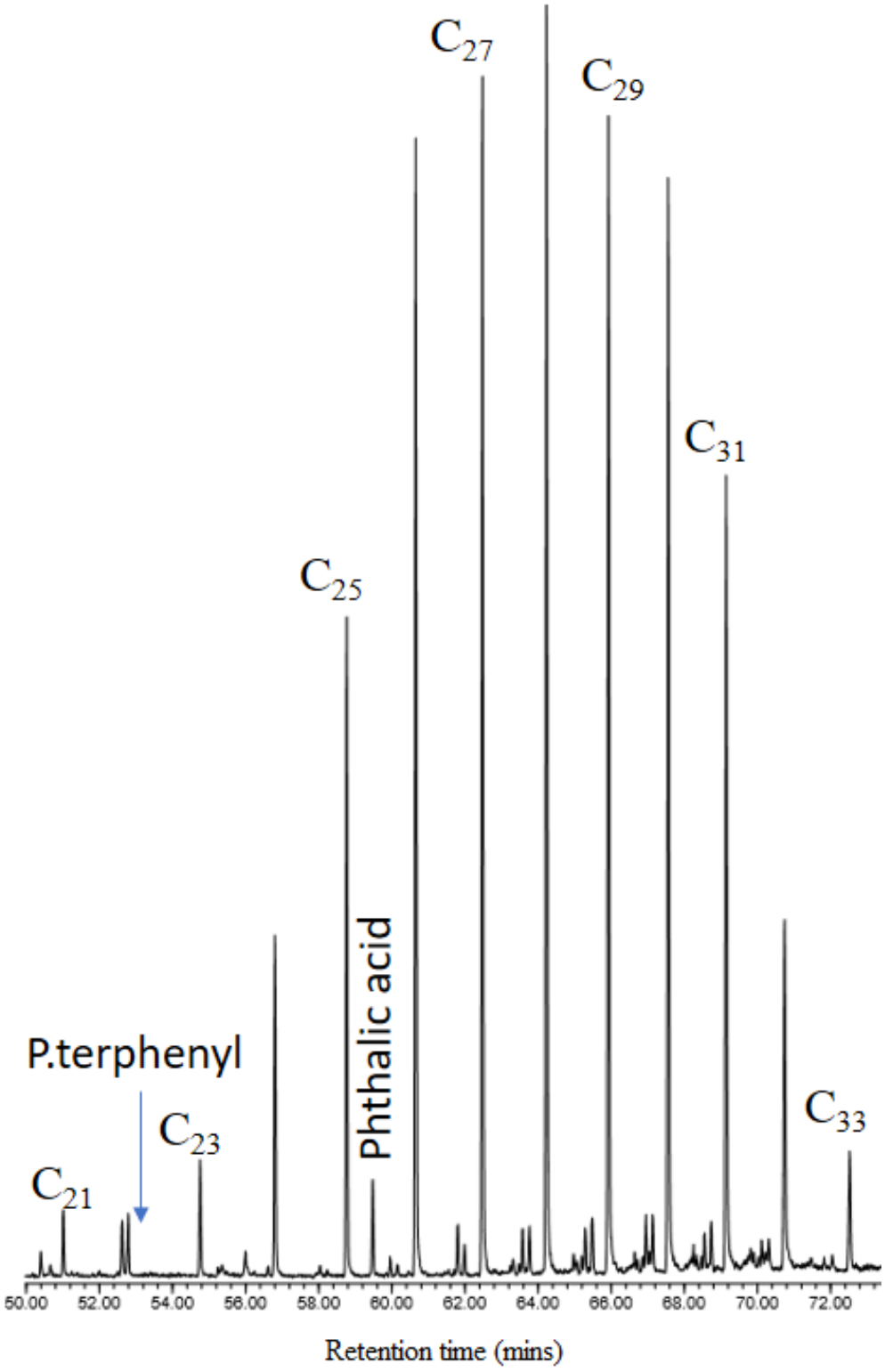

Figure S9. Partial m/z 57 chromatogram of MMBi2 showing n-alkanes, the standard, P.terphenyl, and a phthalic acid contaminant peak.

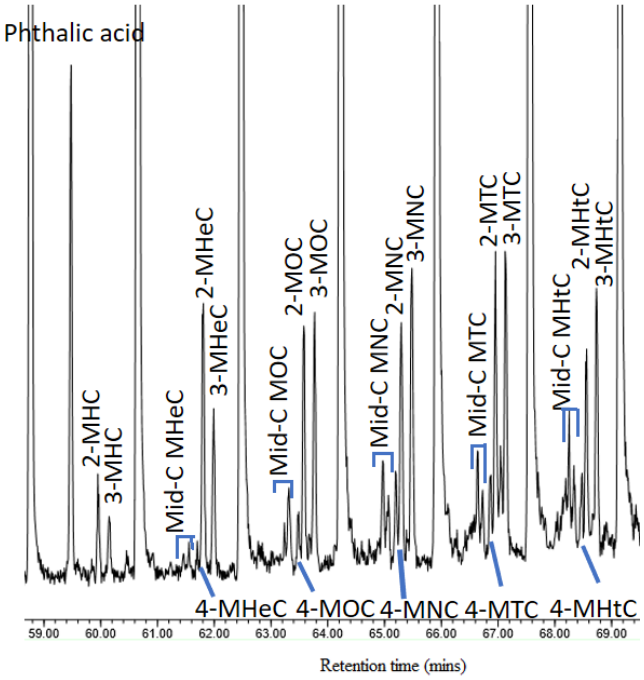

Figure S10. Partial m/z 57 chromatogram of MMBi2 showing the monomethyl alkanes, and a phthalic acid contaminant peak. Mid-C = midchain; MHC =methylhexacosane; MHeC=methylheptacosane; MOC = methyloctacosane; MNC = methylnonacosane; MTC = methyltriacontane; MHtC =methylhentriacontane.

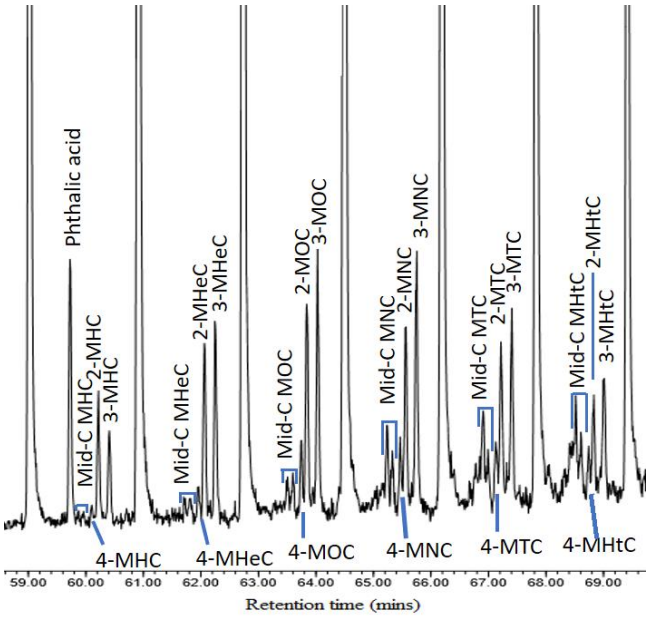

Figure S11. Partial m/z 57 chromatogram of MMBi1 showing the monomethyl alkanes, and a phthalic acid contaminant peak. Mid-C = midchain; MHC =methylhexacosane; MHeC=methylheptacosane; MOC = methyloctacosane; MNC = methylnonacosane; MTC = methyltriacontane; MHtC =methylhentriacontane.

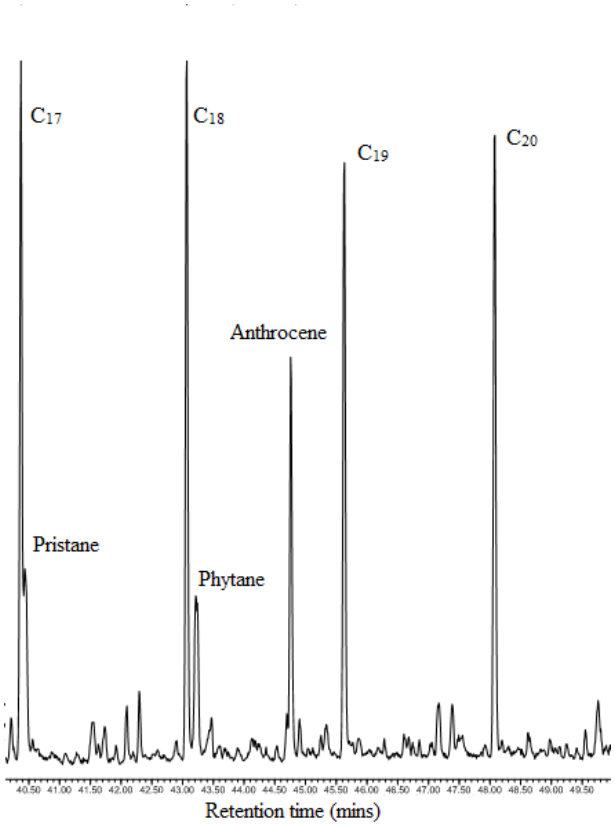

Figure S12. Partial m/z 57 chromatolgram of TH415Bi2. Showing a series of n-alkanes, pristine, phytane, and the standard Anthrocene.

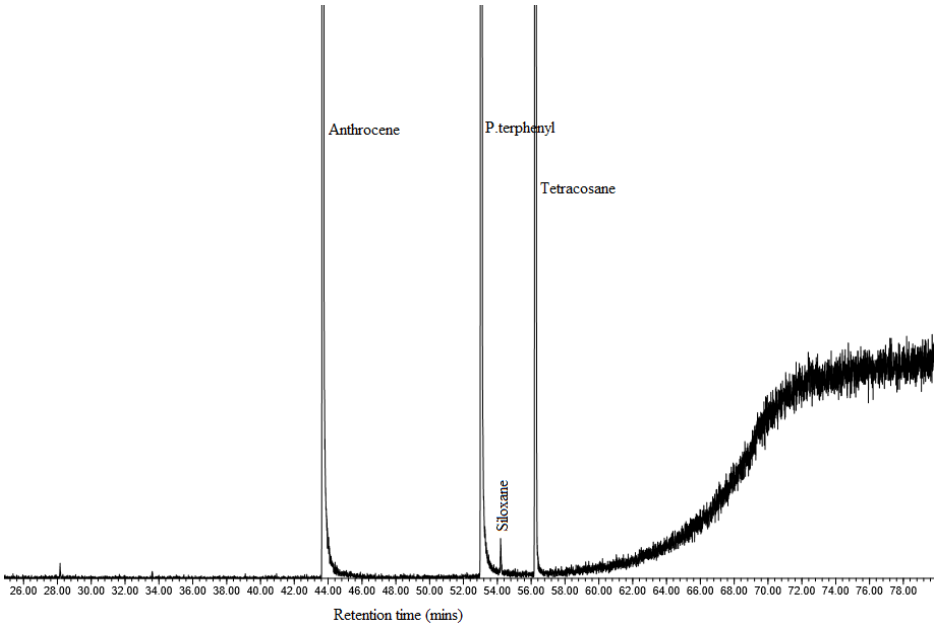

Figure S13. Partial total ion chromatogram of the glassware blank. The standards Anthrocene, P. terphenyl and Tetracosane are shown.

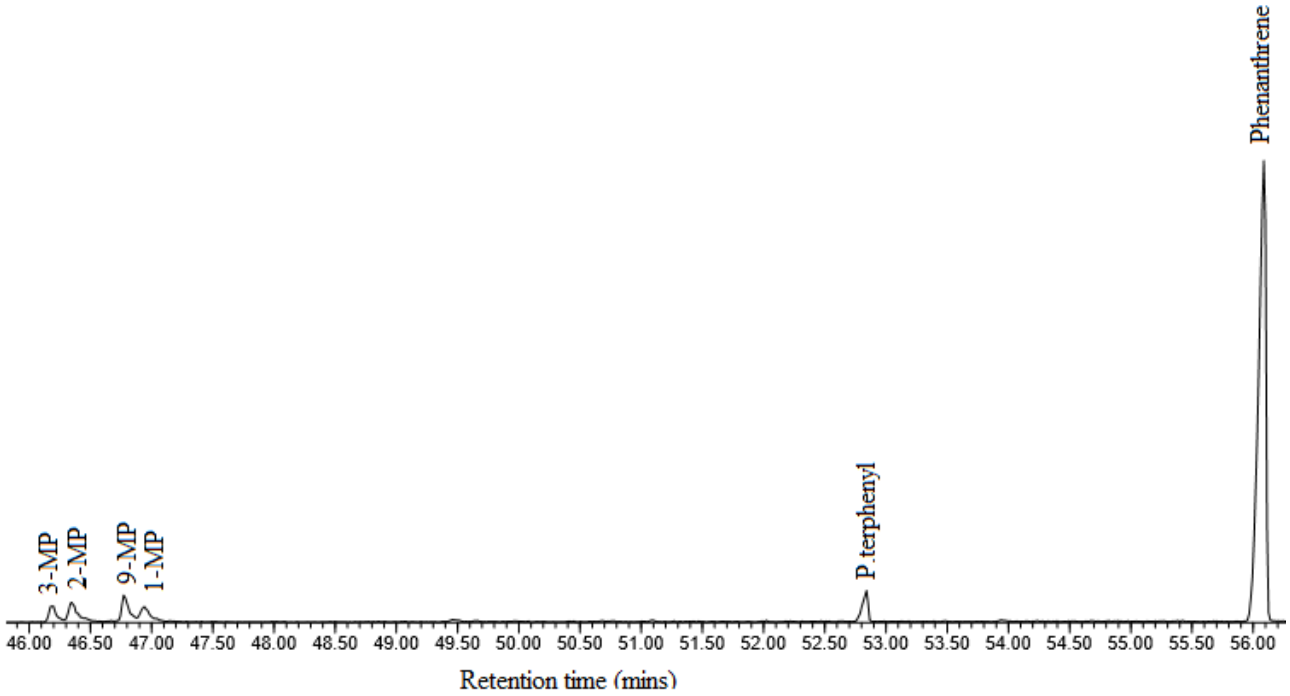

Figure S14. Partial m/z 192 chromatogram of TH415Bi2. MP = methylphenanthrene

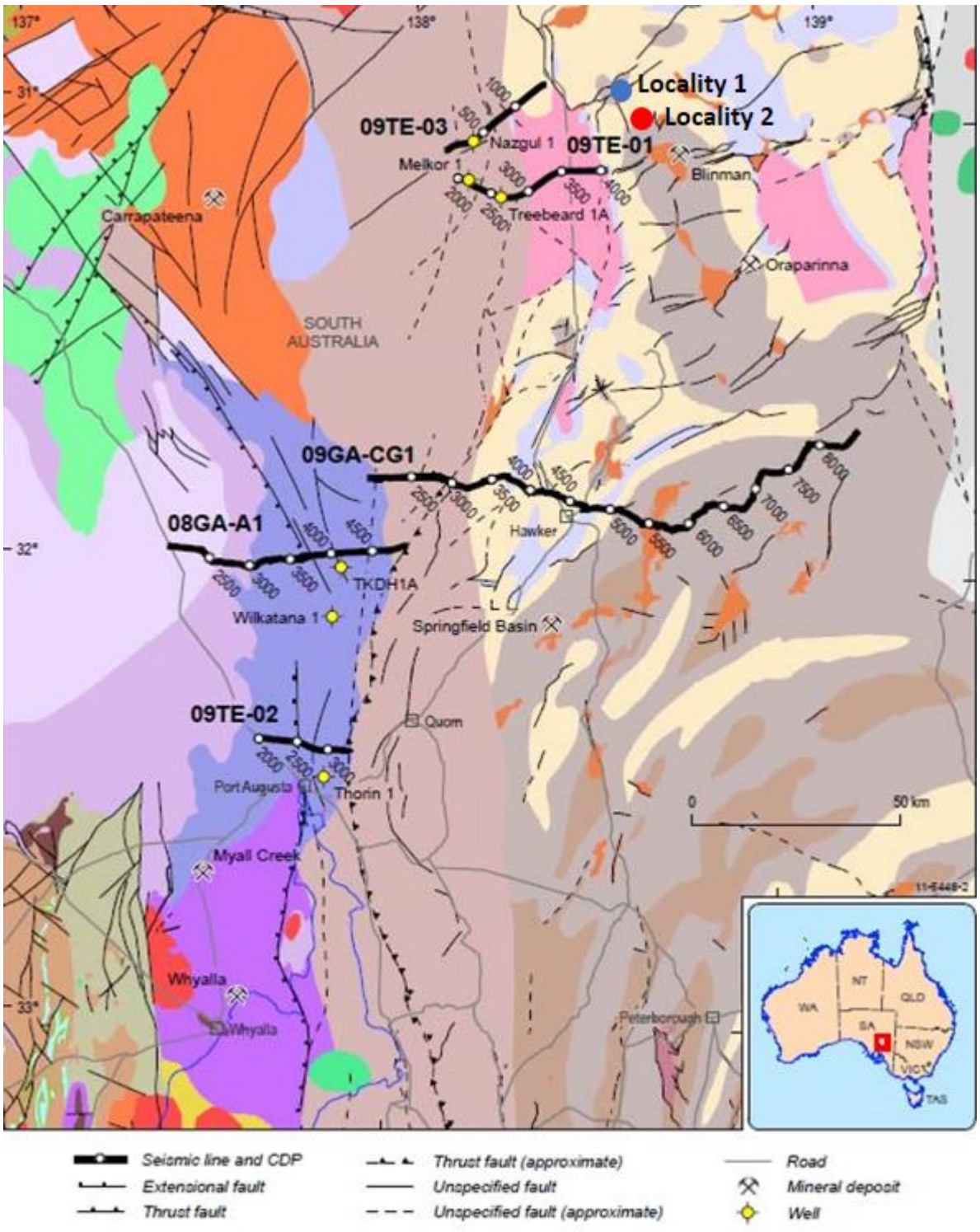

Figure S15. Solid geology map (after Carr et al., 2010) showing the locations of seismic lines 08GA-A1, 09TE-01, 09TE-02 and 09TE-03 in the western Arrowie Basin, South Australia. Localities 1 and 2 from this study are marked on the map.